



A University of Sussex PhD thesis

Available online via Sussex Research Online:

<http://sro.sussex.ac.uk/>

This thesis is protected by copyright which belongs to the author.

This thesis cannot be reproduced or quoted extensively from without first obtaining permission in writing from the Author

The content must not be changed in any way or sold commercially in any format or medium without the formal permission of the Author

When referring to this work, full bibliographic details including the author, title, awarding institution and date of the thesis must be given

Please visit Sussex Research Online for more information and further details

US

UNIVERSITY
OF SUSSEX

DOCTORAL THESIS

**Search for supersymmetry in final
states including two same-sign
hadronically decaying tau leptons**

A tale from triggers to taus

*A thesis submitted in fulfilment of the requirements
for the degree of Doctor of Philosophy*

in the

Experimental Particle Physics Research Group
School of Mathematical and Physical Sciences

Author:

Daniela KOECK

Supervisor:

Prof. Fabrizio SALVATORE

19th December 2022

*To my parents, for their relentless support, love and trust.
To my family away from home, for having my back, always.*

ACKNOWLEDGEMENTS

The past four years have been an incredible adventure with amazing people along the way I'd like to thank at this point. A first big thank you has to go to my supervisor, Fabrizio Salvatore. I could have not wished for a better person to guide me through this adventure. Thank you for your wisdom and support in all aspects of the PhD, not only the scientific parts. Your mentorship, your incredible kindness and humour have been an invaluable support. You have helped me grow as a scientist and person. Thank you also to Antonella de Santo, my second supervisor. Thank you for pointing me to great opportunities and for your support throughout this PhD.

I'd like to thank the entire Sussex PI's and postdocs for creating a welcoming and supportive environment and always being open for discussions. Thanks to the ATLAS PhD office crew for welcoming the newbies with open arms: Fab Trovato, Mario Grandi, Mario Spina, Ioannis, thanks for your open ears, help and after work beers. A special thanks has to go to Marco, who I shared this PhD adventure with. Thank you for pushing me to be confident in my work, always being up for random discussions and being a good friend through the years.

I started my time as PhD student in the Trigger Egamma ATLAS group. I'd like to thank Fernando Monticelli for his kind help during and after my qualification task in answering all the trigger questions I could come up with, for his support and his continued friendship the last years. I'd like to extend my thanks to the SUSY di-tau group with Xuai and Stefan. A special thanks to Stefan for his continued support and great discussions about the analysis work, all things ATLAS, as well as the job hunt. Thanks to Stefan Richter for very useful discussion on the electron ID. Thanks also to Peter Tornambe for his continued friendship and open ear.

Thanks to the BFWG for their financial support and for providing a welcoming, encouraging and motivating network of likeminded women. I'd like to thank Cynthia Burek in particular for her continued mentorship and guidance.

I am very grateful to have crossed paths with Rusteem Ospanov during my time at CERN, thank you for sharing your wisdom, calmness and kindness at long conversations over coffee and lunch. To all my friends and family back home and distributed around the globe - thank you for your patience, support and effort to keep friendships alive.

This thesis would have not been possible without my friends in Brighton, thank you Giada for all the evenings of distraction and laughter! My family away from home: Ash (Aishwarya Padmanabhan), Chinmay, thank you for having my back when things get difficult and providing laughter, joy, good food and great trips when we all needed a break. Ash, thank you for pushing me when I needed a nudge, especially when I didn't want to hear it. Thanks for being incredibly loyal and the truest friend. Thanks to my sister for providing laughter and joy, especially through her little ones. My entire family for being supportive from afar.

Lastly I want to thank my parents: Ohne euch wäre diese Arbeit nicht möglich gewesen. Danke dass ihr immer an mich glaubt, für mich da seid und mich unterstützt, was auch immer ich als nächstes anpacke!

I, Daniela KOECK, hereby declare that this thesis has not been and will not be, submitted in whole or in part to another university for the award of any other degree.

Brighton,
19th December 2022

Daniela KOECK

DOCTORAL THESIS

Search for supersymmetry in final states including two same-sign
hadronically decaying tau leptons

by Daniela KOECK

ABSTRACT

This thesis presents a search for the production of supersymmetric gauge bosons decaying via scalar tau leptons into a final state of at least two same-sign hadronically decaying tau leptons. This search has been performed analysing 13 TeV proton-proton collision data recorded by the ATLAS detector at the CERN Large-Hadron-Collider during the years of 2015-2018. A total of 139 fb^{-1} of data has been analysed. No significant excesses have been observed with respect to the Standard Model expectation, therefore exclusion limits have been set at 95% confidence level. Masses of the lightest chargino ($\tilde{\chi}_1^\pm$), equivalent with the mass of the next-to-lightest neutralino ($\tilde{\chi}_2^0$), up to 960 GeV for massless lightest neutralinos ($\tilde{\chi}_1^0$) have been excluded. Mass differences between the $\tilde{\chi}_1^\pm$ and $\tilde{\chi}_1^0$ as little as 30 GeV have been excluded for a $\tilde{\chi}_1^\pm$ mass of 80 GeV. A statistical combination with an ATLAS analysis using an opposite di-tau final state has been performed, leading to an exclusion of $\tilde{\chi}_1^\pm / \tilde{\chi}_2^0$ masses up to 1160 GeV for massless $\tilde{\chi}_1^0$. Dedicated studies on the performance of electron triggers are also presented within this thesis that have been part of the author's qualification task and continued involvement within the ATLAS trigger community. These studies have hinted towards the need of dedicated electron trigger correction factors in the ATLAS fast simulation framework and the author has provided a first set of such scale factors to the ATLAS Collaboration.

CONTENTS

List of Figures	viii
Introduction	1
1 The Standard Model and Beyond	3
1.1 The Standard Model of Particle Physics	3
1.1.1 Quantum field theory and Gauge symmetries	4
1.1.2 The Higgs mechanism	5
1.1.3 Particle spectrum and interactions of the Standard Model	7
1.2 Shortcomings of the Standard Model	8
1.2.1 Dark Matter	8
1.2.2 Matter-Antimatter asymmetry	9
1.2.3 Hierarchy Problem	10
1.3 Supersymmetry	10
1.3.1 Soft SUSY breaking	11
1.3.2 Particle spectrum of the MSSM	11
1.3.3 Interactions in the MSSM	13
1.4 The bigger picture	14
2 Experimental Setup	17
2.1 LHC	17
2.2 ATLAS	20
2.2.1 ATLAS Coordinate system	21
2.2.2 Inner Detector	22
2.2.3 Calorimeter System	23
2.2.4 Muon System	25
2.2.5 The Trigger System	26
3 Data Acquisition, Reconstruction and Monte Carlo Simulation	29
3.1 Signature triggers	29
3.1.1 Electron triggers	29

3.1.2	Muon triggers	30
3.1.3	Missing transverse momentum triggers	30
3.1.4	Tau Triggers	31
3.2	Object Reconstruction	32
3.2.1	Electrons	32
3.2.2	Muons	34
3.2.3	Jets	34
3.2.4	Taus	34
3.2.5	Missing transverse energy	36
3.3	Monte Carlo Simulation	36
3.3.1	Monte Carlo generators	37
3.3.2	ATLAS detector simulation	38
4	The ATLAS Electron Trigger Performance in Run-2	39
4.1	The ATLAS electron trigger	39
4.2	Electron trigger menu in Run-2	42
4.3	Efficiency measurements and scale factor calculation	45
4.3.1	The Z tag-and-probe method	45
4.3.2	Trigger efficiency evaluation and scale factor calculation	46
4.4	Run 2 performance studies on fully simulated events	47
4.4.1	Single electron trigger	48
4.4.2	Di-electron trigger	49
4.5	Full Run 2 AF2 fast simulation studies	51
4.5.1	Single electron trigger	51
4.6	Summary and future perspectives of this work	56
5	Search for SUSY in a final state with at least two hadronically decaying tau leptons	57
5.1	Introduction and theoretical motivation	57
5.2	Previous model investigations	59
5.3	Analysis strategy	60
5.4	Data and simulation samples	62
5.5	Event selection	63
5.6	Object definitions	64
5.7	Signal region, control region and validation region definitions	66
5.8	Signal region optimisation	66
5.8.1	Choice of kinematic variables	67
5.8.2	SR optimisation procedure	68
5.9	Standard Model background estimations	75
5.9.1	Estimation of Multi-jet background	75
5.9.2	Estimation of W+jets background	81
5.9.3	Top background estimation	85
5.9.4	Multi-boson background estimation	89

5.9.5	Z+jets and Higgs processes	91
5.10	Systematic uncertainties	92
5.10.1	Experimental uncertainties	92
5.10.2	Theoretical and Modelling uncertainties	92
5.11	Statistical concepts	94
5.11.1	Fit strategies	97
5.12	Results	98
5.13	Interpretation	103
5.13.1	Model dependent interpretation	103
5.13.2	Model independent interpretation	105
5.14	The opposite sign analysis	105
5.15	Combined gaugino pair results	106
	Conclusions	108
A	Appendix	110
A.1	Theoretical uncertainty breakdown	110
	Glossary	113
	Bibliography	115

LIST OF FIGURES

1.1	Illustration of the complex scalar potential, adapted from [8] for the case of $\mu^2 < 0$	6
1.2	Overview of most recent ATLAS Higgs results on the production cross sections (a) as well as decay mode branching fraction (b) [5]. The dominant production processes include gluon-gluon Fusion (ggF) and Vector Boson Fusion (VBF), with Higgs production associated with other particles at smaller cross section values.	7
1.3	Exemplary analysis of rotation curves, here showing observations in galaxy NGC 3198. The dotted curve is the galaxy’s gas component, dashed line is its visible components. The dotted-dashed line is visualising a contribution of a Dark Matter halo, with the solid line a fit to the data points including all components. Figure adapted from [12].	9
1.4	Gaugino production mechanisms at hadron colliders, adapted from [6] . Here $\tilde{N}_{1,2,3,4}$ is equivalent to $\tilde{\chi}_{1,2,3,4}^0$ and $\tilde{C}_{1,2}^\pm$ to $\tilde{\chi}_{1,2}^\pm$	14

1.5	Wino and bino field vertices in the MSSM [34].	14
1.6	Latest summary of gluino mass exclusion limits by A Toroidal LHC ApparatuS (ATLAS) for various simplified models . Shown are exclusion limits at 95 % Confidence Level in a lightest neutralino ($\tilde{\chi}_1^0$) versus gluino (\tilde{g}) mass plane. Different simplified models are shown in different coloured lines [36].	15
1.7	Latest summary of gluino mass exclusion limits by Compact Muon Solenoid (CMS) for various simplified models [37]. The excluded mass scale for the gluino is given for light Lightest Supersymmetric Particle (LSP)s on the x-axis, with the associated simplified model and final state highlighted in each bar.	15
1.8	Latest exclusion plots summarising searches for pair production of stop particles by ATLAS [36]. The limits shown are given at 95 % confidence level, with the stop mass on the x-axis and the $\tilde{\chi}_1^0$ mass on the y-axis.	16
1.9	Latest exclusion plots summarising searches for pair production of stop particles by CMS [37]. The x-axis is showing the 95 % confidence level exclusion limit on various squark masses. The bars along the y-axis highlight the simplified models considered to yield the exclusion limits.	16
2.1	Overview of the CERN accelerator facilities, including the acceleration chain leading up to the Large Hadron Collider (LHC) [40].	18
2.2	Summary of the luminosity delivered by the LHC, recorded by the ATLAS detector as well as the overall data good to use for physics analyses [48].	19
2.3	Pileup conditions throughout Run-2 [48].	20
2.4	Overview graphic of the ATLAS detector design , with two people illustrated for scale reference [49].	21
2.5	Slice view of the Inner Detector, highlighting each sub-detectors distance to the beampipe [51] (a) and cut-out view of the barrel and endcap components, not including the Insertable B-Layer (IBL) [44] (b).	22
2.6	Illustration of the ATLAS calorimeter system [44].	24
2.7	Visualisation of an Electromagnetic Calorimeter (ECAL) slice at $\eta = 0$ (a), next to an overview of the material in terms of radiation lengths in front of the presampler and main ECAL (b). Both from [44].	25
2.8	Overview of a quarter of the muon spectrometer, showing all subsystems [61].	26
2.9	Overview of the ATLAS trigger system during Run-2. Adapted from [62].	27
3.1	Efficiency of the lowest unprecaled muon trigger in data collected between 2016 and 2018 in the detector barrel ($ \eta < 1.05$) and end-cap ($1.05 < \eta < 2.5$) regions, from [61]	30
3.2	Illustration of an electron path through the Inner Detector and Calorimeters of ATLAS, highlighting the layer granularity in the electromagnetic calorimeter. The dashed line presents a photon produced through interactions of the electron with the Inner Detector (ID) material. Taken from [67].	33

3.3	Feynman diagram of a leptonic tau decay, highlighting its decay via a W-boson (a). Examples of hadronic tau decays into (from left to right) one charged pion, one charged and one neutral pion as well as three charged pion (b) [74], highlighting in which detector systems the participating particles will be detected.	35
3.4	Performance of the tau Recursive Neural Network (RNN) identification working points in comparison with previously used Boosted Decision Tree (BDT) based identification [76]	36
3.5	CPU time distributions for 250 $t\bar{t}$ events compared for G4, fast G4 and AFII setup, taken from [87]	38
4.1	Visualisation of the Level-1 electron selection [91].	40
4.2	Visualisation of the consecutive algorithms of the electron trigger signature at the High Level Trigger (HLT) for non-isolated electron trigger. Adapted from [88]. . . .	41
4.3	Single electron trigger rates during Run-2 [88]. The three graphs show the the three lower energy triggers with electron likelihood selection making up the single electron trigger as discussed in Table 4.1. Omitted here are the high energy triggers without likelihood selection. In (a) the lowest energy threshold trigger with a 24 GeV and 26 GeV energy threshold in 2015 and 2016-2018, respectively can be seen. In (b) the rate of the 60 GeV threshold trigger without isolation requirement in use from 2016-2018 is shown. Figure (c) shows the trigger rate for the loose likelihood trigger with 120 (140) GeV energy threshold in 2015 (2016-2018).	43
4.4	Level-1 rate for isolated (L1_2EM15VHI) and non-isolated triggers (L1_2EM15VH, L1_2EM20VH) [88].	44
4.5	Illustration of the Z tag-and-probe method.	46
4.6	Single electron trigger performance in Run-2. Shown is the trigger efficiency with respect to the offline electron's transverse energy (a), pseudorapidity (b) and the pileup in the event. Bins with low statistics have been removed.	48
4.7	Single electron trigger efficiency in 2018 in dependency of the offline electron E_T and η	49
4.8	Single electron trigger combination scale factor in dependency of E_T and η of the offline electron.	50
4.9	Di-electron trigger efficiency in Run-2. Shown is the trigger efficiency with respect to the offline electron's transverse energy (a), pseudorapidity (b) and the pileup in the event. Bins with low statistics have been removed [88].	50
4.10	2015 single electron trigger efficiency comparison of full simulation and fast simulation samples. Shown is the trigger efficiency with respect to the offline electron's transverse energy (a), pseudorapidity (b) and the pileup in the event.	52
4.11	2016 single electron trigger efficiency comparison of full simulation and fast simulation samples. Shown is the trigger efficiency with respect to the offline electron's transverse energy (a), pseudorapidity (b) and the pileup in the event.	53

4.12	2017 single electron trigger efficiency comparison of full simulation and fast simulation samples. Shown is the trigger efficiency with respect to the offline electron's transverse energy (a), pseudorapidity (b) and the pileup in the event.	54
4.13	2018 single electron trigger efficiency comparison for full and fast simulation. samples. Shown is the trigger efficiency with respect to the offline electron's transverse energy (a), pseudorapidity (b) and the pileup in the event.	55
4.14	Scale Factor maps in dependency of η and E_T for fast simulation (a) as well as full simulation (b).	55
5.1	Cross section comparison in 13 TeV proton-proton collisions [97, 98].	58
5.2	Feynman diagram of the simplified supersymmetric model considered in this thesis [95].	58
5.3	Results of previous model investigations in partial Run-2 data [99] . In its $m_{\tilde{\chi}_1^0}$ vs $m_{\tilde{\chi}_2^0}$ interpretation, as well as for a benchmark point in dependency of the stau mass splitting parameter x	60
5.4	Overview of Standard Model (SM) processes contributing to a di-tau final state. . .	61
5.5	Visualisation of the available signal mass points.	63
5.6	Visualisation of signal, control and validation regions and a typical arrangement in phase space.	67
5.7	Kinematic variable distributions for SS scenario after a loose preselection. Error bands include statistical uncertainties only. The lower panel shows the significance Z_n including a 30 % systematic uncertainty assumption.	69
5.8	Significance estimation including a 30% flat systematic uncertainty.	70
5.9	"N-1" distributions of relevant kinematic variables after SR-C1N2SS-LM requirements, except the one on the shown variable, have been applied. The stacked histograms show the expected SM backgrounds estimated from Monte Carlo (MC), normalised to 139 fb^{-1} as well as Multi-jet expectation as described in section 5.9.1. Statistical uncertainties and systematic uncertainties as discussed in section 5.10 are included in the error band.	71
5.10	"N-1" distributions of relevant kinematic variables after SR-C1N2SS-HM requirements, except the one on the shown variable, have been applied. The stacked histograms show the expected SM backgrounds estimated from MC, normalised to 139 fb^{-1} as well as Multi-jet expectation as described in section 5.9.1. Statistical and systematic uncertainties as discussed in 5.10 are included in the error band.	72
5.11	Remaining kinematic distributions in SR-C1N2SS-LM, for all variables not used in the signal region definition. The error band includes statistical and systematic uncertainties. The lower panel shows the significance Z_n including a 30 % systematic uncertainty assumption.	73
5.12	Remaining kinematic distributions in SR-C1N2SS-HM, for all variables not used in the signal region definition. The error band includes statistical and systematic uncertainties. The lower panel shows the significance Z_n including a 30 % systematic uncertainty assumption.	74

5.13	Significance distribution for the (a) SR-C1N2SS-LM, (b) SR-C1N2SS-HM for 139 fb^{-1} . The statistical uncertainty and 30% systematic uncertainty on SM backgrounds are included in the Z_N calculation.	75
5.14	ABCD region illustration for the low and high mass signal regions Here only the cuts on $m_T(\tau_1)+m_T(\tau_2)$ and the tau-ID are shown. * As described in section 5.8.2, further requirements on other kinematic variables are applied to define the signal regions .	76
5.15	Dependency of the transfer factor on $m_T(\tau_1) + m_T(\tau_2)$ for low mass and high mass regions. Highlighted in the lower panel in red is the nominal used transfer factor value. All uncertainties are statistical only.	77
5.16	Data/MC distributions in VR-F-LM, the uncertainty band includes statistical and systematic uncertainties. No normalisation factors as extracted in the background-only fit described in section 5.12 are applied.	78
5.17	Data/MC distributions in VR-F-HM, the uncertainty band includes statistical and systematic uncertainties. No normalisation factors as extracted in the background-only fit described in section 5.12 are applied.	79
5.18	Background composition in W+jet Control and Validation region	82
5.19	Signal contamination in percentage in W-CR and W-VR.	82
5.20	Distributions of relevant kinematic variables in the W-CR. The SM backgrounds other than multi-jet production are estimated from MC simulation and normalised to 139 fb^{-1} . The hatched bands represent the statistical uncertainties and systematic uncertainties discussed in 5.10. The lower panel shows the ratio of data to the SM background estimate. No normalisation factors as extracted in the background-only fit described in section 5.12 are applied.	83
5.21	Distributions of relevant kinematic variables in the W-VR. The SM backgrounds other than multi-jet production are estimated from MC simulation and normalised to 139 fb^{-1} . The hatched bands represent the statistical uncertainties and systematic uncertainties discussed in 5.10. The lower panel shows the ratio of data to the SM background estimate. No normalisation factors as extracted in the background-only fit described in section 5.12 are applied.	84
5.22	Process composition in Top Control and Validations	85
5.23	Signal contamination of high mass Top CR and VR in percent	86
5.24	Top High mass control region data/MC distributions. The hatched band is including the statistical and systematic uncertainties. No normalisation factors as extracted in the background-only fit described in section 5.12 are applied.	87
5.25	Top High mass validation region data/MC distributions. The hatched band is including the statistical and systematic uncertainty. No normalisation factors as extracted in the background-only fit described in section 5.12 are applied.	88
5.26	Breakdown of the top compositions in the top control and validation region	89
5.27	Multiboson purity in MBVR-SS as well as signal contamination in %	90

5.28 Kinematic distributions comparing data/MC in the Multiboson validation region. The hatched uncertainty band includes statistical and systematic uncertainties. No normalisation factors as extracted in the background-only fit described in section 5.12 are applied.	91
5.29 pre-fit Multijet CR-A (as defined in the ABCD method in section 5.9.1) and post-fit MJ-VR.	99
5.30 pre-fit WCR and post-fit WVR.	99
5.31 pre-fit Top control region and post fit top validation region - showing improvement in the top modelling through the fit [95].	100
5.32 Reduced correlation Matrix for the C1N2SS background only fit.	100
5.33 Unblinded signal region distributions for SR-C1N2SS-LM. All normalisation factors extracted in the background-only fit are applied. The hashed band includes statistical and systematic errors.	101
5.34 Unblinded signal region kinematic distributions for SR-C1N2SS-HM. All normalisation factors extracted in the background-only fit are applied. The hashed band includes statistical and systematic errors.	102
5.35 Pull Plot: Summary of all validation and signal regions included in the background only fit and the significance of the difference of background estimation compared to observed data.	103
5.36 Exclusion limits in the SR-C1N2SS-LM (a), SR-C1N2SS-HM (b) as well as both signal regions statistically combined (c)	104
5.37 Simplified models considered in the opposite-sign analysis.	106
5.38 Summary of all validation and signal regions considered in the opposite-sign and same-sign analyses after the analysis-specific background-only fits [137].	107
5.39 Combined exclusion contours of the opposite-sign and same-sign analysis [137]. In (a) the exclusion limits at 95 % CL are given in the $\tilde{\chi}_1^\pm / \tilde{\chi}_2^0$ versus $\tilde{\chi}_1^0$ mass plane. In (b) the same exclusion limits are shown with respect to the mass splitting $\Delta m(\tilde{\chi}_1^\pm, \tilde{\chi}_1^0)$ in dependency to the $\tilde{\chi}_1^\pm / \tilde{\chi}_2^0$ mass.	107

INTRODUCTION

Within the last decades of particle physics research there have been many milestones and discoveries, narrowing in on the building blocks of matter and leading to the development of the Standard Model (SM) of particle physics as we know it today. This has been achieved through extraordinary efforts and interplay between experimental measurements unravelling hints and evidence of new particles, and theoretical effort of tying this to an overarching theory and achieving more precise predictions: from the discovery of the electron in 1897 [1], to the discovery of the tau lepton in 1975 [2], to the most recent success of the theoretical predictions lying in the experimental discovery of the Higgs boson [3, 4]. In the last ten years since the Higgs boson's discovery, its properties have been measured to high precision [5] and the Standard Model's predictions have been put to stringent tests. In various measurements, tensions with predictions of the Standard Model have been appearing, hinting towards a larger underlying theory. The limitations of the Standard Model have become more and more evident. The Hierarchy problem [6], questioning the difference in scales between the Higgs mass and the Planck scale, raising the need for unnatural fine-tuning, is only one of the hints for the need for a larger principle. The evolution of our universe into a matter-dominated universe is so far unexplained, with no mechanisms within the Standard Model to sufficiently generate this asymmetry with anti-matter [7–9]. Lastly, one of the most striking hints connects the limitations of the theoretical model describing the smallest building blocks in our universe to the largest structures known to humankind. The presence of Dark Matter [10–15] in galaxies and galaxy clusters can not be explained through a composition of Standard Model particles.

An additional symmetry between bosons and fermions called Supersymmetry (SUSY) could offer solutions to many of these limitations. Not only could SUSY avoid the need for fine-tuning of the Higgs mass, but also Weakly Interacting Massive Particles (WIMPs) predicted by SUSY could make up a component of Dark Matter. This striking connection of two problems at length scales varying from the size of a fundamental particle to galaxies and galaxy clusters is known as the WIMP miracle.

Supersymmetric particles have been searched for in many ways at the Large-Electron-Positron collider, the Large-Hadron-Collider as well as through a variety of non-collider experiments. Up to the moment of writing this thesis, there has been no direct detection of Dark Matter particles and no evidence of supersymmetric particles at colliders.

According to definitions of science historian Thomas Kuhn and discussion thereof of Gian Francesco Giudice ([16, 17]) particle physics can currently be described to be in a period of "krisis". Krisis has to be understood in its original meaning - a period of change and anticipation. This period can be frustrating and confusing, with a lack of direction to a new underlying principle, but should be seen as a privilege. A period preceding a paradigm change, with room for creativity for new ideas but also the need for diligent exploration of limitations in current experiments.

At the time of writing, a new data-taking period at the LHC has just begun. In preparation for this new data taking, it is crucial to thoroughly analyse the Run-2 data set, find its limitations and uncovered areas of new physics searches in order to prepare for the new challenges to come.

In this thesis, a search for **SUSY** has been performed, looking for a production of the lightest chargino and next to lightest neutralino (supersymmetric partners of SM gauge bosons), decaying via a scalar tau lepton into a final state with hadronically decaying tau leptons. This search has been performed with data collected by the ATLAS detector at the LHC, as part of the ATLAS Collaboration. This final state with hadronically decaying tau leptons belongs to the 'paths less walked' within the ATLAS Collaboration, due to its challenging reconstruction. This offers an interesting window to determine and overcome the limitations of the ATLAS Collaboration's search program for **SUSY**. This analysis has been the author's full responsibility. Next to this main effort within this thesis, the performance of electron triggers within ATLAS have been studied as part of the author's qualification task as well as continued commitment to ensure the successful operation and good performance of ongoing ATLAS data-taking.

The structure of this thesis is as follows: A brief overview of the theoretical concepts of the SM as well as its limitations, motivating **SUSY** is given in Chapter 1. This is followed by a conceptual description of LHC proton-proton collisions and the ATLAS detector in chapter 2. Further details on the data collection and reconstruction of collision events as well as the simulations used to study the events is given in Chapter 3. A detailed view on the electron trigger and its performance is given in Chapter 4. The search for supersymmetric gauge bosons in all its necessary details is given in Chapter 5.

THE STANDARD MODEL AND BEYOND

1

"Nothing in life is to be feared. It is only to be understood. Now is the time to understand more, so that we may fear less"

Marie Curie

This thesis covers a search for new particles predicted by **SUSY** an extension to the **SM** of particle physics. In the following chapter, the foundations for this search will be laid. A summary of the core concepts of the **SM** will be given in section 1.1, discussing how quantum field theory in combination with gauge symmetries can explain and predict a large set of phenomena in our universe. This is followed by a short discussion on the limitations of this current best theoretical description of fundamental particles and their interactions in section 1.2. Supersymmetry is an extension to the **SM** that can resolve some of these shortcomings, motivating an extensive search program within experimental particle physics. An overview of **SUSY**, focusing on the phenomenological consequences allowing for a search at hadron colliders, is given in section 1.3. The search presented in this thesis is brought into context in the broader field in a discussion of the bigger picture in section 1.4.

1.1 The Standard Model of Particle Physics

The Standard Model of Particle Physics is an extremely successful theory, able to predict particle interactions to high precision. This year (2022) marks the 10th anniversary of one of the biggest successes in particle physics to date - the discovery of the Higgs boson [3, 4]. With the **SM** as it is today, including the Brout-Englert-Higgs mechanism, we can put its predictions to stringent tests through precision measurements of its couplings, masses and interactions. Searches for new physics like those described in this thesis are a crucial way to put the **SM** to a test and increasingly go hand-in-hand with precision measurements.

1.1.1 Quantum field theory and Gauge symmetries

The SM is a theory of quantum fields. Similar to classical field theory, a Lagrangian formalism is used to describe the components of the theory. The basis of the Lagrangian formalism is presented through its connection with the action $S = \int d^4x \mathcal{L}$, expressed through a Lagrangian density \mathcal{L} [18]. Connecting this with the principle of least action ($\delta S = 0$), postulating that every physical process is minimising its action, leads to the Euler-Lagrange equation in (1.1). This is describing the equation of motion for a field ψ with space-time indices μ :

$$\partial_\mu \left(\frac{\partial \mathcal{L}}{\partial (\partial_\mu \psi)} \right) - \frac{\partial \mathcal{L}}{\partial \psi} = 0 \quad (1.1)$$

Noether theorem [19] connects symmetries of a Lagrangian with conserved charges. In the SM, these symmetries are in the form of local phase transformations $\psi(x) \rightarrow e^{i\alpha(x)}\psi(x)$ or *gauge* transformations. The transformations are connected with rotational symmetries of Lie groups and can be summarized through the group structure [8]:

$$U(1)_Y \otimes SU(2)_L \otimes SU(3)_C \quad (1.2)$$

Every local gauge transformation can be absorbed within a gauge field, with the excitations of the gauge fields called *gauge bosons*. The conserved charges connected with the transformations of each group are indicated through the group subscripts. The $SU(3)_C$ part of the overall Standard Model symmetry group is the symmetry group of quantum chromodynamics, C representing the strong interactions with conserved colour charge. The gauge symmetry generates eight gauge bosons, representing the eight possible gluons. The hypercharge Y presents the conserved charge under $U(1)$ transformations of the Lagrangian and can be expressed through the Gell-Mann-Nishijima formula (here in one of its forms, based on discussions in [20–22]):

$$Y = 2(Q_{em} - I_3) \quad (1.3)$$

This connects the electromagnetic and weak interaction, including the electromagnetic charge Q as well as the third component of the Isospin, I_3 and allows for the direct product of the $U(1)_Y \otimes SU(2)_L$ symmetry groups. The gauge boson of the $U(1)_Y$ group is a neutral gauge boson, B_μ , whereas the $SU(2)_L$ symmetries are absorbed in a set of three gauge fields, $W_\mu^{(1)}, W_\mu^{(2)}, W_\mu^{(3)}$. These four massless gauge fields form eigenstates of the electroweak interaction [8], connected through the weak mixing angle θ_W :

$$\begin{aligned} A_\mu &= B_\mu \cos \theta_w + W_\mu^{(3)} \sin \theta_w \\ Z_\mu &= -B_\mu \sin \theta_w + W_\mu^{(3)} \cos \theta_w \\ W^\pm &= \frac{1}{\sqrt{2}} (W_\mu^{(1)} \mp i W_\mu^{(2)}) \end{aligned} \quad (1.4)$$

The discovery of the Z-boson and its interactions in comparison with, and together with, the photon offer experimental proof of the above-described field configurations. If the Z boson would be a gauge boson of the weak interaction in itself, a W^0 , it would only couple to left-handed particles. This would lead to an asymmetry in polarised electron-positron collisions, the so-called left-right asymmetry. This has not been observed, confirming the right-handed coupling component in these interactions in measurements performed at the Stanford Linear Accelerator Center [23].

1.1.2 The Higgs mechanism

The gauge groups discussed above describe particle interactions under electroweak and strong interactions through gauge invariant principles. Particle mass terms in the Lagrangian, accounting for heavy bosons and massive particles observed in experiments, would break these gauge invariances. Therefore an additional mechanism needs to be responsible for the generation of observed particle masses. Similar to the Meißner-Ochsenfeld effect [24,25] in superconductivity, where a background field of scalar Cooper pairs [26] can lead to a photon appearing massive, a background field could be the origin of particle masses. Such a background field in combination with spontaneous symmetry breaking, in which the ground state of a system does not include the symmetry of the system, is the foundation of the mechanism developed by Brout, Englert, Kibble and Higgs [27–29]. A short overview of this mechanism is first given in a simplified case, followed by a short discussion of the mechanism within the SM. The discussion closely follows [8].

To introduce a background field into the SM, a Lagrangian term describing both its potential as well as a kinematic term has to be introduced. In the case of a complex scalar field as in equation (1.5), its Lagrangian is described by equation (1.6).

$$\phi = \frac{1}{\sqrt{2}}(\phi_1 + i\phi_2) \quad (1.5)$$

$$\mathcal{L} = (\partial_\mu \phi)^* (\partial^\mu \phi) - \mu^2 (\phi^* \phi) - \lambda (\phi^* \phi)^2 \quad (1.6)$$

The last two terms in the Lagrangian (1.6) define the potential of the complex scalar field, which can be illustrated in dependency of its two real components, ϕ_1 and ϕ_2 , as shown in Figure 1.1.

This potential is often named as *wine-bottle potential* or *Mexican-hat potential*. The parameter λ needs to be positive for this potential to have a minimum. The Lagrangian described has a global $U(1)$ symmetry and has a multitude of possible minima, which is defined through its *vacuum expectation value* v . This can be visualised through the dashed circle in Figure 1.1.

$$\phi_1^2 + \phi_2^2 = \frac{-\mu^2}{\lambda} = v^2 \quad (1.7)$$

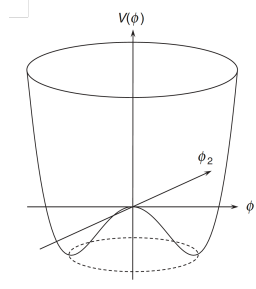


Figure 1.1: Illustration of the complex scalar potential, adapted from [8] for the case of $\mu^2 < 0$

Through the selection of a specific ground state (e.g. $(\phi_1, \phi_2) = (v, 0)$), the global symmetry is spontaneously broken. Any field can be expressed as an expansion around its ground state. When expanding the complex scalar field with respect to two fields η and ξ , with $\phi = \frac{1}{\sqrt{2}}(\eta + v + i\xi)$, the Lagrangian in equation (1.6) can be expressed like:

$$\mathcal{L} = \frac{1}{2}(\partial_\mu \eta)(\partial^\mu \eta) - \frac{1}{2} \underbrace{(2\lambda v^2)}_{m_\eta^2} \eta^2 + \frac{1}{2}(\partial_\mu \xi)(\partial^\mu \xi) - \underbrace{(\lambda v \eta^3 + \frac{1}{4} \lambda \eta^4 + \frac{1}{4} \lambda \xi^4 + \lambda v \eta \xi^2 + \frac{1}{2} \lambda \eta^2 \xi^2)}_{V_{int}(\eta, \xi)} \quad (1.8)$$

This presents a Lagrangian density for a massive field η as well as a massless field ξ , as well as interaction terms. The massless field ξ is a so-called *Goldstone* boson, originating from the spontaneous symmetry breaking.

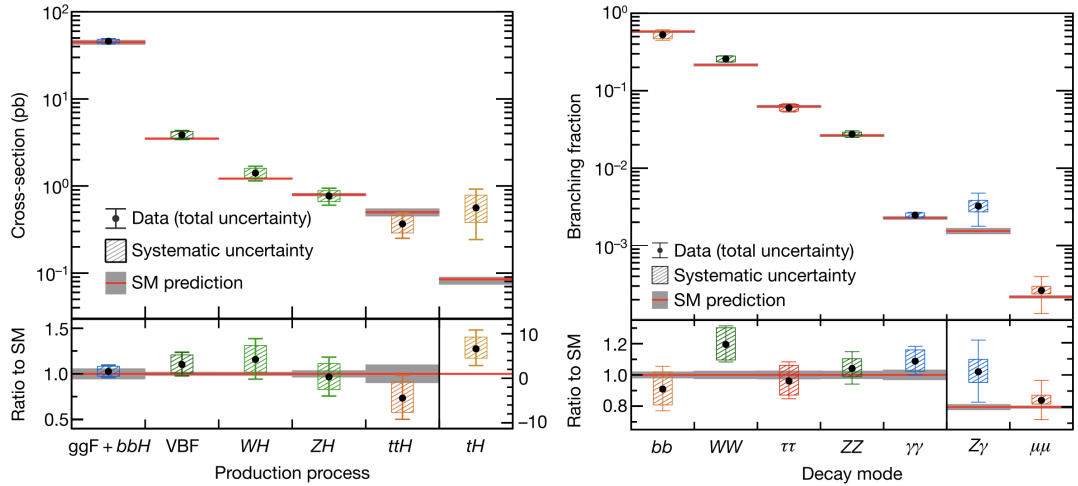
In the SM, this mechanism of symmetry breaking is embedded within the electroweak symmetry. This is based on two complex scalar fields in a weak isospin doublet (see equation (1.9)). Similar to the simplified case with one complex scalar field, the spontaneous symmetry breaking of the Higgs field, with its vacuum expectation value $v = -\mu^2 / \lambda$ and free parameter μ and λ of the potential leads to the generation of mass terms.

$$\phi = \begin{pmatrix} \phi^+ \\ \phi^0 \end{pmatrix} = \frac{1}{\sqrt{2}} \begin{pmatrix} \phi_1 + i\phi_2 \\ \phi_3 + i\phi_4 \end{pmatrix} \quad (1.9)$$

This spontaneous symmetry breaking of the electroweak symmetry generates mass terms for the two W-bosons, the Z-boson, and a massless boson in agreement with the photon (here denoted as A) with weak mixing angle θ_W and weak coupling constant g_W (see equation (1.10)).

$$\begin{aligned} m_W &= \frac{1}{2} g_W v \\ m_Z &= \frac{1}{2} \frac{g_W}{\cos \theta_W} v \\ m_A &= 0 \end{aligned} \quad (1.10)$$

The excitation of the Higgs field, the Higgs boson (with $m_h^2 = 2\lambda v^2$), was discovered by the [ATLAS](#) and [CMS](#) collaborations in 2012 [3, 4]. In the last 10 years, there have been extensive precision measurements of not only the Higgs mass but a multitude of its production and decay modes. A most recent discussion on developments and a detailed summary of the latest measurements of the Higgs bosons properties throughout the last ten years since its discovery can be found in [5, 30]. An overview of the production and decay modes of the Higgs boson can be found in Figure 1.2.



(a) Higgs Production mechanisms and their cross section (b) Higgs decay modes and their branching ratio

Figure 1.2: Overview of most recent ATLAS Higgs results on the production cross sections (a) as well as decay mode branching fraction (b) [5]. The dominant production processes include gluon-gluon Fusion (ggF) and Vector Boson Fusion (VBF), with Higgs production associated with other particles at smaller cross section values.

1.1.3 Particle spectrum and interactions of the Standard Model

With the Higgs boson as the latest part of the [SM](#), this sums up its particle content as shown in Table 1.1. This includes three generations of neutrinos and leptons, as well as three generations of quarks. As can be seen, for neutrinos, an upper limit on the masses is included. Massive neutrinos in itself present an extension to the [SM](#) and are necessary through evidence of neutrino oscillations [31].

Below an energy scale of the order of 246 GeV (the *electroweak* scale), the interactions of the [SM](#) can be split into electromagnetic, weak and strong interactions:

Electromagnetic interactions are mediated through massless photons. The underlying symmetry group is the U(1) symmetry of Quantum Electrodynamics ([QED](#)). The conserved charge associated with this gauge symmetry is the electric charge. The neutral photon does not self-interact. Photons couple to left- and right-handed particles irrespectively.

Weak interactions are mediated through W- and Z-bosons. The $SU(2)_L$ symmetry only applies to left-handed particles and is able to transform isospin states, therefore creating weak

Particle	electric charge	spin	colour	weak I_3 (L)	mass
electron e	-1	1/2	-	+1/2	0.511 MeV
electron neutrino ν_e	0	1/2	-	-1/2	< 1.1 eV
muon μ	-1	1/2	-	+1/2	105.66 MeV
muon neutrino ν_μ	0	1/2	-	-1/2	< 0.19 MeV
tau τ	-1	1/2	-	+1/2	1776.86 MeV
tau neutrino ν_τ	0	1/2	-	-1/2	< 18.2 MeV
up quark u	+ 2/3	1/2	r,g,b	+1/2	2.2 MeV
down quark d	-1/3	1/2	r,g,b	-1/2	4.7 MeV
charm quark c	+2/3	1/2	r,g,b	+1/2	1.27 GeV
strange quark s	-1/3	1/2	r,g,b	-1/2	93.4 MeV
top quark t	+2/3	1/2	r,g,b	+1/2	172.69 GeV
bottom quark b	-1/3	1/2	r,g,b	-1/2	4.18 GeV
photon γ	1	-	0	0	0
gluon g	0	1	8	0	0
W boson W	+/- 1	1	-	+/- 1	80.377 GeV
Z boson Z	0	1	-	0	91.1876 GeV
H boson h	0	0	-	0	125.25 GeV

Table 1.1: Overview of all SM particles and their properties, with the third weak isospin component I_3 [32]

isospin doublets of up type quarks (u,c,t) and down type quarks (d,s,b). Through its left-handed only coupling, the weak interaction is parity and charge-parity violating.

Strong interactions are mediated through massless gluons, described by Quantum Chromodynamics (QCD). They are gauge bosons of the $SU(3)_c$ symmetry group, with conserved colour charge. Values of the colour charge can be red (r), green (g) and blue (b). Gluons are self-interacting. This has two interesting phenomenological consequences (discussed in detail in [18]): the coupling constant increases for low energies and gets close to one, therefore quarks and gluons are *confined*. They will form a bound state through strong interactions and have not been observed free. Moreover, at high energies, quarks become *asymptotically free*, due to the decrease of the coupling constant with energy. Consequently, at high energies perturbation theory can be used to predict QCD interactions.

1.2 Shortcomings of the Standard Model

The Standard Model as described above can account for a wide spectrum of phenomena and has been put to a stringent test by various experiments. Nevertheless, there are open questions and unexplained phenomena that cannot be explained by the SM, hinting to a need for an extension of our current best model beyond the SM.

1.2.1 Dark Matter

A hint towards the incompleteness of the SM is the presence of Dark Matter (DM). First hints to the presence of non-luminous matter in galaxies has been found by Zwicky in 1933 [10], who

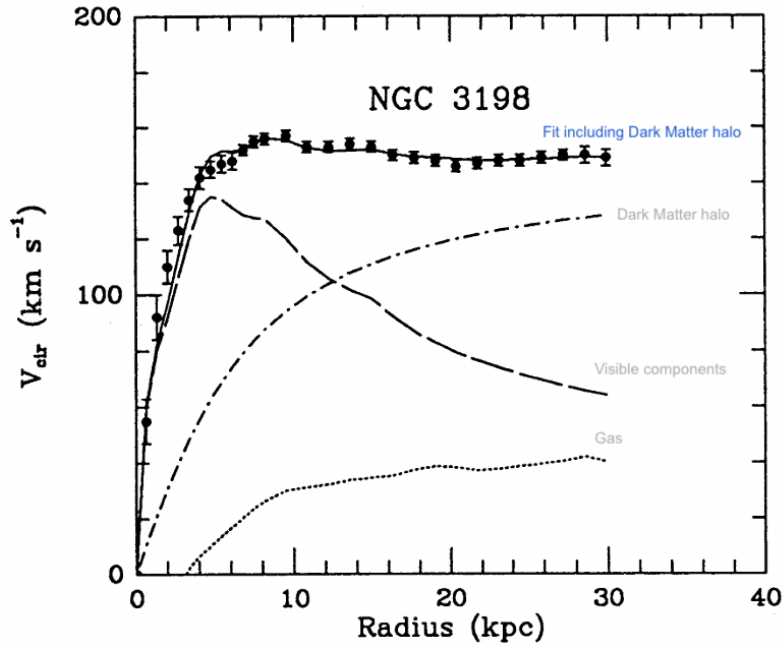


Figure 1.3: Exemplary analysis of rotation curves, here showing observations in galaxy NGC 3198. The dotted curve is the galaxy's gas component, dashed line is its visible components. The dotted-dashed line is visualising a contribution of a Dark Matter halo, with the solid line a fit to the data points including all components. Figure adapted from [12].

found that the mass of the galaxies in the Coma cluster based on luminosity calculations was not providing enough gravitational pull to prevent galaxies from escaping the cluster. Rubin and Kent's observation of rotation curves in galaxies [11] in dependence to the distance to the galaxy's centre was important in 1970. The velocity of galaxy components on the outer arms of the galaxy exceeded the expected rotational velocity in their measurements. This can be explained through the presence of non-luminous, gravitational matter in a halo around the galaxies centre, as illustrated on an exemplary galaxy, NGC 3198 in Figure 1.3.

An additional hint for the presence of Dark Matter in our universe is offered through analyses of the Cosmic Microwave Background (CMB), as done by the Planck Collaboration [13], showing a 27% Dark Matter composition in our universe. Lessons about the properties of DM can be gained by analysing colliding galaxy clusters and specifically their interaction. The bullet cluster is a prominent example of such an analysis, offering limitations on the self-interaction of DM, hinting to Dark Matter consisting of weakly interacting, massive particles (WIMPs) [14, 15]. An alternative possible theoretical approach apart from the presence of Dark Matter would be the modification of gravity models, governed by general relativity. A discussion of this group of theories in comparison with the Dark Matter approach is outside the scope of this thesis.

1.2.2 Matter-Antimatter asymmetry

Our visible universe is dominantly made up of matter, which can be measured through observations of the CMB, for example through the Wilkinson microwave anisotropy probe, whose measurements result in a matter-antimatter asymmetry of 6×10^{-10} [7, 8, 33]. To achieve such an asymmetry between matter and antimatter in a theory describing our universe, Sakharov defined a set of conditions necessary [9]:

1. Presence of at least one process violating baryon number conservation
2. CP violating aspects in the overall theory
3. Interactions outside of equilibrium

These three conditions are all fulfilled within the **SM**: The first condition can be met in **SM** quantum effects associated with weak interactions. A CP violating phase is present in the CKM (Cabibbo-Kobayashi-Maskawa) matrix, connecting the quark mass and gauge eigenstates. An interaction outside the equilibrium is given through electroweak phase transitions. Despite the presence of all three Sakharov conditions, the matter-antimatter asymmetry resulting from the **SM** processes is not enough to explain the observed matter-antimatter asymmetry. This is a further limitation of the current **SM**, motivating extensions **BSM**.

1.2.3 Hierarchy Problem

The matter-antimatter asymmetry as well as Dark Matter present phenomenological motivations of physics beyond the current **SM**. A theoretical, as well as experimentally motivated question, is the nature of the Higgs mass. As discussed in section 1.1.2, the Higgs-boson has been observed at 125 GeV [32]. The Hierarchy problem connected with the Higgs-bosons mass here describes the following consideration (adapted from [6]):

Since the Higgs boson couples to both fermions as well as bosons, its mass itself, given through its propagator and all loop corrections to it, is influenced by the fermion and boson masses. The correction terms of these contributions are given in equation (1.11) and (1.12) for fermion and boson (scalar) contributions, respectively. If the **SM** is assumed to only be valid until a certain energy scale Λ_{UV} , this cut-off scale is entering the Higgs loop corrections. A well-motivated cut-off scale would be the Planck scale, at which gravitational effects reach similar orders of magnitude to the interactions governed within the **SM**.

$$\Delta m_{H,\text{fermion}}^2 = -\frac{|\lambda_f|^2}{8\pi^2} \Lambda_{UV}^2 + \dots (\propto m_f) \quad (1.11)$$

$$\Delta m_{H,\text{scalar}}^2 = \frac{\lambda_S}{16\pi^2} [\Lambda_{UV}^2 - 2m_S^2 \ln(\Lambda_{UV}/m_S) + \dots] \quad (1.12)$$

With this cut-off at the Planck scale, corrections to the Higgs mass would include multiple orders of magnitudes. This would require artificial fine-tuning to generate the Higgs boson observed mass of 125 GeV.

1.3 Supersymmetry

This artificial fine-tuning necessary to resolve the hierarchy problem could be avoided if there would be a symmetry in the **SM**, connecting fermions and bosons. This symmetry can be

provided by an extension of the **SM** called supersymmetry. A discussion of supersymmetry and its phenomenology relevant to this thesis will be given in the following, based on discussions in [6]. Supersymmetry is generated through a fermionic generator Q , transforming a fermion $|f\rangle$ into a boson $|b\rangle$ and vice-versa:

$$\begin{aligned} Q|b\rangle &= |f\rangle \\ Q|f\rangle &= |b\rangle \end{aligned} \tag{1.13}$$

Following from the properties of the **SUSY** generator, and namely its commutation with space-time translations, the masses of the connected fermion and boson are equal. Supersymmetry would connect each mass correction to the Higgs-boson originating from fermionic loop corrections to a bosonic loop correction and vice-versa. Given the opposite sign in the terms in equation 1.11 and (1.12), thus cancelling the quadratic divergences.

1.3.1 Soft SUSY breaking

Supersymmetry would be an unbroken symmetry if the supersymmetric partners to the **SM** particles would have the same masses as their counterparts. Since we have not yet observed any hints for supersymmetric particles at colliders, **SUSY** particles must be heavier than their **SM** partner. Therefore **SUSY** needs to be a broken symmetry. An additional SUSY breaking term can be introduced in the Lagrangian [6]:

$$\mathcal{L} = \mathcal{L}_{SUSY} + \mathcal{L}_{soft} \tag{1.14}$$

This Lagrangian is only including *soft* terms to avoid quadratic divergences in the Higgs mass loop corrections. The soft breaking is introducing new parameters determining the supersymmetric particles' masses into the Minimal Supersymmetric Standard Model (**MSSM**), leading to a large number of free parameters. The spontaneous breaking of supersymmetry is assumed to happen in a hidden sector with different assumptions on the mediators between this breaking in the hidden sector to lower energies.

1.3.2 Particle spectrum of the MSSM

The smallest possible supersymmetric extension of the **SM** is the Minimal Supersymmetric Standard Model (**MSSM**). In this model fermions and bosons are paired into supermultiplets, each **SM** particle acquiring a supersymmetric partner. *Chiral* multiplets pair **SM** spin 1/2 fermions with a supersymmetric complex scalar field. **SM** bosons with spin 1 are forming a *gauge supermultiplet* with supersymmetric fermions. The **SM** vector bosons (W^+ , W^- , W_0 and B_0) **SUSY** partners are referred to as gauginos (Wino, Bino). In table 1.2, an overview of the supersymmetric particles in the **MSSM** is given. Here a differentiation between their gauge and mass

Names	Spin	P_R	Gauge Eigenstates	Mass Eigenstates
Higgs bosons	0	+1	$H_u^0 H_d^0 H_u^+ H_d^-$	$h^0 H^0 A^0 H^\pm$
squarks	0	-1	$\tilde{u}_L \tilde{u}_R \tilde{d}_L \tilde{d}_R$	(same)
			$\tilde{s}_L \tilde{s}_R \tilde{c}_L \tilde{c}_R$	(same)
			$\tilde{t}_L \tilde{t}_R \tilde{b}_L \tilde{b}_R$	$\tilde{t}_1 \tilde{t}_2 \tilde{b}_1 \tilde{b}_2$
sleptons	0	-1	$\tilde{e}_L \tilde{e}_R \tilde{\nu}_e$	(same)
			$\tilde{\mu}_L \tilde{\mu}_R \tilde{\nu}_\mu$	(same)
			$\tilde{\tau}_L \tilde{\tau}_R \tilde{\nu}_\tau$	$\tilde{\tau}_1 \tilde{\tau}_2 \tilde{\nu}_\tau$
neutralinos	1/2	-1	$\tilde{B}^0 \tilde{W}^0 \tilde{H}_u^0 \tilde{H}_d^0$	$\tilde{N}_1 \tilde{N}_2 \tilde{N}_3 \tilde{N}_4$
charginos	1/2	-1	$\tilde{W}^\pm \tilde{H}_u^+ \tilde{H}_d^-$	$\tilde{C}_1^\pm \tilde{C}_2^\pm$
gluino	1/2	-1	\tilde{g}	(same)
goldstino (gravitino)	1/2 (3/2)	-1	\tilde{G}	(same)

Table 1.2: Particle content of the **MSSM**, with the sfermion mixing of the first two families assumed to be negligible, from [6]. Here $\tilde{N}_{1,2,3,4}$ is equivalent to $\tilde{\chi}_{1,2,3,4}^0$ and $\tilde{C}_{1,2}^\pm$ to $\tilde{\chi}_{1,2}^\pm$. The R-Parity P_R as defined in equation (1.15) is listed highlighting its different values for **SM** particles and **SUSY** particles.

eigenstates is made, since the gauge eigenstates are in some cases not equivalent to their mass eigenstates. Some of these cases are discussed below.

In table 1.2 P_R , called R-parity is introduced. This is defined as given in equation (1.15), with the baryon number B , lepton number L and spin s .

$$P_R = (-1)^{3(B-L)+2s} \quad (1.15)$$

If R-Parity conservation is assumed within the **MSSM** this has the following phenomenological consequences:

- Each **SUSY** particle must eventually decay into an odd number of **LSPs**.
- **SUSY** particles are pair produced.
- The **LSP** is stable and cannot further decay into **SM** particles. If the **LSP** is only interacting weakly with other particles and is electrically neutral, it can provide the right relic **DM** density and can therefore be a potential **DM** candidate.

The decision to conserve R-parity is well motivated phenomenologically since it is preventing proton decay, which has not been experimentally observed.

The gaugino fields of the MSSM mix with each other since their quantum numbers are identical. This leads to neutral and charged mass eigenstates (called neutralinos and charginos). This mixing is visible in the MSSM Lagrangian ((1.16), (1.17)) in the mixing matrices, given in (1.18) and (1.19) [6].

$$\mathcal{L}_{\text{neutralino mass}} = -\frac{1}{2}(\psi^0)^T \mathbf{M}_{\tilde{\chi}_j^0} \psi^0 + c.c., \quad (1.16)$$

$$\text{with } \psi^0 = (\tilde{B}^0, \tilde{W}^0, \tilde{H}_d^0, \tilde{H}_u^0)$$

$$\mathcal{L}_{\text{chargino mass}} = -\frac{1}{2}(\psi^\pm)^T \mathbf{M}_{\tilde{\chi}_i^\pm} \psi^\pm + c.c., \quad (1.17)$$

$$\text{with } \psi^\pm = (\tilde{W}^+, \tilde{H}_u^+, \tilde{W}^-, \tilde{H}_d^-)$$

The parameters of the mixing matrices originate from the soft **SUSY** breaking Lagrangian, $\mathcal{L}_{\text{soft}}$. M_1 and M_2 are the bino and wino mass parameters respectively, μ the higgsino mass parameter. The vacuum expectation values $\langle H_{u/d}^0 \rangle$ are noted as $v_{u/d}$, g and g' describe the **SM** coupling constants.

$$\mathbf{M}_{\tilde{\chi}_i^0} = \begin{pmatrix} M_1 & 0 & -g'v_d/\sqrt{2} & g'v_u/\sqrt{2} \\ 0 & M_2 & gv_d/\sqrt{2} & -gv_u/\sqrt{2} \\ -g'v_d/\sqrt{2} & gv_d/\sqrt{2} & 0 & \mu \\ g'v_u/\sqrt{2} & -gv_u/\sqrt{2} & -\mu & 0 \end{pmatrix} \quad (1.18)$$

$$\mathbf{M}_{\tilde{\chi}_j^\pm} = \begin{pmatrix} \mathbf{0} & \mathbf{X}^T \\ \mathbf{X} & \mathbf{0} \end{pmatrix}, \text{ with } \mathbf{X} = \begin{pmatrix} M_2 & gv_u \\ gv_d & \mu \end{pmatrix} \quad (1.19)$$

Depending on the comparable size of the **MSSM** parameters M_1, M_2 and μ , neutralinos can be bino-dominated ('bino-like'), wino-dominated ('wino-like'), higgsino-dominated ('higgsino-like') or mixed with no clear dominating component.

Similar to the gaugino mixing described above, the third generation sleptons $\tilde{\tau}_1, \tilde{\tau}_2$ can have mass eigenstates differing from their gauge eigenstates ($\tilde{\tau}_L, \tilde{\tau}_R$).

1.3.3 Interactions in the MSSM

Gauginos can be produced at hadron colliders through the following interactions, depending on their field content:

Gauginos are pair-produced as a consequence of R-parity conservation. The pair production relates to **SUSY** particles in general, therefore also a chargino-neutralino production as shown in Figure 1.4 (last row). These feynman diagrams showing example production modes are governed by the same interaction vertices as the decay of gaugino particles and leptons. This would for example allow for the decay of a $\tilde{\tau}$ particle into a bino-like neutralino as well as a **SM** tau lepton, which can be constructed using the \tilde{B} vertex shown in figure 1.5.

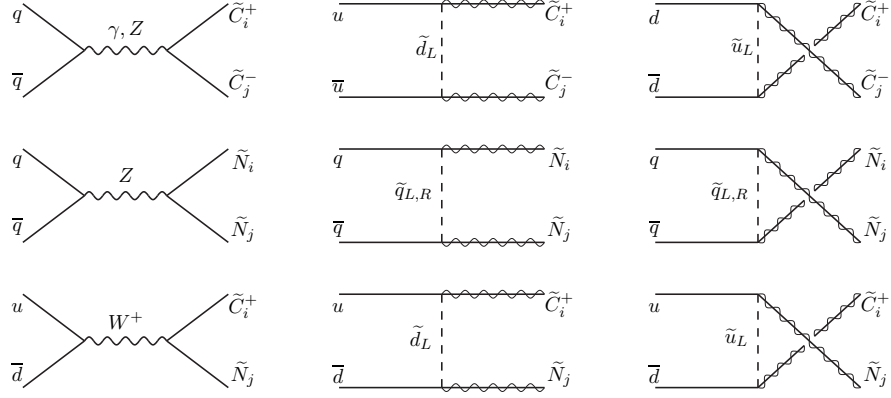


Figure 1.4: Gaugino production mechanisms at hadron colliders, adapted from [6]. Here $\tilde{N}_{1,2,3,4}$ is equivalent to $\tilde{\chi}_{1,2,3,4}^0$ and $\tilde{C}_{1,2}^\pm$ to $\tilde{\chi}_{1,2}^\pm$.

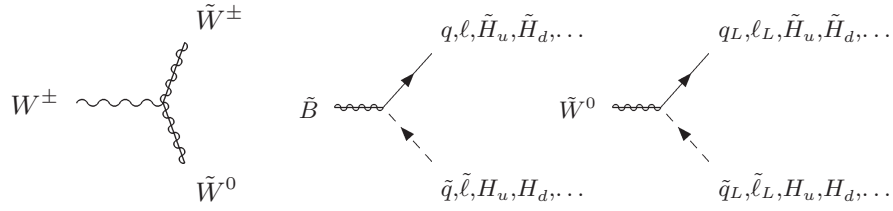


Figure 1.5: Wino and bino field vertices in the MSSM [34].

1.4 The bigger picture

As discussed in section 1.3, the **MSSM** has a large set of free parameters. Most notably, the masses of all particles in the **MSSM** are free. This significantly impacts the expected signatures within particle detectors as well as the cross sections. A multitude of searches for supersymmetric particles are carried out at the **LHC** with the help of *simplified models*. These models present a slice of parameter space of the **MSSM**, often assuming 100% branching ratios in their decay chains as well as expecting particles not participating in the process to be decoupled. The parameter space is reduced to parameters accessible to collider experiments such as the particle masses and cross sections. The concept of simplified models serves multiple purposes (a comprehensive discussion can be found in [35]): determine the limits of search sensitivity, study the properties of new physics signals and derive limits on more general models. When considering results of a search based on simplified models, identifying the boundaries of sensitivity such as reconstruction efficiencies helps experimentalists and theorists realize uncovered and unaccessible detector signatures and serve as a reference to other theoretical models with similar decay topologies. In the case of an observation of a new physics signal, simplified models help understand the properties such as particle masses of such a new signal, leading to broader model development. Lastly, search results of simplified models can be used to be interpreted in more general models. This can be done through upper limits on observable signal events and compared to predictions of other models. Using simplified models, the **ATLAS** Collaboration has a wide search program for supersymmetric particles. Given that the **LHC** is a hadron collider, the production of squarks and gluinos is an initially most prom-

ising window into **SUSY** searches. An overview of the most recent limits (as of March 2022) on the production of gluinos (\tilde{g}) and their consecutive decay into the lightest **SUSY** particles, here either the lightest neutralino, $\tilde{\chi}_1^0$, or the gravitino, \tilde{G} are given in Figure 1.6.

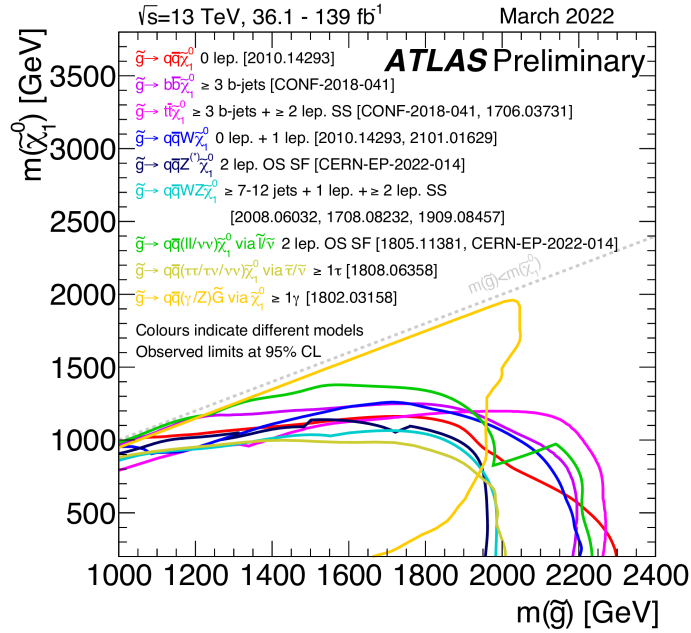


Figure 1.6: Latest summary of gluino mass exclusion limits by ATLAS for various simplified models . Shown are exclusion limits at 95 % Confidence Level in a lightest neutralino ($\tilde{\chi}_1^0$) versus gluino (\tilde{g}) mass plane. Different simplified models are shown in different coloured lines [36].

Different simplified models are shown in different colours. As can be seen for example in the light blue line, showing a simplified model of $\tilde{g} \rightarrow q\bar{q}WZ\tilde{\chi}_1^0$, different consecutive decays of the **SM** bosons, leading to different final states (here either $\geq 7 - 12$ jets, one or at least two light leptons) can be investigated. These analysis results can be combined to lead to results in a simplified model considering all consecutive **SM** boson decays. Gluino masses up to 2 TeV have been excluded for the assumption of a massless $\tilde{\chi}_1^0$, for various decay modes. Similar searches for the production of gluinos have been carried out by the CMS Collaboration, resulting in comparable exclusion limits on gluino masses up to around 2 TeV [37], as displayed in Figure 1.7.

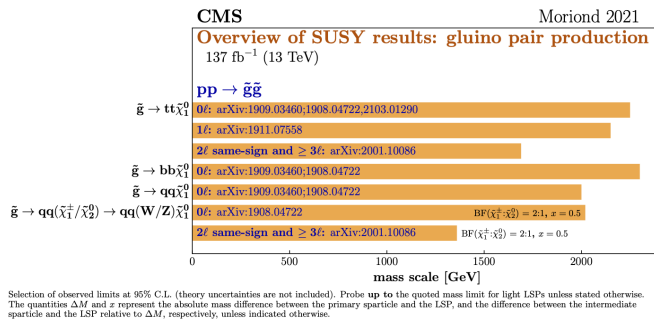


Figure 1.7: Latest summary of gluino mass exclusion limits by CMS for various simplified models [37]. The excluded mass scale for the gluino is given for light LSPs on the x-axis, with the associated simplified model and final state highlighted in each bar.

A further example of extensive **SUSY** searches with the ATLAS detector are the searches for

the scalar top quark. Due to the top quarks' large coupling to the Higgs boson, its scalar, the supersymmetric partner is of particular interest for naturalness arguments. In Figure 1.8, a summary of the latest searches for the pair production of the top squark and consecutive decay to the $\tilde{\chi}_1^0$ is given. Three simplified models with different consecutive decays of the stop are considered, therefore showing 3 different kinematically forbidden regions. Stop masses up to 1250 GeV are excluded for a massless LSP. Comparable stop masses for the same simplified model have been excluded by the CMS Collaboration [37] (see Figure 1.9).

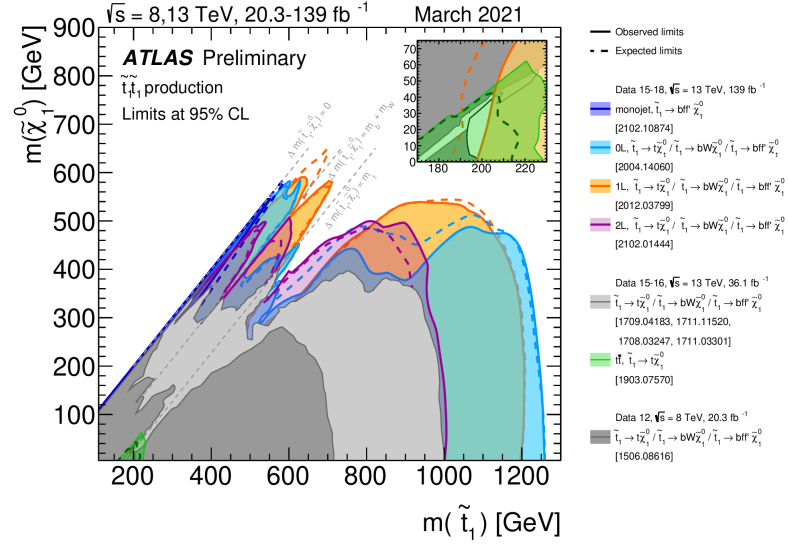


Figure 1.8: Latest exclusion plots summarising searches for pair production of stop particles by ATLAS [36]. The limits shown are given at 95 % confidence level, with the stop mass on the x-axis and the $\tilde{\chi}_1^0$ mass on the y-axis.

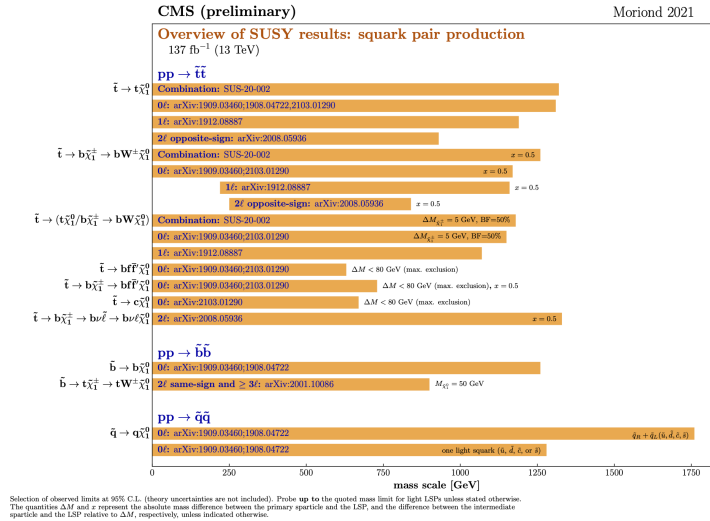


Figure 1.9: Latest exclusion plots summarising searches for pair production of stop particles by CMS [37]. The x-axis is showing the 95 % confidence level exclusion limit on various squark masses. The bars along the y-axis highlight the simplified models considered to yield the exclusion limits.

So far, we have not observed hints for SUSY through these production mechanisms. As will be further discussed in section 5.1, the high masses excluded for these strong interaction production mechanism motivates investigations into electroweak production of SUSY, which will be the main topic of this thesis.

EXPERIMENTAL SETUP

2

Ignore the glass ceiling and do your work. If you're focusing on the glass ceiling, focusing on what you don't have, focusing on the limitations, then you will be limited.

Ava DuVernay

The work in this thesis has been performed using data from the [ATLAS](#) detector, one of the particle detectors recording collisions of protons accelerated by the [LHC](#) particle accelerator at [CERN](#). In the following chapter, an introduction to the [LHC](#) is given in section 2.1, followed by a discussion of the [ATLAS](#) detector in section 2.2. The discussion is focused on aspects important to the analyses of this thesis.

2.1 LHC

The [LHC](#) [38,39] is the largest particle accelerator in the world. It is located at the European Organization for Nuclear Research ([CERN](#)), in Geneva, Switzerland. With its 27 km circumference, the accelerator ring is partially located in Switzerland and partially in France, between 50-175 meters underground. The [LHC](#) was designed to accelerate protons in two separate beam pipes up to a centre of mass energy of 14 TeV. It is also capable of accelerating heavy ions. To keep the protons and heavy ions on the accelerator ring, overall 9593 magnets are used. These magnets include superconducting dipole and quadrupole magnets, cooled down to 1.9 K (-271 °C). The dipole magnets generate a magnetic field of 8.3 T.

Before the protons enter the [LHC](#), a chain of accelerators is used (see Fig. 2.1): starting from a hydrogen bottle, negative hydrogen ions are fed into the Linear Accelerator 2 (LINAC2) and are accelerated up to 50 MeV. Before getting inserted into the Proton Synchrotron Booster ([PSB](#)) the ions are stripped of their electrons only leaving protons. The up to 2 GeV accelerated protons are then inserted into the Proton Synchrotron (PS), followed by the Super Proton Synchrotron

CERN's Accelerator Complex

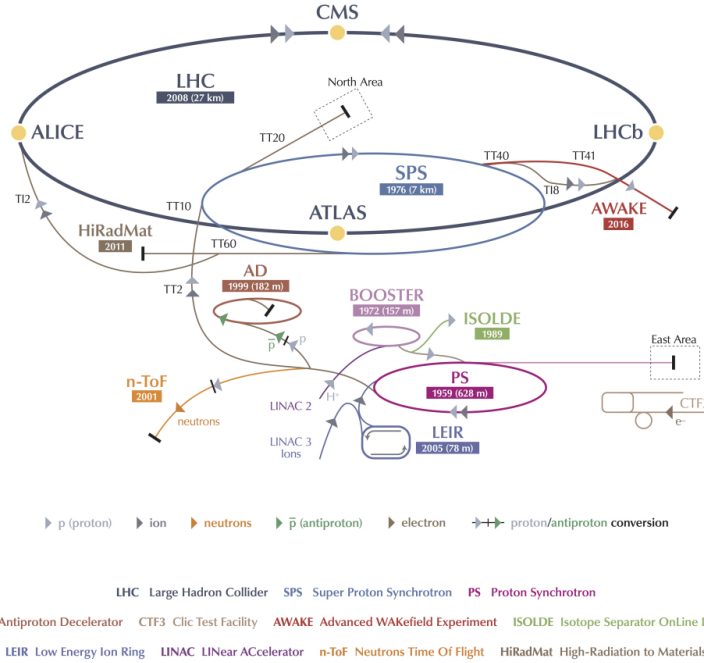


Figure 2.1: Overview of the CERN accelerator facilities, including the acceleration chain leading up to the LHC [40].

(SPS) which accelerates the protons from 60 GeV to 450 GeV before feeding the LHC. Overall 8 radiofrequency cavities can push the energy of the protons in the LHC up to 14 TeV.

The LHC so far provided proton and heavy ion beams for two data-taking periods. Between 2009 and 2013 (known as Run-1), the LHC was operating with a centre-of-mass energy (\sqrt{s}) of 7 TeV and 8 TeV. After a long shutdown (LS1), the second run (Run-2) started in 2015 and ended in 2018, providing 13 TeV collisions to the experiments around the LHC ring. In Figure 2.1 visualised yellow dots, there are four interaction points, housing the ALICE [41], LHCb [42], CMS [43], ATLAS [44], LHCf [45], TOTEM [46], MoEDAL [47] experiments, among many other experiments.

The instantaneous luminosity [39] is a measure of the accelerator:

$$\mathcal{L} = \frac{N_b^2 n_b f_{rev} \gamma_r}{4\pi \epsilon_n \beta^*} F \quad (2.1)$$

With N_b the number of particles per bunch, the bunches per beam n_b , revolution frequency f_{rev} , the relativistic gamma factor γ_r , ϵ_n normalised transverse beam emittance as well as β^* , the beta function at the collision point, determining the transverse spread of the particle beam. The correction term F takes into account the beam crossing angle.

$$N_{event} = L_{int} \sigma_{event} = \sigma_{event} \int \mathcal{L} dt \quad (2.2)$$

A measure for the recorded data is the integrated luminosity over time, (see equation (2.2)), connecting the luminosity with the number of events. This can be seen for each month during Run-2 in Figure 2.2. This illustrates the overall 156 fb^{-1} of a proton-proton collisions delivered to *ATLAS* by the *LHC* as well as the 139 fb^{-1} of data collected by *ATLAS* with detector conditions good enough to use the events in data analysis.

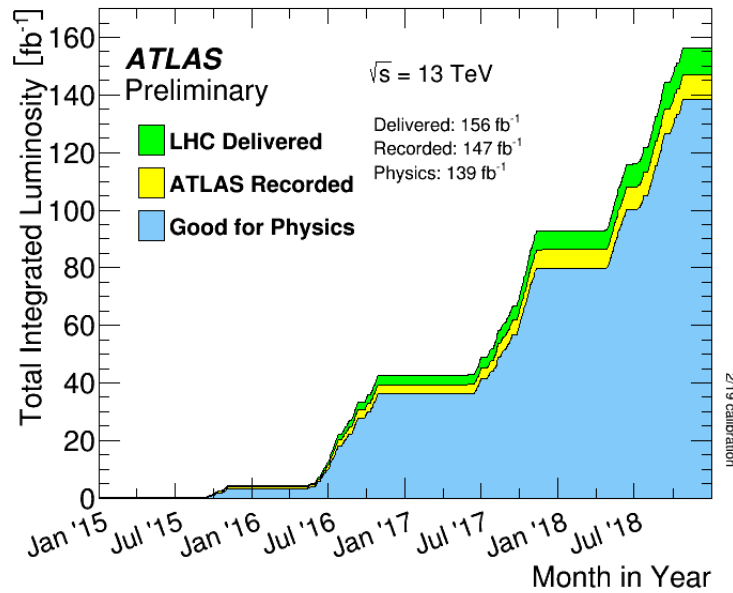


Figure 2.2: Summary of the luminosity delivered by the LHC, recorded by the ATLAS detector as well as the overall data good to use for physics analyses [48].

As already hinted to in equation (2.1), protons in the acceleration chain are accelerated in so-called bunches to generate high instantaneous luminosity. As a consequence, many proton-proton interactions can happen during one crossing of bunches. In Figure 2.3, the mean number of interactions per bunch crossing is given for all years of Run-2 data-taking. This so-called *pile-up* reached above 70 number of interactions per bunch crossing in 2017.

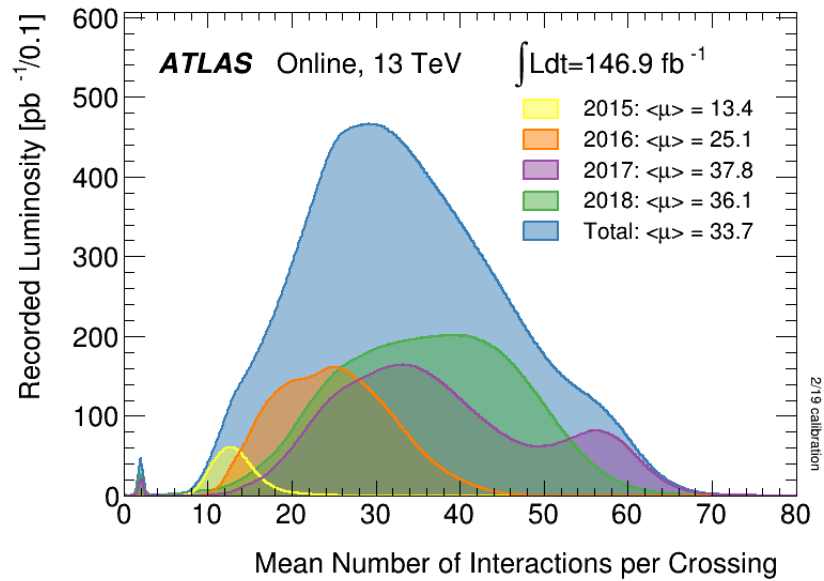


Figure 2.3: Pileup conditions throughout Run-2 [48].

2.2 ATLAS

The [ATLAS](#) detector is located at Point 1 along the [LHC](#). This is the only [CERN](#) site along the LHC ring with access to a main experiment, the [SPS](#) as well as the LHC. The overall structure is comparable to a barrel, leading to the centre part of the detector being referred to as the barrel, as well as the large, 25m in diameter, wheels on each side referred to as endcaps. With its 25 meters tall and 44 meters length, [ATLAS](#) is the largest particle detector built on a collider so far. It consists of multiple sub-systems and sub-detectors, all built with different purposes in mind, targeting momentum and energy reconstruction. [ATLAS](#) provides hermetic coverage around the beam axis, enabling detection of all charged particles generated in the collisions in the plane orthogonal to the beam axis. This is particularly important in searches for new physics, relying on analyses of momentum balances in the orthogonal plane such as discussed within this thesis. An illustration of the design of [ATLAS](#) is given in Figure 2.4. It is built up of multiple layers, starting from the innermost component, the Inner Detector ([ID](#)), providing tracking hits close to the beam pipe. Surrounding the [ID](#) is a system of two calorimeters. The outermost parts of [ATLAS](#) are built by the muon spectrometer, providing momentum reconstruction for muons passing through the inner detector layers. Arguably one of the most striking features of [ATLAS](#) is given through its magnet system. Three superconducting Niobium-Titanium ([NbTi](#)) magnets span an overall length of 26m. The first magnet system, the central solenoid, is wrapped around the [ID](#), providing a 2 T axial magnetic field to curve the [ID](#) tracks of charged particles. The largest magnet parts are the eight barrel toroid coils, intertwined with the outer muon system, providing a total magnetic field of 4 T (0.5 T per coil) to measure the momentum of muons. The toroid magnetic field is completed by the end-cap toroids, also generating a magnetic field up to 4T for muons leaving [ATLAS](#) close to the beam pipe.

Every component in [ATLAS](#) working together enables the reconstruction and identification of

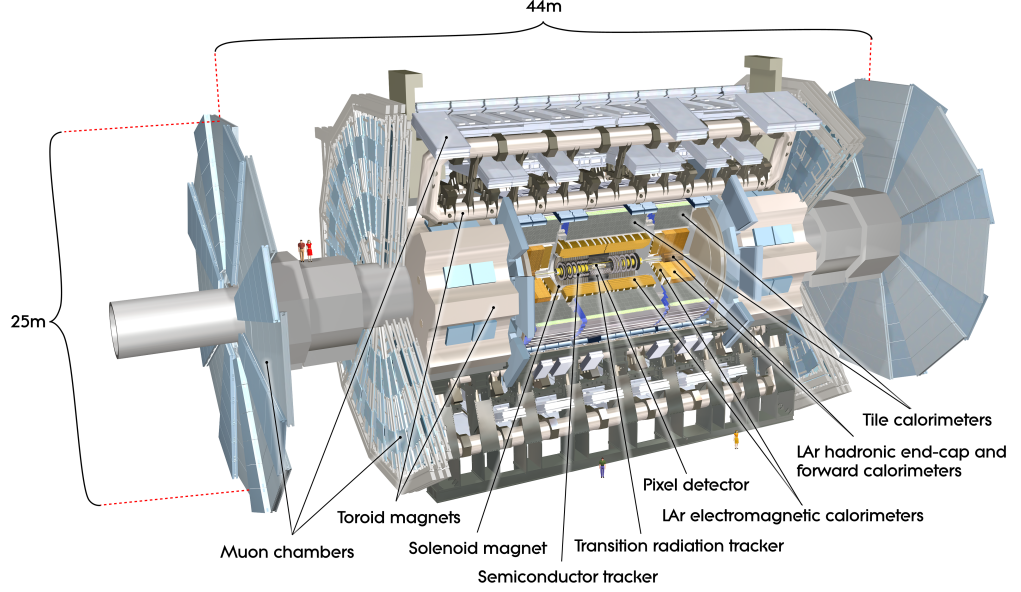


Figure 2.4: Overview graphic of the ATLAS detector design , with two people illustrated for scale reference [49].

a variety of particles with high precision. An overview of the design capabilities of **ATLAS** in terms of the momentum and energy resolution is given in Table 2.1, adapted from [44]. Here the resolution given lists first a stochastic term, measuring the uncertainty based on the statistically dominated interaction of a particle with the material, followed by a noise term, which accounts for uncertainties due to electronic noise in the readout process.

Detector component	Required resolution	η coverage	
		Measurement	Trigger
Tracking	$\sigma_{p_T}/p_T = 0.05\% p_T \oplus 1\%$	± 2.5	
EM calorimetry	$\sigma_E/E = 10\%/\sqrt{E} \oplus 0.7\%$	± 3.2	± 2.5
Hadronic calorimetry (jets)	barrel and end-cap	$\sigma_E/E = 50\%/\sqrt{E} \oplus 3\%$	± 3.2
	forward	$\sigma_E/E = 100\%/\sqrt{E} \oplus 10\%$	$3.1 < \eta < 4.9$
Muon spectrometer	$\sigma_{p_T}/p_T = 10\%$ at $p_T = 1$ TeV	± 2.7	± 2.4

Table 2.1: Performance goals of the **ATLAS** detectors' subsystems. Units are given in GeV. \oplus indicating a sum in quadrature of the single terms for the total uncertainty [44].

In the following, a brief overview of the detector is given; a more comprehensive description can be found in [44] as well as the Technical Design Reports of the subsystems, as cited throughout the description below.

2.2.1 ATLAS Coordinate system

The coordinate system used within **ATLAS** is used throughout this thesis and shortly described in the following [44]. The origin of the right-handed coordinate system is at the nominal interaction point, with the positive x-axis pointing towards the centre of the **LHC**. The x-y plane is perpendicular to the beam axis, defining the z-axis. Towards the surface defines the positive

y-axis. An azimuthal angle ϕ is defined around the beam axis, and a polar angle θ is the angle from the beam axis. Instead of θ the rapidity y is used for heavy objects:

$$y = \frac{1}{2} \ln[(E + p_z)/(E - p_z)] \quad (2.3)$$

Differences in Rapidity are invariant under boosts along the beam axis. For massless objects or relativistic objects ($m \ll p$), the pseudorapidity is used:

$$\eta = -\ln(\tan(\theta/2)) \quad (2.4)$$

To quantify the distance between two objects, ΔR is defined:

$$\Delta R = \sqrt{\Delta\phi^2 + \Delta\eta^2} \quad (2.5)$$

The transverse momentum and energy are defined in the x-y plane, with the transverse momentum given as $p_T = \sqrt{p_x^2 + p_y^2}$.

2.2.2 Inner Detector

A cross-section of the ID system [50] is shown in Figure 2.5, highlighting the distance of each subsystem from the beampipe. The innermost part of the ID is the IBL, followed by three layers of pixel detectors. At 299 mm radial distance from the beam pipe, four layers of SemiConductor Tracker (SCT) modules are located before the Transition Radiation Tracker (TRT), which extends the overall ID detector size to a radius of 1082 mm. The ID allows for particle track reconstruction within $|\eta| < 2.5$.

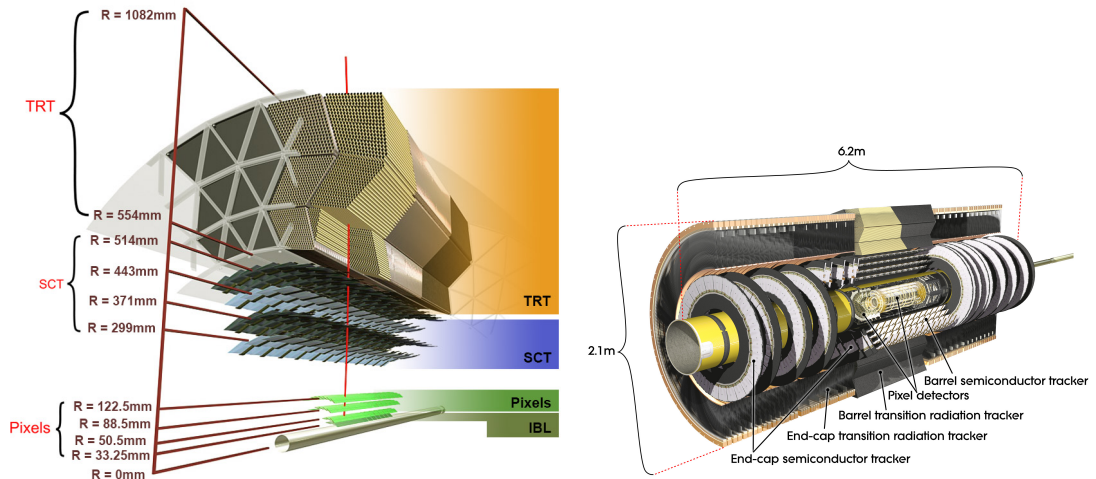


Figure 2.5: Slice view of the Inner Detector, highlighting each sub-detectors distance to the beampipe [51] (a) and cut-out view of the barrel and endcap components, not including the IBL [44] (b).

IBL - Insettable B-layer After Run-1, during a long shutdown in 2013-2014, the pixel detector system was subject to maintenance and upgrades. Within this set of upgrades, a 4th pixel layer at a 3.3 cm distance from a new, smaller beam pipe (33 mm outer radius, originally 36 mm). A

fourth pixel layer was a first in particle physics experiments [52, 53] and has led to significant improvements in interaction vertex reconstruction and identification of b-hadron jets.

Pixel Detector The innermost pixel layer, the IBL, is surrounded by three layers of pixel detectors, arranged in barrels around the beam pipe [54, 55]. The first layer is at a distance of 50.5 mm from the beam pipe's centre. As can be seen in Figure 2.5b, the end caps of the pixel layer consist of 3 disks around the beampipe, stretching the length of the pixel component of the ID to 1.4 m length along the beam axis. The pixel detector consists of overall 1744 pixel modules with a nominal size of $50\mu m \times 400\mu m$ in the (ϕ, z) plane (ϕ, r for the disk panels), comprising over 80 million readout channels. The pixel and IBL part of the ATLAS detector is crucial for tracking, providing 4 pixel hits over the entire ID pseudorapidity coverage ($|\eta| < 2.5$).

Semiconductor Tracker The pixel detector and IBL are located within SCT modules [56]. Similar to the pixel detector modules, the SCT modules are semiconductor-based, arranged into cylindrical layers around the beampipe in the barrel region, forming disks in the endcap. Since the SCT modules only provide precise location along one axis, two modules are combined back-to-back and rotated against each other to gain two dimensional spacial information. Four layers are arranged in the barrel, nine disks in each endcap side (see Fig. 2.5b). Including the endcap disks, the SCT extends up to $|z| < 2735\text{mm}$.

Transition Radiation Tracker The last part of the ID is the TRT [57], in the barrel stretching from 554 mm to 1082 mm radial distance. This detector is composed of 4 mm diameter straw tubes, arranged in parallel to the beam pipe or radially in the barrel and end-cap, respectively. Within $|\eta| < 2.0$, three barrel rings and 18 end-cap units provide typically 36 hits per track. The straws are intertwined with polypropylene fibres for passing through particles to create transition radiation. Inside the straws is a thin tungsten wire, collecting charges drifting through the straws gas mixture (Xe, CO₂ and O₂). The level of radiation and collected charges in each straw can be used to discriminate between electrons and charged pions. The TRT only offers spatial information in the $(R - \phi)$ plane, no information in the z-direction can be extracted due to the straws orientation.

2.2.3 Calorimeter System

The overall ID system is surrounded by two sets of calorimeters [44]. An Electromagnetic Calorimeter (ECAL) [58] in the inner most part, followed by a Hadronic Calorimeter (HCAL) [59] (see Figure 2.6). Both systems are designed to record the energy deposits of mainly electromagnetically interacting particles (electron, photons) or the energy of hadrons, based on hadronic interactions.

Both calorimeters are so-called sampling calorimeters with alternating layers of absorber and active material. The absorber layer triggers a shower development of consecutive interactions with the detector material, the active layer is detecting the signal. The shower development

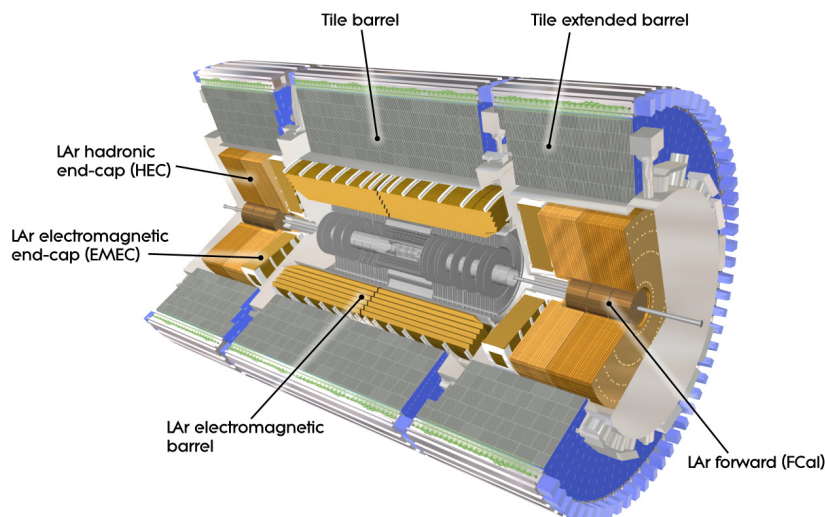


Figure 2.6: Illustration of the ATLAS calorimeter system [44].

and properties can be a helpful characteristic in particle identification. Overall, the calorimeters cover the $|\eta|$ range below 4.9. Two important quantities in connection with the calorimeters are the radiation length, X_0 , and the interaction length λ . The radiation length refers to the distance after which an electron's energy has been reduced to $1/e$ of its initial energy. The interaction length describes the mean free path before the occurrence of a hadronic interaction.

Liquid Argon Calorimeter Liquid Argon (LAr) calorimeters [58] are used in multiple parts of the calorimeter system. First, it is comprising the ECAL, with two half barrels covering the central detector region, with a small (4 mm) gap at $z = 0$ and one end-cap on each side of the beamline (see Fig. 2.7a). Additionally, the LAr technology is used for the hadronic calorimeters end-caps as well as a Forward Calorimeter (FCAL) ($3.1 < \eta < 4.9$). The active material is LAr, with copper and kapton electrodes for readout. The absorber is made of lead with stainless steel sheets. As can be seen in Figure 2.7a, an accordion symmetry is used to ensure homogeneous coverage all over ϕ .

In front of the ECAL between $|\eta| < 1.52$ in the barrel region and $1.5 < |\eta| < 1.8$ in the end cap, there is an additional layer of instrumented Liquid Argon, the *presampler*. This is included in order to account for energy losses of particles before entering the ECAL. The first layer of the ECAL has the finest granularity, comprising $4.3 X_0$, followed by the second layer of $16 X_0$ radiation lengths in depth and a third layer with coarse granularity. The total thickness in the barrel of the ECAL is over $22 X_0$, over $24 X_0$ in the endcap. In Figure 2.7b, the amount of material in front of the presampler as well as the accordion part of the calorimeters is given in radiation lengths. Within the region of $1.37 < |\eta| < 1.52$, a large amount of material is present. This is due to the transition between the barrel and end-cap cryostats, housing the calorimeters. This region is known as the *crack* region or transition region.

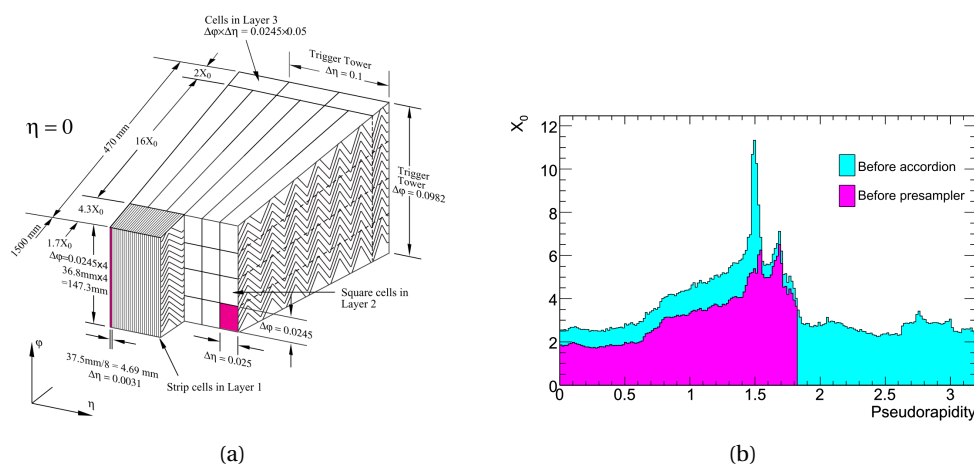


Figure 2.7: Visualisation of an **ECAL** slice at $\eta = 0$ (a), next to an overview of the material in terms of radiation lengths in front of the presampler and main **ECAL** (b). Both from [44].

Tile Hadronic Calorimeter The hadronic calorimeter is built of a tile calorimeter technology [59] in the barrel and extend barrel region (between $0 < |\eta| < 1.7$, see Figure 2.6). Similar to the Liquid Argon (**LAr**) calorimeter the tile calorimeter is a sampling calorimeter, with a steel absorber material as well as plastic scintillator tiles as active material. The scintillator tiles are combined with optical fibres and photo-multipliers for signal readout. In the barrel, the tile calorimeter has an overall depth of roughly 9.7 interaction lengths.

2.2.4 Muon System

The outermost part of the **ATLAS** detector is the Muon Spectrometer (**MS**) [60]. It is embedded within the 4 T magnetic field generated by the barrel and endcap toroid magnets. In Figure 2.8, a quarter of the muon system is visualised, highlighting the different subsystems. Monitored Drift Tubes (**MDT**s) and Resistive-Plate Chambers (**RPC**s) form three layers around the barrel, Cathode Strip Chambers (**CSC**s) are used close to the beam pipe. The *Big Muon wheels*, forming the "lids" of the **ATLAS** barrel structure, are comprised of Thin-Gap Chamber (**TGC**) and **MDT** subdetectors. A short overview of the subsystems is given in the following.

MDT - Monitored Drift Tubes The **MDT** subdetectors of the muon spectrometer are drift tubes with a diameter of 29.97 mm. They are filled with 93% Ar, 7% CO₂ and have a tungsten-rhenium wire in the middle. There are in total 1171 **MDT** chambers, each layer with up to eight layers of drift tubes. Overall 354240 tubes cover a pseudorapidity range up to $|\eta| < 2.7$, providing high precision track coordinates perpendicular to the magnetic field. In the innermost end-cap layer, the **MDT** chambers are replaced by **CSC**'s.

CSC - Cathode Strip Chamber In the endcap in a pseudorapidity range of $2.0 < |\eta| < 2.7$, the **CSC** detectors provide a fast response and high spatial resolution, similar to **MDT**'s. Since **MDT** reach their maximum operational radiation tolerance close to the beampipe, **CSC** are used at the high radiation environment close to the beampipe. **CSC** detectors are multiwire

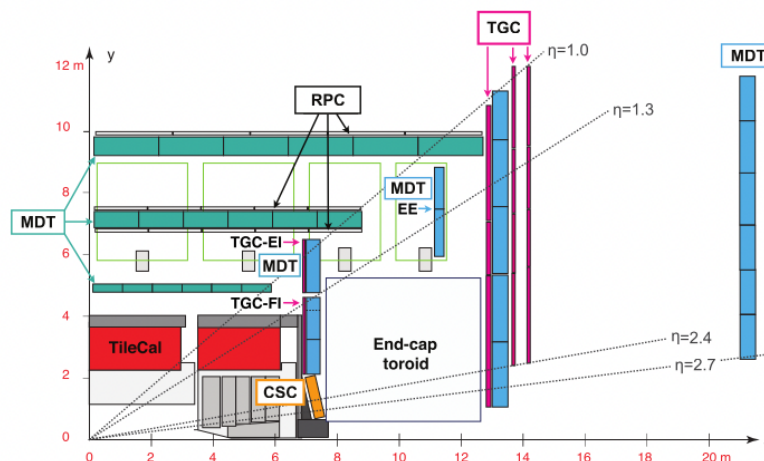


Figure 2.8: Overview of a quarter of the muon spectrometer, showing all subsystems [61].

proportional chambers filled with the same gas mixture as **MDT**'s. They provide both r and ϕ coordinates. Both **MDT** and **CSC** detectors are used for precision momentum measurements, whereas **RPC** and **TGC** detectors are used to provide fast information to the **ATLAS** trigger system (see section 2.2.5).

RPC - Resistive Plate Chambers In combination with **MDT**'s, **RPC** detectors are used to provide a coarse, quick, secondary coordinate measurement. Each **RPC** consists of two detector layers orthogonal to each other, providing ϕ and η coordinate measurements. The **RPC** covers an overall pseudorapidity region up to $|\eta| < 1.05$. The detectors are named after the two resistive parallel plates of phenolic-melaminic plastic laminate within each chamber, enclosing a gas mixture.

TGC - Thin Gap Chambers The last component of the **MS** are **TGC**. They are multi-wire proportional chambers similar to **CSC**'s, but with a coarser granularity. The gas filling is a mixture of CO_2 and n -pentane ($n\text{-C}_5\text{H}_{12}$). Similar to **RPC** detectors, **TGC** are able to provide a signal faster than 25 ns, allowing for a matchin of a signal to a specific bunch crossing. Their fast readout time is used in the trigger system, additional to **MDT**, s they provide a secondary measurement of the azimuthal angle.

2.2.5 The Trigger System

With all the components of the **ATLAS** detector described above, any interactions and electrical signals from the entire detector convolute into a large set of read-out information. Even without any proton-proton collisions provided by the **LHC**, **ATLAS** can detect feedback from the detectors through for example cosmic muons. Storing every single interaction within **ATLAS** during collisions would exceed the storage capabilities of the **CERN** computing centres and simultaneous would not provide any differentiation between high energetic collision interactions and low energy scattering of the protons. The **ATLAS** trigger system has been designed

to select collision events of interest to the multitude of physics analyses performed with ATLAS data. To do so, a two-stage trigger system was used during Run-2. A visualisation of the trigger system, as well as the flow of data through this system, is given in Figure 2.9.

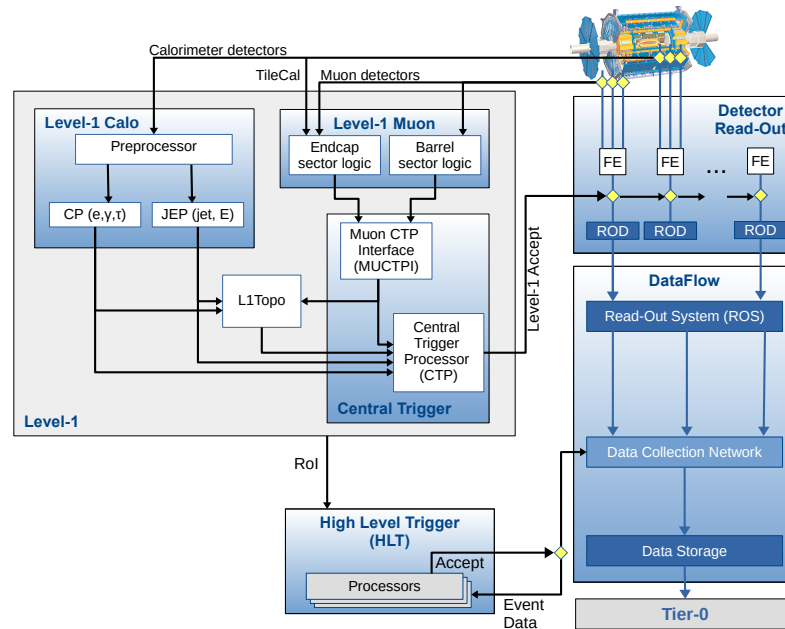


Figure 2.9: Overview of the ATLAS trigger system during Run-2. Adapted from [62].

The first trigger level is based in hardware. This *Level-1* trigger is built of processors digitizing the calorimeter readout and information from the muon spectrometers (TGC, RPC), identifying electrons, photons, tau leptons, jets, and can calculate missing transverse energy. The L1Topo component of the Level-1 system allows for topological requirements such as invariant mass selections and distance measures to be taken into account in the Level-1 decision. The final decision to keep or discard an event at Level-1 is made by the Central Trigger Processor (CTP). This Level-1 trigger step reduces the 40 MHz collision rate down to a maximum rate of 100 kHz [62] and passes on Regions-of-Interest in η and ϕ to the next trigger step, the High Level Trigger (HLT). Regions-of-Interest consist of neighbouring calorimeter cells in the ECAL and HCAL, a detailed discussion in connection with electron triggers is given in Chapter 4.

The HLT is a software-based trigger, a computing farm allowing for sequences of algorithms. The HLT is designed to reduce the event rate from 100 kHz to around 1 kHz that is saved. The algorithms run on the HLT farm have access to higher granularity calorimeter information as well as tracking information from the ID. A typical trigger sequence includes fast algorithms, designed to quickly reject events not targeted by the trigger, followed by more precise algorithms that can run more time-consuming reconstruction and identification similar to events stored offline. The exact sequence and type of algorithms considered at the HLT are defined in the trigger *menu*. This comprises a database of triggers, each trigger defining a sequence of algorithms and requirements on these algorithms for an event to pass the HLT. The overall set of triggers targeting various detector signatures associated with particles, such as electrons,

muons or photons as well as missing transverse energy. The trigger requirements are designed and budgeted in a way that the overall [HLT](#) rate does not exceed 1 kHz. In some cases, even the reduction in event rate achieved through the [HLT](#) algorithms for desired trigger requirements, such as low momentum triggers, is too high. To keep the overall [HLT](#) rate below 1 kHz in these cases, triggers can still be included in the menu, but with a *prescale*. A prescale is an artificial scaling of the trigger, only accepting every Nth trigger decision if the prescale factor is N. This allows triggers with an otherwise high rate to still collect events.

DATA ACQUISITION, RECONSTRUCTION AND MONTE CARLO SIMULATION

3

*“Champions keep playing until they
get it right.”*

Billie Jean King

A crucial step in the recording of collision events with ATLAS is the selection through dedicated signature triggers. These trigger decisions are emulated in Monte Carlo simulation in order to replicate the selection in data. After events have been selected by the ATLAS trigger system and saved to disk, further detailed reconstruction and identification algorithms can be performed. In the following, a short overview of the signature triggers of importance to this thesis as well as a summary of the reconstruction and identification processes for the particles and physics objects used in this thesis is given. Additionally, a brief description of Monte Carlo concepts and ATLAS detector simulation is given.

3.1 Signature triggers

An introduction to the ATLAS trigger system was given in section 2.2.5; in the following an overview of the trigger signatures of importance to this thesis are discussed. All the trigger signatures combined form a *trigger menu*, a selection of triggers simultaneously active in ATLAS in order to select all events of interest to the multitude of physics analyses in the ATLAS collaboration. A trigger is a unique identifier for a sequence of trigger algorithms and the requirements that have to be fulfilled after each algorithm step, including a specification of the Level-1 hardware trigger requirements. A signature here refers to the combination of specific interactions that different [SM](#) particles have with the various ATLAS detector layers.

3.1.1 Electron triggers

The electron trigger signature uses signals from the electromagnetic and hadronic calorimeters at Level-1 to select high energetic clusters of calorimeter towers. Based on that decision, a fast selection, followed by precision algorithm-based selections at HLT are performed. Very

detailed work on the electron trigger has been part of the PhD work of the candidate, therefore a detailed discussion of the electron trigger signature as well as its performance in Run-2 is discussed in chapter 4.

3.1.2 Muon triggers

The muon trigger signature relies on signals from the **MS** and tracks from the **ID**. In the Barrel of the detector, the Level-1 muon trigger signal consists of coincidences of hits in two or three **RPC** segments for high and low p_T momentum muons, respectively. In the End-Cap region ($1.04 < |\eta| < 2.4$), the Level-1 muon decision is based on coincidences in the **TGC** segments of the Big Muon Wheel. After this first Level-1 step, information on **ID** tracks is accessible at **HLT**. Multiple isolation requirements on the muons at trigger level can be applied. The lowest unprescaled single muon trigger uses a lower momentum threshold of 20 GeV in 2015, raised to 26 GeV from 2016 onwards. The efficiency of the lowest unprescaled single muon trigger between 2016 and 2018 is shown in Figure 3.1. An extensive description of the muon trigger and its performance in Run-2 can be found in [61], here only a short overview can be given. The efficiency of the trigger is calculated on recorded collision events with selections targeting events with Z-bosons decaying into a opposite-sign di-muon final state. A selection of muons from this decay, is used as unbiased *probe* sample to test the trigger's selection efficiency. The trigger efficiency is defined as a ratio of the selected probe muons fulfilling the trigger selections over all available probe muons. The trigger in Figure 3.1 shows a fast turn-on of its efficiency in dependency of the probe muon's momentum, reaching almost 70% efficiency in the barrel regions and 90% in the detector end-caps, with a close agreement between data and Monte Carlo simulation visible in the lower panels. The lower trigger efficiency observed in the barrel region compared

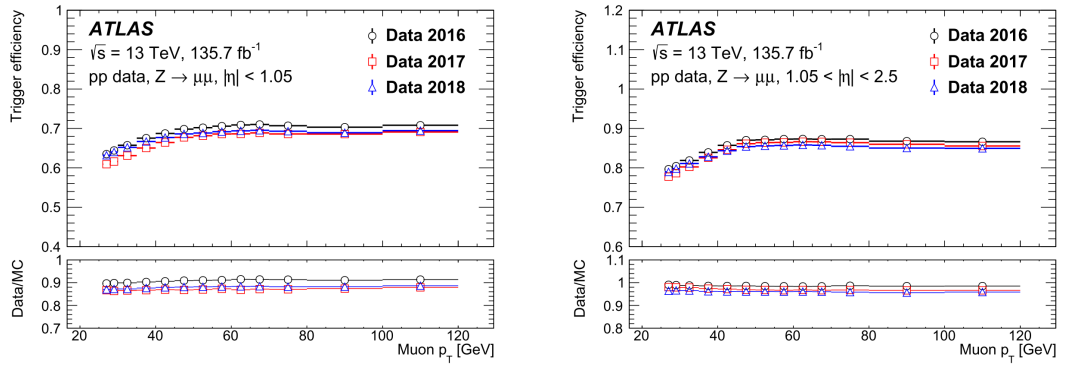


Figure 3.1: Efficiency of the lowest unprescaled muon trigger in data collected between 2016 and 2018 in the detector barrel ($|\eta| < 1.05$) and end-cap ($1.05 < |\eta| < 2.5$) regions, from [61]

to the end-cap is due to a smaller geometric coverage at the Level-1 trigger stage.

3.1.3 Missing transverse momentum triggers

Missing transverse energy (E_T^{miss}) in the detector is one of the essential features in many Beyond Standard Model (**BSM**) searches in ATLAS. In connection with R-parity conserving **SUSY**, the

lightest neutralino particle is stable and can escape the detector without being detected. This detector signature is similar to neutrinos escaping the detector. Triggering on missing transverse momentum in this thesis is used in combined triggers with taus. The E_T^{miss} trigger is solely based on calorimeter information; multiple algorithms are available on the High-Level-Trigger to calculate the missing transverse momentum, varying in the definition of used calorimeter clusters and their calibration. In essence, a projection and summation of the clusters as described in equation (3.1) [63] is performed.

$$\begin{aligned} E_x^{\text{miss}} &= - \sum_{i=1}^{|\text{Elements}|} E_i \sin \theta_i \cos \phi_i \\ E_y^{\text{miss}} &= - \sum_{i=1}^{|\text{Elements}|} E_i \sin \theta_i \sin \phi_i \end{aligned} \quad (3.1)$$

A detailed explanation of the E_T^{miss} trigger and its performance in Run-2 can be found in [63]. For data analysis and selection discussed in this thesis, only the most rudimentary missing transverse energy **HLT** algorithm is used. This is extracting E_T^{miss} from a sum of all calorimeter cells with their uncalibrated energy above a noise threshold. This noise threshold is included to avoid electronic noise and pile-up contributions.

3.1.4 Tau Triggers

The tau trigger signature is based on a fast selection of electromagnetic and hadronic clusters at Level-1, followed by reconstruction and identification algorithms run at the **HLT**. A detailed description can be found in [64]; a summary is given below.

The applied selections are based on hadronic tau decays happening before traversing the active detector region. These signatures are showing as narrow calorimeter energy deposits with a small number of associated tracks. At Level-1, a core region made of 2×2 trigger towers (each 0.1×0.1 in $\Delta\phi \times \Delta\eta$) is defined, with the E_T of the hadronic tau candidate made up of the two most energetic consecutive cells. Around this core region, an isolation region of 4×4 trigger towers is used to determine the isolation in the electromagnetic calorimeter.

The tau energy reconstruction at Level-1 does not include any calibrations or clustering algorithms and has a worse energy resolution than observed in the offline tau reconstruction. This leads to a signal efficiency loss for low transverse energy tau candidates. Regions-of-Interest selected by the Level-1 are passed to the HLT. The tau selection here includes three steps: a calorimeter only selection, a track preselection, and an offline-like selection. The calorimeter-only selection step uses the full detector granularity, making use of the topological clustering algorithm [65]. This algorithm, generating so-called *Topo-Clusters* considers the significance of the electronic signal of each calorimeter cell and removes calorimeter cells if they are not close to cells with a large signal. This topological clustering includes information about the shape and location of the cluster, allowing for calibrations to be applied. In the tau trigger case described here, a simplified tau energy calibration is applied. The track preselection step makes use of a two-stage fast-tracking reconstruction. At first, tracks within a narrow area along the beam axis are reconstructed, finding the tau vertex. In a second step, tracks in a larger

ΔR window are considered, but in a narrow interval around the tau vertex. This allows for fast reconstruction of the vertex and significantly reduces the CPU usage compared to a reconstruction of tracks in a large ΔR and z window. Eventually, an offline-like selection is applied. The tracks reconstructed in the previous step are now passed through precision tracking and therefore available with higher accuracy. Together with the calibrated clusters, multiple kinematic variables are used as input to a Boosted Decision Tree. This **BDT** is similar to an identification method previously used to identify offline taus. The **BDT** is trained to distinguish taus from jets, using features such as the maximum distance in ΔR of the tracks associated to the tau, with tracks associated with jets expected to be more wide-spread than tau associated tracks. A detailed description of the **BDT** can be found in [66]. Multiple tau identification working points are defined based on fixed cuts on the **BDT** output score. At trigger level, a medium working point is used.

3.2 Object Reconstruction

After the selection of events through the signature triggers described above, the particle signatures are reconstructed and identified *offline*, after they have been saved to storage. This reconstruction is done event by event with the same procedure applied to Monte Carlo simulation and recorded ATLAS data. Each particle has its reconstruction and identification procedure and can have additional algorithms to help with the specification of its properties. Since the event is already recorded, less limitations on the CPU consumption and timing constraints governing the online reconstruction can be used. In the following, a brief overview of the offline reconstruction and identification of the objects used in this thesis is given.

3.2.1 Electrons

The main features of an electron or positron (in the following both referred to as electron) in ATLAS is a cluster of energy deposits in the **ECAL**, tracks in the **ID** as well as a close match between the clusters and tracks in terms of $\eta \times \phi$. These three main features present the three consecutive steps in reconstructing electrons: first, a seed cluster is reconstructed: Based on a sliding-window algorithm, looking at collections of energy towers with at least 2.5 GeV of summed transverse energy. Here an energy tower is the sum of collected energy in all three layers of the **ECAL**, including the presampler, in a $\Delta\eta \times \Delta\phi = 0.025 \times 0.025$ segment. This mimics the granularity of the second layer of the **ECAL**. In Figure 3.2, the path of an electron through the different detector components is illustrated, also highlighting the three different layers in the **ECAL**.

After the seed cluster is identified, tracks are reconstructed. This is based on pattern recognition of hits in the **SCT** and Pixels, followed by an ambiguity resolution step, resolving ambiguity of hits associated with multiple tracks, and an extension of the tracks to the **TRT**. For the fitting of tracks, a global χ^2 fitting procedure is used, with either a pion hypothesis or an electron hypothesis in the presence of significant Bremsstrahlung. Consecutively, a Gaussian Sum Fil-

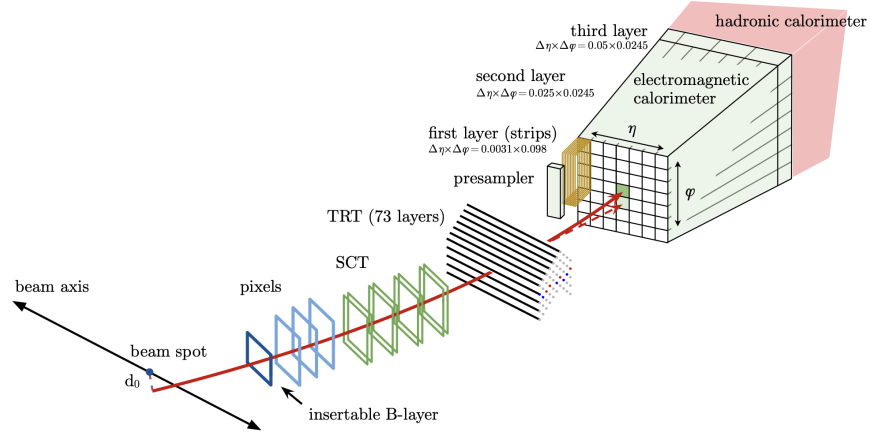


Figure 3.2: Illustration of an electron path through the Inner Detector and Calorimeters of ATLAS, highlighting the layer granularity in the electromagnetic calorimeter. The dashed line presents a photon produced through interactions of the electron with the ID material. Taken from [67].

ter (GSF) [68] is applied to account for energy losses in the ID material. As the last electron reconstruction step, a matching of the GSF-track and calorimeter cluster is performed. This matching is based on a geometric distance between the clusters and tracks and is described in detail in [67]. The electromagnetic energy clusters are further calibrated as described in [69].

After the reconstruction, a further identification is necessary to distinguish prompt electrons from electrons originating from misidentified hadrons, non-isolated electrons from heavy-flavour decays or electrons from photon conversion.

This identification is based on a likelihood discriminant construction. The likelihood discriminant d'_L is given in equation(3.2) [67], where a fixed factor $\tau = 15$ is used to achieve a smooth discriminant distribution.

$$d_L = \frac{L_S}{L_S + L_B} \quad (3.2)$$

$$d'_L = -\tau^{-1} \ln(d_L^{-1} - 1)$$

Here L_S describes the likelihood function of signal, prompt electrons. Whereas L_B is the likelihood of non-prompt, fake electrons. The likelihoods L_S and L_B are a product of probability density functions for a large set of kinematic variables. The distributions and the likelihoods are binned in the p_T and η of the electron candidate. A complete set of the variables considered in the likelihood definition is included in [67], as well as a detailed description of the pdf and likelihood extraction. Using a multi-variate technique can help where a simple cut on single variables would not offer strong discriminating power. Based on the output of the discriminant, several working points are defined. These are designed to have a given signal-electron selection efficiency in each (p_T, η) bin. Therefore a cut on the discriminant is defined in each (p_T, η) bin. In addition, to stabilise the performance at high pileup (to avoid getting too much increase in background passing the selection), the cut on the discriminant is done such that it depends linearly on a pileup variable. Effectively, the cut gets tightened as pileup

increases. The number of primary vertices in the event is used as the pileup variable for offline electrons. For online electrons, this is too computationally intense, so the number of inelastic collisions per bunch crossing (μ) is used instead as a measure of the amount of pileup. Additional to the electron likelihood based identification, isolation requirements can be applied to distinguish between prompt electrons and electrons from heavy-flavour decays. Two isolation criteria for offline electrons are defined, *FCTight* and *FCLoose*. These isolation working points include a restriction on the transverse energy sum in a $\Delta R < 0.2$ region around the electron in the calorimeter (E_T^{iso}) to be below 0.06 and 0.2 times the electrons energy (E_T), for *FCTight* and *FCLoose*, respectively. The calorimeter based isolation requirement is combined with a track-based isolation, restricting the momentum. The radial distance has a maximum value of 0.2 and decreases with the electrons momentum. For the *FCTight* working point, the momentum fraction within the isolation cone is restricted to be smaller than 0.06 times the electrons momentum, for *FCLoose* it is below 15% of the electrons momentum.

3.2.2 Muons

Muon candidates as minimum ionising particles in ATLAS are reconstructed using track segments from the Muon Spectrometer that have been matched to **ID** tracks. Energy loss in the calorimeters is taken into account in a combined fitting of **MS** and **ID** tracks. Multiple identification working points in varying levels of prompt muon selection efficiency and background rejection are defined, designed to satisfy the large varying needs of physics analyses. Additional to identification criteria, an isolation requirement can be applied [70]. Similar to the electron isolation working points, a muon isolation based on calorimeter and track-based isolation criteria is defined, *FCLoose*. The transverse energy in a $\Delta R < 0.2$ isolation cone around the muon is restricted to 30% of the muons momentum. Additionally, the momentum in a variable size, maximum $\Delta R < 0.3$ cone around the muon should not extend 15% of its momentum.

3.2.3 Jets

The particle-flow jet reconstruction [71] makes use of calibrated Topoclusters as well as tracking information from the **ID**. The topological clustering algorithm has been previously introduced and discussed in section 3.1.4 in relation to tau triggers. The anti- k_T sequential recombination algorithm [72] is used to form jet objects based on particle-flow objects. To remove pile-up jets, a multivariate discriminant based on vertex information, the Jet vertex Tagger (**JVT**) [73] can be used.

3.2.4 Taus

As briefly highlighted within the description of the tau trigger in section 3.1.4, hadronic tau decays have a distinct detector signature that can be used to trigger on events containing hadronic taus. In the following, a brief discussion of the tau decay is given to provide a baseline of

the features important to this thesis, before summarizing the hadronic tau reconstruction and identification within **ATLAS**. Tau leptons have a mass of 1776.86 MeV and a mean lifetime of 290.3×10^{-15} s [32]. With their proper decay length around $87 \mu\text{m}$ [32], taus decay before interacting with active detector layers of **ATLAS**. As can be seen in Figure 3.3a, tau leptons decay via a W boson and a tau neutrino. The hadronic or leptonic decay of the tau is determined through the consecutive decay of the W -boson, Figure 3.3a, highlighting a leptonic decay into an electron. Leptonic decays of the tau make up 35% of tau decays, with hadronic decays making up 65% [32]. Examples of hadronic tau decays are given in Figure 3.3b, highlighting the calorimeter systems in which the decay products will leave the majority of their energy. Not explicitly shown in the sketch is the W -boson, only its decay products. In 72% the hadronic tau decay includes one charged pion, in 22% of the cases the decay includes three charged pions. These charged pions leave tracks in the **ID**, presenting a distinct identification feature of taus, the number of charged tracks or *prongs* associated with their decay. The hadronic decay of a tau lepton is determined through the quarks and intermediate mesons built in the W -boson decay. Examples thereof are shown in Figure 3.3b.

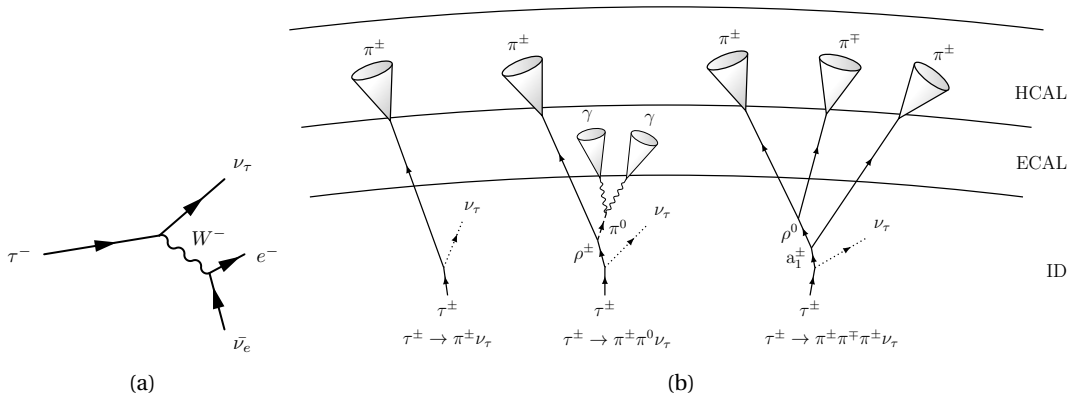


Figure 3.3: Feynman diagram of a leptonic tau decay, highlighting its decay via a W -boson (a). Examples of hadronic tau decays into (from left to right) one charged pion, one charged and one neutral pion as well as three charged pion (b) [74], highlighting in which detector systems the participating particles will be detected.

Hadronic tau candidates are seeded from jets that have been reconstructed using the anti- k_T algorithm, with a distance parameter of $\Delta R = 0.4$ [75]. Additionally, jet seeds are required to have $p_T > 10$ GeV and $|\eta| < 2.5$. A **BDT** is used to categorize all tracks associated to the tau candidate within $\Delta R = 0.4$ of the tau axis to be core or isolation tracks. The number of core tracks is used to define the prongness of taus, indicating the number of charged particles involved in the tau's decay.

To distinguish tau particles from jets, a recurrent neural network (RNN) identification is used. For this, multiple kinematic variables are used for the training of an RNN [76]. Variables include specifications of the cluster depth, the longitudinal extension and the radial cluster extension as well as fractions of momenta in the core or isolation region of the tau cluster, to highlight a few of them. The performance of the RNN identifier is shown in Fig. 3.4 for its 1-prong and 3-prong decay modes. This is also compared with the performance of a **BDT** identifier previously used in the τ identification in **ATLAS**. The improved network architecture of the RNN identifier

provides rejection of jets by up to a factor of two better than the previous BDT approach.

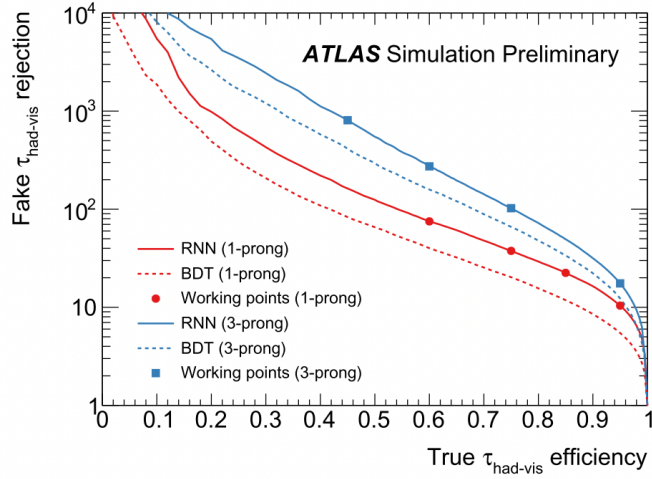


Figure 3.4: Performance of the tau **RNN** identification working points in comparison with previously used **BDT** based identification [76]

3.2.5 Missing transverse energy

The reconstruction of missing transverse energy after an event has been stored by a trigger is similar to the procedure at trigger level described in section 3.1. In contrast to the trigger reconstruction, the offline missing transverse energy reconstruction is not based on uncalibrated clusters, but fully calibrated physics objects. Additionally to this part of the E_T^{miss} reconstruction considering physics object, a soft term comprised of low momentum tracks is taken into account [77].

3.3 Monte Carlo Simulation

To evaluate any measurements taken with the ATLAS detector, simulations of physics processes and their decay within the ATLAS detector are necessary. This is achieved through the use of Monte Carlo event generators. In the following, a brief description of the essentials of Monte Carlo simulations are given, based on pedagogic introductions given in [78]. Followed by a short overview of the Monte Carlo generators used in this thesis. For the production of a final state X through the collision of two hadrons (h_1, h_2), the inclusive cross section can be factorised like the following:

$$\sigma_{h_1, h_2 \rightarrow X} = \sum_{a, b \in q, g} \int dx_a \int dx_b f_a^{h_1}(x_a, \mu_F^2) f_b^{h_2}(x_b, \mu_F^2) \int d\Phi_{ab \rightarrow X} \frac{d\hat{\sigma}_{ab}(\Phi_{ab \rightarrow X}, \mu_F^2)}{d\Phi_{ab \rightarrow X}} \quad (3.3)$$

With $f_a^{h_1}(x_a, \mu_F^2) f_b^{h_2}(x_b, \mu_F^2)$ representing the parton distribution functions. Here μ_F presents the factorisation scale. This scale is the cutoff between processes that are considered perturbatively and the non-perturbative regime. An important part of this inclusive cross section is

presented by the Matrix element describing the hard scattering process, this is included in the last integral of equation (3.3). After the inclusive matrix element calculation as described in equation (3.3), the parton showering takes into account the additional particles that can contribute to the production. The parton showering here is considering that a parton can originate from a splitting of other partons. To not consider the additional particles twice, a matching of the matrix element and the parton showering has to be performed. The produced partons in such a showering will form colourless hadrons, which in turn can further decay. A last aspect to be taken into consideration for event simulations is the underlying event. This is caused by *spectator* partons, not directly participating in the hard scattering.

3.3.1 Monte Carlo generators

Sherpa One of the general purpose event generators used in this thesis is SHERPA [79]. It includes matrix element generators as well as a built-in parton showering. In this thesis, simulated events with SHERPA include Multi-boson processes as well as the associate production of vector bosons and jets.

Powheg The POWHEG [80] framework is a matrix element generator at next-to-leading perturbative order. The matrix element generation is interfaced with generators like PYTHIA or HERWIG++ in order to simulate the parton shower. This kind of combination of matrix element generator and parton shower simulation is used for top-related processes such as top-antitop pair production.

MadGraph5_aMC@NLO MadGraph5 [81] is used as a matrix element calculator at next-to-leading perturbative order. Similar to POWHEG, it is interfaced with PYTHIA or HERWIG to include parton showering.

Pythia A second general purpose event generator used in this thesis is PYTHIA 8 [82], even with matrix element calculation and parton showering possible within PYTHIA, it is widely used for its parton showering, interfaced with POWHEG or HERWIG. Additionally, PYTHIA is used in this thesis to simulate minimum-bias proton-proton collisions.

Herwig The HERWIG [83, 84] Monte Carlo event generator has capabilities to be used to simulate the matrix element, but is only used within this thesis as a variation of the PYTHIA parton showering.

EvtGen EvtGen [85] is a framework that simulates the decay of bottom and charm hadrons. Events associated with the production and decay of a top quark used in this thesis are simulated through a combination of POWHEG, PYTHIA and EvtGen. Within this thesis, all events generated with a parton showering by PYTHIA include final state particle decays simulated with EvtGen.

3.3.2 ATLAS detector simulation

To directly compare the data collected with the ATLAS detector with the prediction of SM and BSM events in simulation, the interaction of the produced particles with the detector material has to be simulated. The Geant4 [86] software package is used to simulate the interaction of particles with the detector material. A full Geant4 model of the ATLAS detector is used to simulate the transition of particles produced in proton-proton collisions through the different detector layers.

The simulation of a large number of interactions necessary to mimick the ATLAS reconstruction is computationally extensive. Especially the simulation of shower developments in the calorimeters consumes a large amount of CPU and computing time. For many BSM searches, a large number of parameters affecting the predicted particle masses and interactions have to be simulated. A 'fast' parameterised detector simulation has been developed to cope with this high simulation demand. A so-called Atlfast-II or AFII setup simulation chain uses Geant4 simulation for the interactions in the ID and muon spectrometer, but a parametrised simulation called FastCaloSim for the particle interactions in the electromagnetic and hadronic calorimeter. The improvements in computing time compared to Geant4 simulation of the full detector as well as a fast, simplified Geant4 simulation is shown in Figure 3.5. The overall processing time is reduced by roughly an order of magnitude compared to the full Geant4 simulation [87]. The fast calorimeter simulation FastCaloSim uses a parametrisation of the calori-

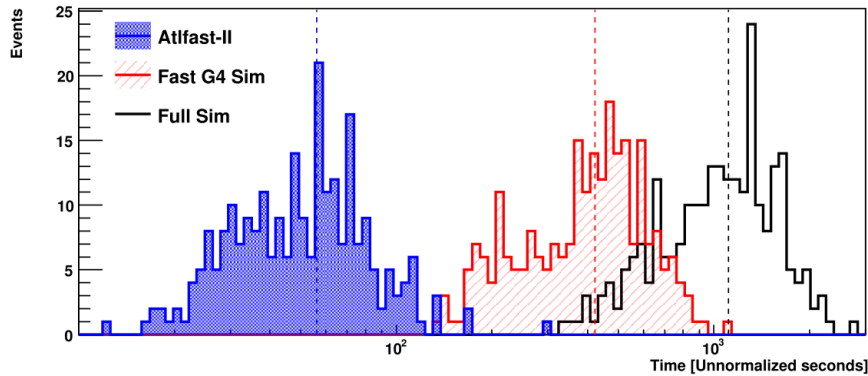


Figure 3.5: CPU time distributions for 250 $t\bar{t}$ events compared for G4, fast G4 and AFII setup, taken from [87]

meter response. The parametrisation has been extracted through Geant4 simulation and tuned to data. The main three simplifications include simplifying the detector geometry, approximating the calorimeter cells as cuboids, only reproducing the average lateral energy distributions and restricting the simulation to three types of initial particles.

THE ATLAS ELECTRON TRIGGER PERFORMANCE IN RUN-2

4

My mission in life is not merely to survive but to thrive and to do so with some passion, some compassion, some humor, and some style.

Maya Angelou

The following chapter gives an introduction to the electron trigger in ATLAS and describes the performance of selected electron triggers during Run-2. This work is part of the author's involvement in the ATLAS electron and photon trigger signature group between 2018-2022. The main focus of this work is the measurement of trigger efficiencies as well as the calculation of trigger scale factors, which have been widely used in physics analyses of the Run-2 dataset. This work has contributed in a major way to the first electron and photon trigger performance publication in ATLAS [88] and has been presented by the author at the ICNFP2019 conference [89, 90].

In section 4.1, an introduction to the electron trigger signature is given, followed by a discussion and motivation of the electron trigger menu in section 4.2. A brief explanation of the efficiency and scale factor calculation methodology is given in section 4.3. The trigger performance throughout Run-2 including full Geant4 detector simulation (section 4.4) as well as parametrised AF2 simulation (section 4.5) is then completed by a short discussion on the perspectives and limitations of these studies in section 4.6.

4.1 The ATLAS electron trigger

Triggers selecting electron signatures are widely used in ATLAS. They target a detector signature of tracks in the **ID**, combined with energy deposits in the **ECAL**. As described in section 2.2.5, the first selection step for any signature is the Level-1 trigger. For electrons, this consists of clusters in the electromagnetic calorimeter. The Level-1 trigger identifies a Region of Interest (**RoI**), a group of neighbouring trigger towers. A trigger tower presents a sum of calor-

imeter cells in a $\Delta\eta \times \Delta\phi$ region in the detector, including the various layers in the **ECAL** and **HCAL**. As can be seen in the visualisation given in Figure 4.1, this Region-of-Interest is the local maximum of transverse energy deposited in the calorimeter cells. A specified energy threshold is passed at Level-1 if any of the 2x1 or 1x2 connected trigger towers in the **RoI** exceed the specified threshold. The trigger towers have a granularity of $\Delta\eta \times \Delta\phi = 0.1 \times 0.1$ [91]. The energy of the clusters has undergone an electromagnetic energy scale calibration. This calibration reconstructs the energy deposited through an electromagnetic shower, but is not able to correctly account for energy losses in hadronic shower developments. An energy threshold variable in η around a nominal E_T threshold can be applied, accounting for geometrical dependencies in the energy cluster calibrations. Illustrated through a bright yellow ring in Figure 4.1, a requirement on the isolation of the core can be made. This sets a limit on the sum of transverse energy contained in the 12 trigger towers surrounding the Region-of-Interest, in comparison to the energy contained in the core. Lastly, a limit on the hadronic leakage can be required. This limit restricts the energy contained in the hadronic calorimeter trigger towers behind the central 2x2 clusters in the electromagnetic calorimeter. Any requirements on the hadronic leakage or isolation are only applied to transverse energies reconstructed at Level-1 below 50 GeV [88].

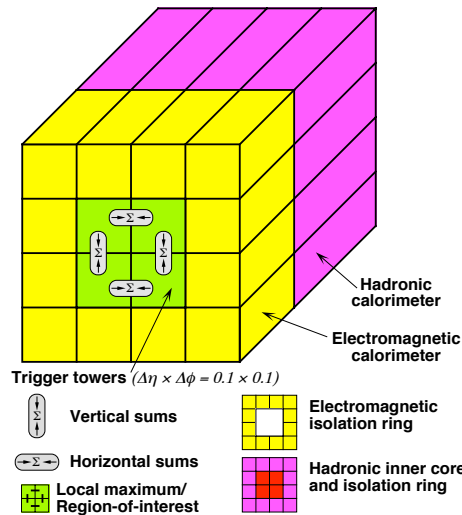


Figure 4.1: Visualisation of the Level-1 electron selection [91].

The selections required from the Level-1 trigger form the basis to all **HLT** triggers. They can be summarized through the following nomenclature:

$L1_{\{\text{multiplicity}\}}EM\{E_T\text{threshold}\}\{\text{possible additional requirements: V H I}\}$,
 with V allowing the E_T threshold to vary up to $^{+3}_{-2}$ GeV from the nominal value dependent on η , H vetoing a hadronic energy deposit behind the **ECAL** cluster and I imposing an electromagnetic isolation. As an example, a L12EM10VH Level-1 trigger requires two electromagnetic clusters with at least 10 GeV transverse energy, without significant energy leakage into the hadronic calorimeter and allows for the energy threshold to vary in η . No isolation of the clusters in the **ECAL** is required. As has been previously discussed in section 2.2.5 and is illustrated in Figure 2.9, once an event is accepted by the Level-1 system, a Region-of-Interest is passed on to the **HLT**.

A visualisation of the consecutive [HLT](#) algorithms in use for non-isolated electron triggers over a 15 GeV transverse energy threshold can be seen in Figure 4.2. For all electron triggers, the first set of algorithms focus on a fast reconstruction. The main goal of these selection steps is the fast rejection of events that do not include electrons in order to reduce the input for the following time-consuming precision algorithms, especially those employing tracking information. From

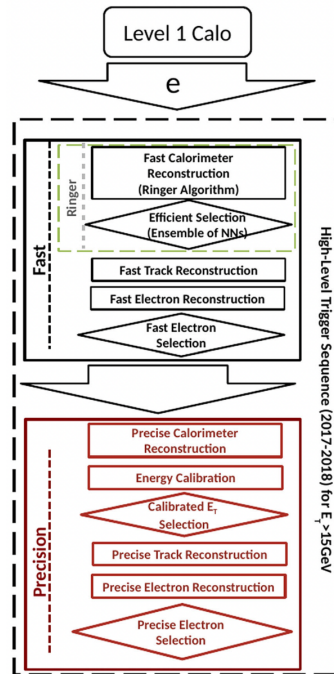


Figure 4.2: Visualisation of the consecutive algorithms of the electron trigger signature at the [HLT](#) for non-isolated electron trigger. Adapted from [88].

2017 onwards, the first step in the electron trigger at [HLT](#) is the so-called *Ringer* algorithm. The Ringer algorithm replaced a cut-based fast calorimeter reconstruction step, which is discussed in detail in Ref. [88]. The neural network based Ringer algorithm was developed for electrons above a 15 GeV energy threshold due to the low available statistics of Z to ee events below that threshold. The overall idea behind this neural network is to use the lateral development of electromagnetic showers in the form of a cone to construct concentric rings in the calorimeter layers around the most energetic calorimeter cell. A vector of all energy sums of these concentric rings, normalised to the energy contained in the RoI, are used as input for a neural network. More details on the design of the neural network can be found in [88]. Following either the Ringer algorithm or cut-based fast calorimeter algorithm, a fast track reconstruction is performed in the RoI and the electron candidates are required to have a track matching the calorimeter clusters in order to proceed to the precision steps. All precision steps are similar to the offline reconstruction steps described in section 3.2.1, a special focus on the differences with respect to offline reconstructions is given in the following. The precision calorimeter reconstruction has access to calorimeter cells extending the RoI and constructs calorimeter clusters following a sliding window algorithm. The cluster is then calibrated, following an offline like calibration described in [92]. The energy threshold for electron trigger at [HLT](#) is applied based on this calibrated energy clusters. As last steps, a precise track reconstruction and electron re-

construction, matching the precision tracks with the electromagnetic clusters is completed by the precise electron selection. This selection uses a likelihood electron identification similar to the offline electron identification described in section 3.2.1. The most notable differences compared to the likelihood constructed offline are the following: no refitting of tracks (with **GSF**) is used to account for Bremsstrahlung effects on trigger level. Fixed-size Topo-clusters are used instead of dynamic, variable sized Topo-clusters [67]. Due to computational limitations at trigger level, the average number of interactions per bunch-crossing, $\langle \mu \rangle$, is used as a measure of pile-up instead of the number of primary vertices. Additional to the algorithms visualised in Figure 4.2, a track-based isolation criteria can be required. The typical electron trigger nomenclature used to clarify the requirements of a trigger can be visualised like the following:

`HLT_{multiplicity}_e{ E_T threshold}_{identification}_{optional isolation}`

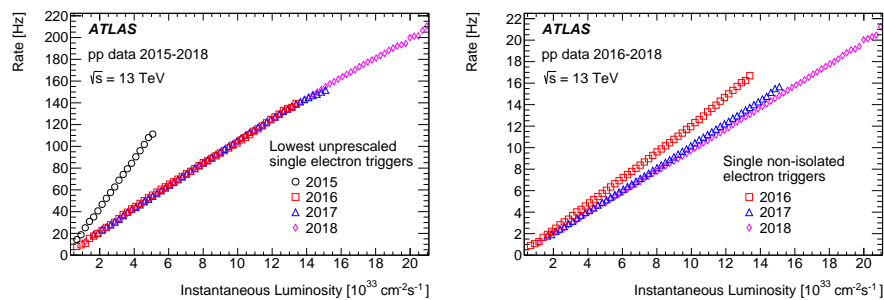
At trigger level, there are three different levels of identification, based on the likelihood discriminant: `lhvloose`, `lhloose`, `lhmedium` and `lhtight`. An additional specification of `nod0` highlights a version of the likelihood identification without a restriction on the transverse impact parameter, d_0 . The transverse impact parameter describes the minimum transverse distance of a track to the beam axis, the longitudinal impact parameter measures the distance from that intersection to the primary vertex along the beam axis. The electron likelihood definition at the **HLT** without d_0 has previously been introduced due to observed mismodellings of the impact parameter within the trigger reconstruction. Only one isolation variant is available for electrons at trigger level, `ivarloose`, requiring a track-only isolation, limiting the momentum contribution in a variable sized cone in ΔR around the electron candidate's track. Some special triggers fall outside this naming convention and typical flow of consecutive algorithms, such as `HLT_e200_etcut`, a 200 GeV energy threshold electron trigger, but without using any likelihood based identification.

4.2 Electron trigger menu in Run-2

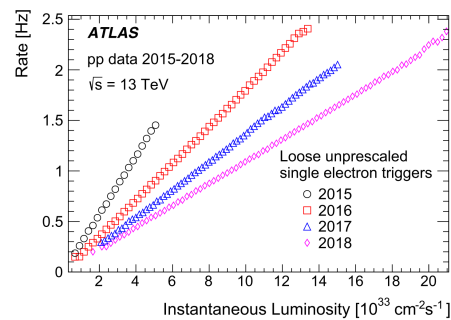
Even with the nomenclature of electron triggers highlighted and discussed in the previous section, this does not specify the version of trigger algorithms used at **HLT** or which triggers are active during data-taking or whether or not they are prescaled. This is all defined in the *trigger menu*. The trigger menu defines all triggers active for different trigger signatures throughout the years. The trigger menu includes single object triggers, such as single electron triggers, as well as multiple-object triggers (e.g. di-electron trigger) and combined object triggers (e.g. electron-muon trigger). Different trigger are categorized into primary trigger, important for crucial physics analyses, and supporting trigger, used mainly for monitoring purposes. Different maximum **HLT** rates are allocated to the triggers accordingly. Additionally, every trigger signature is allocated a maximum overall 'budget' of **HLT** rate in order to allow for a multitude of signatures.

The two primary electron triggers are single electron as well as di-electron triggers. To allow these triggers to stay unprescaled and therefore collect as much data as possible, their energy

threshold, as well as isolation and identification criteria, have to be adapted throughout the years of data taking. In Table 4.1, the evolution of these primary triggers in the trigger menu throughout the Run-2 data-taking can be seen. The single electron trigger as used in physics analysis is a combination of the single electron triggers listed in Table 4.1 for the respective year. The trigger rate is a leading factor in adapting trigger energy and algorithm thresholds throughout data taking. This has been monitored in Run-2 and is shown in Figure 4.3. Here Figure 4.3a shows the trigger rate evolution of the lowest unprescaled single electron trigger. The steep rate increase with instantaneous luminosity in 2015 clearly shows that the increased energy threshold in the consecutive years was needed to reduce the trigger rates and keep them below roughly 200 Hz. This restriction is due to the overall possible trigger rate of 1 kHz and the need to budget this rate across all trigger signatures. In general, the linear increase of the trigger rate with the instantaneous luminosity is expected, since the instantaneous luminosity is a measure of the amount of collisions in *ATLAS*, providing a larger amount of collision events the trigger can select.



(a) Lowest unprescaled energy threshold single electron triggers (b) Single non-isolated electron triggers



(c) Loose unprescaled single electron triggers

Figure 4.3: Single electron trigger rates during Run-2 [88]. The three graphs show the the three lower energy triggers with electron likelihood selection making up the single electron trigger as discussed in Table 4.1. Omitted here are the high energy triggers without likelihood selection. In (a) the lowest energy threshold trigger with a 24 GeV and 26 GeV energy threshold in 2015 and 2016-2018, respectively can be seen. In (b) the rate of the 60 GeV threshold trigger without isolation requirement in use from 2016-2018 is shown. Figure (c) shows the trigger rate for the loose likelihood trigger with 120 (140) GeV energy threshold in 2015 (2016-2018).

In addition to an increased energy threshold, in 2016 an isolation requirement (*ivarloose*) was included in the lowest unprescaled trigger. At higher energy thresholds, the trigger rate drops sufficiently to allow for less stringent identification and isolation requirements on the trigger

Trigger type	2015	2016	2017-2018
single electron	e24_lhmedium (EM20VH)	e26_lhtight_nod0_ivarloose (EM22VHI)	
	e120_lhloose e200_etcut	e60_lhmedium_nod0 e140_lhloose_nod0 e300_etcut	
dielectron	2e12_lhloose (2EM10VH)	2e17_lhvloose_nod0 (2EM15VH)	2e17_lhvloose_nod0 (2EM15VHI) 2e24_lhvloose_nod0 (2EM20VH)

Table 4.1: Evolution of the primary electron trigger during Run-2. given in brackets are the Level-1 seeds used for the given [HLT](#) trigger.

electron. Therefore the e60_lhmedium_nod0 trigger was included in the single electron trigger combination from 2016 onwards, as shown in [4.3b](#). At even higher electron E_T , a loose likelihood selection is possible. In 2015, this threshold was above 120 GeV, in 2016-2018 raised to 140 GeV. The trigger rates of these loose triggers are given in [Figure 4.3c](#).

Di-electron trigger allow for a further reduction in energy threshold and loose identification criteria due to the increased electron multiplicity. The di-electron trigger chains in Run-2 can be seen in [Table 4.1](#).

In 2017 and 2018, not only one but two primary di-electron trigger were defined. This was motivated by the used Level-1 seed, selecting two electromagnetic energy clusters. The *2EM15VH* seed used in 2016 showed a high Level-1 acceptance rate. (see [Figure 4.4](#)).

To mitigate this and reduce the rate of the associated [HLT](#) di-electron trigger, an isolated Level-1 ([L1](#)) trigger (*L12EM15VHI*) was used instead from 2017 onwards, allowing for the threshold to be kept at the same level. A second di-electron trigger without isolation at Level-1 is used additionally.

Compared to a non-isolated Level-1 trigger with otherwise same selections, the rate is reduced by around a factor of four. Even increasing the energy threshold by 5 GeV achieves less reduction in rate (see [Figure 4.4](#)).

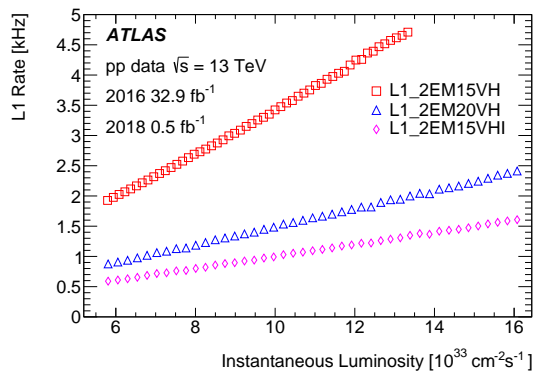


Figure 4.4: Level-1 rate for isolated (*L1_2EM15VHI*) and non-isolated triggers (*L1_2EM15VH*, *L1_2EM20VH*) [[88](#)].

4.3 Efficiency measurements and scale factor calculation

When using electrons in a physics analysis, the overall efficiency for electrons in ATLAS has to be considered. This total efficiency can be factorised into four terms referring to different steps to select and identify an object as electron, as shown in equation (4.1) [93].

$$\epsilon_{\text{total}} = \epsilon_{\text{reconstruction}} \times \epsilon_{\text{identification}} \times \epsilon_{\text{isolation}} \times \epsilon_{\text{trigger}} \quad (4.1)$$

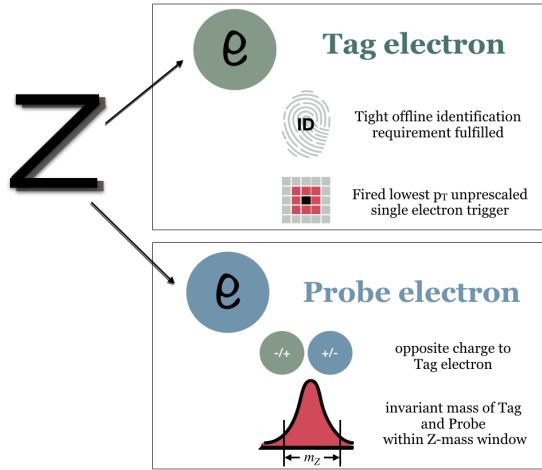
The trigger efficiency is evaluated with respect to *offline* electrons, electrons that have been reconstructed and identified based on precision algorithms used after the event has been selected and stored by a trigger. This allows analyses to correct the trigger efficiency according to the choice in identification and isolation algorithms used on stored data.

4.3.1 The Z tag-and-probe method

To evaluate the trigger efficiency, an unbiased sample of electrons is needed. The Z boson's decay into two oppositely charged electrons can be used to achieve this with the so-called *Z tag-and-probe* method. Events are selected if one of the electrons fulfills the requirements of the lowest unrescaled single electron trigger (*fires* the single-electron trigger). If this electron was produced through a Z-boson decay, a second electron of opposite charge is expected to be in the event. Since the event has already been selected by the single-electron trigger, the second electron does not need to be selected by any other triggers and is therefore unbiased in terms of trigger decisions. The first electron selecting the event is referred to as *tag* electron, the second electron is referred to as *probe* electron. To ensure a low contribution of non-prompt electrons as tag electrons, the tag electron is required to pass a more stringent identification working point than the probe electron. To select a probe candidate, electrons of opposite charge to the tag electron are considered, with the invariant mass of the tag and probe pair required to be within a window around the Z boson mass m_Z .

An illustration of the Z tag-and-probe method with an exemplary tag electron configuration is given in Figure 4.5.

The selection of probe electrons through the Z tag-and-probe method allows for an unbiased selection of electrons to measure trigger efficiencies. When selecting events based on the Z tag-and-probe method additional non-Z-boson originated processes can enter the selections. This can happen when two electrons not from a Z-boson decay fall within the invariant mass window consistent with a Z boson. Since this background is combinatorial, it does not reproduce a similar Z-boson mass peak, but generate a flat component in the di-electron invariant mass distribution. This flat component of the invariant mass distribution is estimated to follow a polynomial distribution. Due to its combinatorial nature, these events populate a same-sign di-electron final state in a similar manner than a opposite sign di-electron final state. Therefore, a replication of the Z tag-and-probe electron selection is repeated, but with the two electrons being of same electric charge. The contributions to this same-sign selection are used to

Figure 4.5: Illustration of the Z tag-and-probe method.

normalise the polynomial distribution. Once normalised, the number of probe electrons predicted through this *background template* is subtracted from the opposite-sign Z tag-and-probe selection. In all events selected, the probe electrons transverse energy, pseudorapidity as well as the average number of pileup interactions contributing to the event is noted. To evaluate the efficiency of an electron trigger in question, whether or not a probe electron would pass the selection of [HLT](#) trigger algorithm requirements is checked. The number of all probe electrons fulfilling the trigger requirements after background subtraction ($N_{probe}^{triggered}$) is compared to the overall set of probe electrons after background subtraction N_{probe} . This ratio as described in equation 4.2 yields a trigger efficiency measurement with reference to an eligible set of electron candidates, for one specific choice of tag and probe electrons.

$$\epsilon_{trigger} = \frac{N_{probe}^{triggered}}{N_{probe}} \quad (4.2)$$

Since the trigger efficiencies are calculated for electrons fulfilling offline reconstruction and identification requirements, such as offline identification working points, the contribution of backgrounds to the trigger efficiency is negligible in all cases discussed in this thesis. Indeed, in most of the efficiency distributions presented in the following, the background subtraction step has been omitted, since it has shown to be smaller than per-mill level efficiency differences and within uncertainties.

4.3.2 Trigger efficiency evaluation and scale factor calculation

The Z tag-and-probe method described above allows for the calculation of trigger efficiencies for one specific set of method parameters. The parameters that define the calculated trigger efficiency include: the tag electron definition, including its identification working point and optional isolation requirement., as well as the di-electron invariant mass window used to define the phase space region consistent with a Z -boson decay. Lastly, the template used to subtract non Z -boson backgrounds. Even though the trigger efficiency is also varying with the definition

of the probe electron, this is not considered as a parameter of the method, since the interest lies in providing trigger efficiencies with respect to a specific offline electron definition, therefore the offline electron definition is reflected in the probe electron definition.

In order to consider the uncertainty due to a specific choice of parameters, the Z tag-and-probe method is repeated for variations of the parameter configurations. The variations are the following:

- The tag electron offline working point: *Tight* identification working point as well as *Tight* and *Medium* likelihood identification with additional isolation are used
- The invariant mass window around m_Z : $[[80, 100], [75, 105], [70, 110]]$ GeV
- The background subtraction template - two varying templates are considered

The nominal trigger efficiency for a specific probe electron definition is determined as the average of the trigger efficiency calculation from all combinations of all of these method parameters. The systematic uncertainty in the averaged result is obtained from the root-mean-square (RMS) of the individual results [67]. The statistical uncertainty of the trigger efficiency calculated is the average statistical uncertainty observed in all variations.

Correction factors for Monte Carlo simulation, also called trigger efficiency scale factors, are calculated from the above described efficiencies. These correction factors are needed to scale the trigger efficiency performance as simulated in Monte Carlo simulation to its actual performance as observed in data. It is calculated as the ratio of the trigger efficiency in data (ϵ_{data}) over the efficiency in simulation (ϵ_{MC}):

$$SF = \frac{\epsilon_{\text{data}}}{\epsilon_{\text{MC}}} \quad (4.3)$$

The Monte Carlo simulation used to extract ϵ_{MC} is a $Z \rightarrow ee$ set of events simulated with POWHEG interfaced to PYTHIA8 and EvtGen. The $Z \rightarrow ee$ process is overlaid with soft QCD processes simulated by PYTHIA8 and re-weighted to mimic the pileup conditions in data. This extracted scale factor presents a reweighting factor that can be applied to Monte Carlo simulation on an event-by-event basis to correct the simulated trigger efficiency to its actual efficiency observed in data.

4.4 Run 2 performance studies on fully simulated events

The trigger efficiencies of a large set of electron triggers have been studied. The following discussion is focused on the single electron and di-electron trigger performance throughout Run-2. A more extensive discussion on the overall electron trigger performance in Run-2 can be found in [88].

4.4.1 Single electron trigger

Next to trigger rates, the efficiencies of the single electron trigger chain play an important role in understanding their performance, both a-priori during data taking as well as long term performances such as presented in the following. Figure 4.6 compares the trigger efficiency in data, dependent on E_T (4.6a), η (4.6b) as well as $\langle \mu \rangle$ (4.6c) of the considered offline electron. The overall structure of the single electron trigger combination, consisting of all triggers

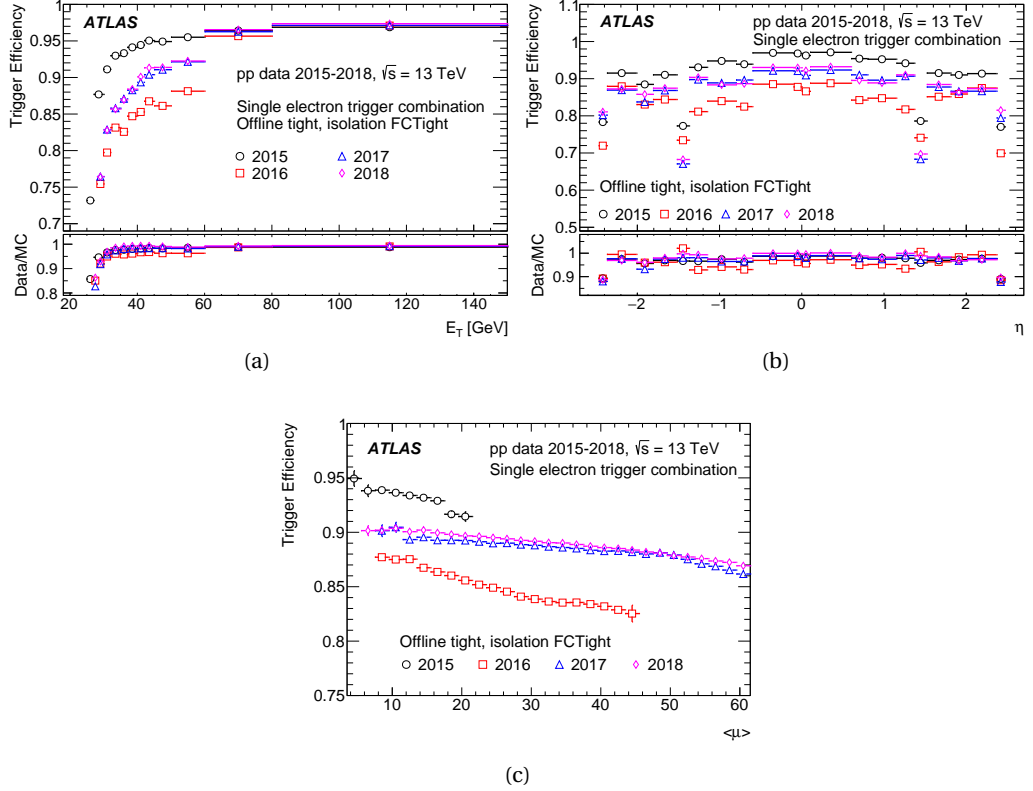


Figure 4.6: Single electron trigger performance in Run-2. Shown is the trigger efficiency with respect to the offline electron's transverse energy (a), pseudorapidity (b) and the pileup in the event. Bins with low statistics have been removed.

in Table 4.1 is strikingly visible in Figure 4.6a. Around an electron energy of 60 GeV, a jump in efficiency can be observed. This is the point when the looser, *lmedium*, trigger electron identification with higher energy threshold has reached its efficiency plateau and becomes more efficient than the lower energy *ltight* the single electron trigger. This is clearly visible in the 2016-2018 triggers including a *medium* identification trigger chain, as listed in table 4.1. An overall loss in efficiency can be seen from 2015 to 2016. The shift in the turn-on of the efficiency in the E_T distribution is due to the increased energy threshold from 2016 onwards. Even though the trigger and its nomenclature described in Table 4.1 have not changed from 2016 to 2017 or 2018, the efficiency can be seen to decrease in 2016, compared to 2017 and 2018 (visible throughout Figures 4.6a, 4.6b and 4.6c. This is due to changes to the underlying HLT algorithms of the single electron trigger. In 2016 some inefficiencies were observed with respect to offline electron identifications, this was recovered through a simpler selection within the precision electron selection in 2017-2018 data taking. Additionally, the trigger algorithms

were tuned to the performance observed in 2016 and improved. This is causing the increased efficiency observed in the last two years of Run-2.

As well as on data, it is crucial to study the trigger performances in Monte Carlo simulation. In Figure 4.7, the efficiency of the single electron trigger in data is compared between data and simulation. Even though the detector architecture and material density are very well modelled in Monte Carlo simulation, operational effects such as inactive detector modules can not be reflected in the simulation. This can lead to an overestimation of the trigger efficiency in simulation, as can be seen in the E_T (4.7a) as well as η (4.7b) distributions. Within the detector crack-region ($1.37 < |\eta| < 1.52$), the efficiency of electron triggers is significantly lower than in other η regions. This is due to a high amount of inactive material such as detector support structures. Many analyses will not consider electrons reconstructed within this region. Similarly to this, towards high η , an increase of inactive material is leading to a reduced trigger efficiency in data.

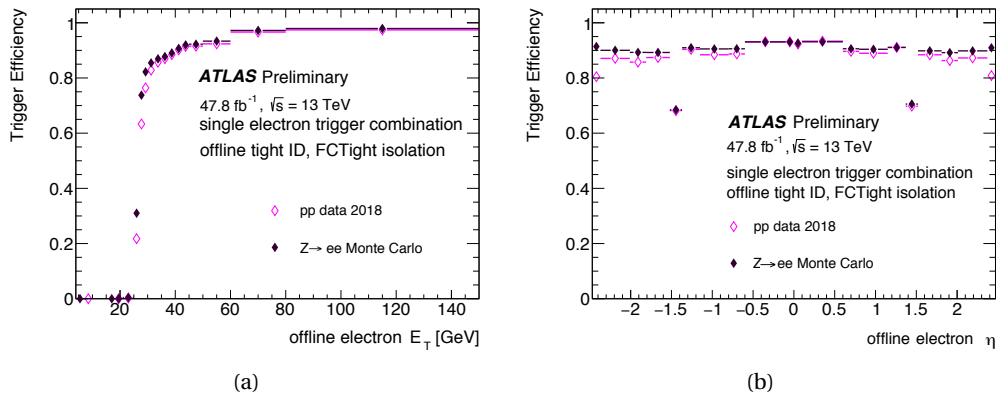


Figure 4.7: Single electron trigger efficiency in 2018 in dependency of the offline electron E_T and η .

As described previously in the calculation methods of trigger efficiencies and scale factors, the observed differences between efficiency modelling in simulation to its actual performance in data are accounted for through scale factors. These scale factors are calculated dependent on E_T and η with scale factor maps in dependency of E_T and η provided to physics analyses. An example visualisation of such a scale factor map can be seen in Figure 4.8. The largest differences are visible in the crack region as well as in the turn-on of the trigger, when the trigger efficiency has not yet reached a plateau.

4.4.2 Di-electron trigger

Because they allow for looser E_T selections than single electron triggers, di-electron triggers are heavily used in multileptonic physics analyses. As discussed in section 4.2, in 2017 and 2018 two di-electron chains have been used: A first one uses a Level-1 seed requiring the electromagnetic energy cluster in the ECAL to be isolated; another one is defined without the isolation requirement. The efficiency shown in Figure 4.9 represents the trigger efficiency of one part of the dielectron trigger, the $E_{12_LHLOOSE}$ for the overall $2E_{12_LHLOOSE}$ dielectron

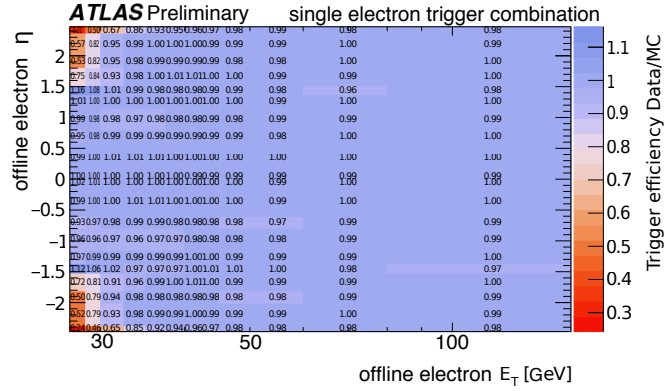


Figure 4.8: Single electron trigger combination scale factor in dependency of E_T and η of the offline electron.

trigger used in 2015. The total efficiency of the di-electron trigger is calculated at analysis level taking into account combinatorics of all electrons in the analysis events, based on the provided efficiency. A loss in efficiency in the E_T distribution (4.9a) for the di-electron triggers using a L1 isolation can be seen. This only affects the E_T range below 50 GeV, since the Level-1 isolation is only active below that energy threshold. Also within the μ dependency of the efficiency (4.9c), a loss in efficiency through the isolation requirement can be seen. To mitigate this efficiency loss, most physics analyses use a combination of isolated and non-isolated di-electron trigger.

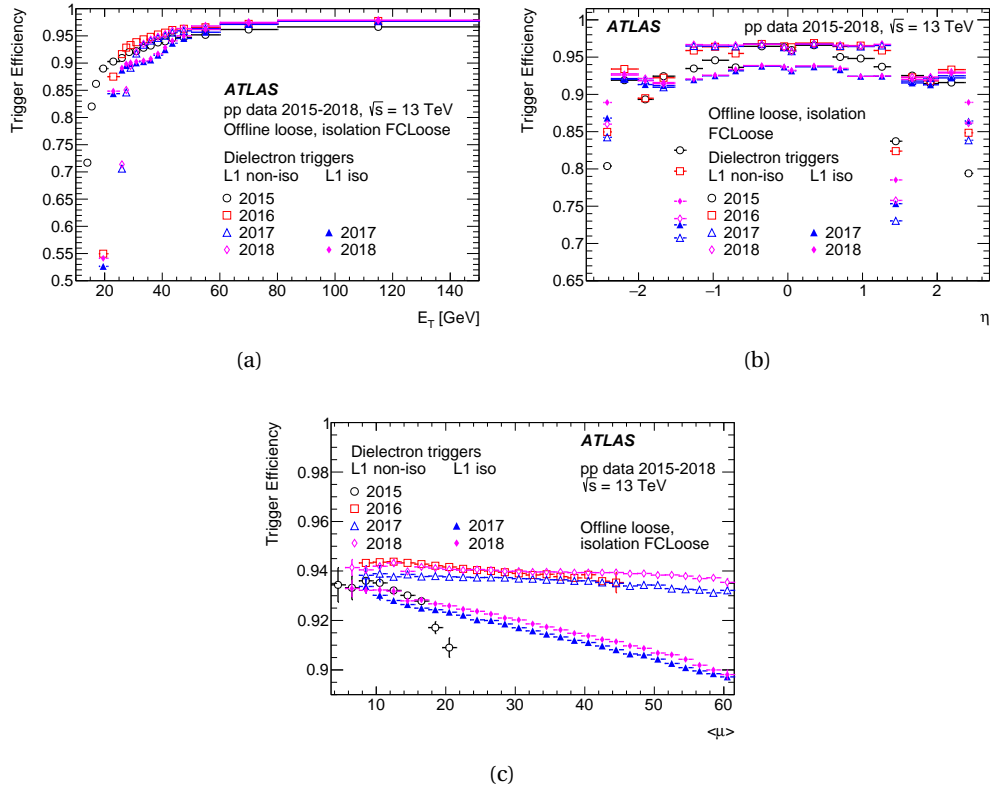


Figure 4.9: Di-electron trigger efficiency in Run-2. Shown is the trigger efficiency with respect to the offline electron's transverse energy (a), pseudorapidity (b) and the pileup in the event. Bins with low statistics have been removed [88].

4.5 Full Run 2 AF2 fast simulation studies

In physics analyses, Monte Carlo samples in use are generated with a full detector simulation of ATLAS, but also with a simplified parametrised approach of the calorimeter simulation. A detailed discussion can be seen in section 3.3.2. This simplified approach is widely used for the generation of large parameters spaces of BSM samples, but also variations in the modelling of SM processes. To ease the following discussion, Monte Carlo samples using Geant4 detector simulation for all detector components are here referred to as *full* simulation, whereas simulations using the AFII setup as introduced in section 3.3.2 are referred to as *fast* simulation. In many cases, analyses assume the validity of full-simulation trigger scale factors also in fast simulation. This has last been studied during Run-1 (see [87]), but has since not been revisited. To validate or correct this assumption, the behaviour of the lowest unprescaled single electron trigger has been studied in fast simulation samples and compared to its equivalent performance in full Geant4 detector simulation.

4.5.1 Single electron trigger

In the first year of Run-2 data taking, the lowest possible energy threshold of the single electron trigger is at 24 GeV, including a *medium* likelihood identification working point. The 2015 single electron trigger efficiency in dependency of the electron energy, pseudo-rapidity as well as pileup is shown in Figure 4.10.

Considering the trigger performance as a function of pileup or energy, integrated over η , a close agreement of full simulation and fast simulation is observed in Figures 4.10a and 4.10c. The pseudorapidity displayed in Figure 4.10b shows up to 5% differences in trigger efficiency in the crack region of the detector, compared to full simulation, with full simulation closer emulating the trigger efficiency in data. The closest agreement between full simulation and fast simulation can be seen in the central detector region, where the accuracy of the FastCaloSim calorimeter layout assumptions are closest to the actual detector layout. This is visible in the central pseudorapidity region of $|\eta| \leq 1.5$ in Figure 4.10b. Towards higher pseudorapidity ($|\eta| > 2$), the accuracy of the fast simulation is falling behind the full simulation. Even though the parametrised simulation can reproduce the full simulation's pileup dependency, both simulations are not mimicking the falling trigger efficiency with a higher number of simultaneous collisions observed in 2015 (Fig. 4.10c).

As discussed in section 4.2 various requirements defining the single electron trigger had to be tightened in 2016. The effects on this can also be seen in the behaviour in fast simulation shown throughout Figures 4.11a to 4.11c.

Generally, it should be noted that the tightening of the online working point used in the lowest unprescaled trigger is compared with an offline tight electron, so effects that are partially hidden through a tighter offline compared to an online working point in 2015 can show up in the 2016 and onward performance more distinctively. Which can be observed comparing Figure 4.10 and Figure 4.11. As is the case for 2015, the differences between fast and full simulation

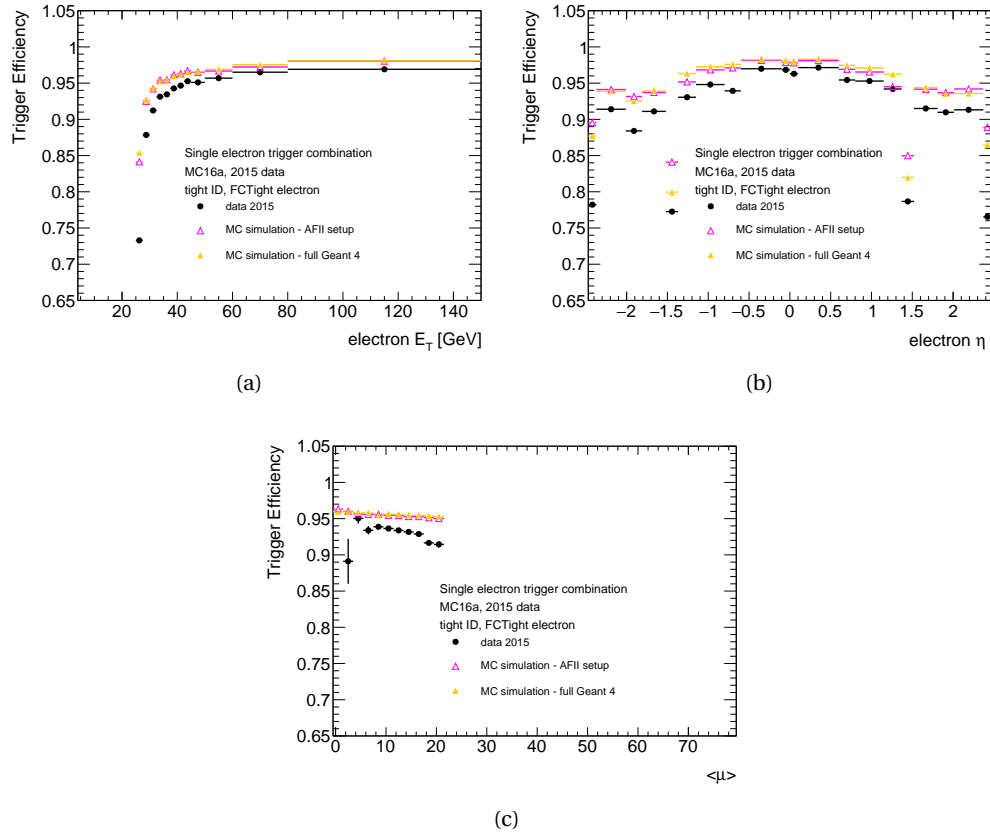


Figure 4.10: 2015 single electron trigger efficiency E_T comparison of full simulation and fast simulation samples. Shown is the trigger efficiency with respect to the offline electron's transverse energy (a), pseudorapidity (b) and the pileup in the event.

are most pronounced in the pseudorapidity distribution. In the bulk of the distribution before the crack region, the parametrised simulation is closer to the performance in data, whereas, towards higher $|\eta|$, this behaviour is inverting to differences between parametrised and full simulation up to 3%. The fast simulation is more accurately representing the pileup dependency in data than the full simulation (Fig. 4.11c), even improving to higher pileup values. Within the turn-on of the trigger efficiency concerning the electron energy (Fig. 4.11a), the efficiency is similarly closer to data in AF2 than in full simulation, whereas in the trigger efficiency plateau reached above 50 GeV the differences decrease.

In the two later years of Run-2 an increased instantaneous luminosity led to collision events with a higher number of pileup (as discussed in Section 2.1 and Fig 2.3). This can be seen in the larger pileup range in 2017 as well as 2018 in Figures 4.12c and 4.13c respectively.

Even though the parametrised calorimeter simulation can closely replicate the trigger efficiency for lower pileup conditions around $\langle \mu \rangle \leq 40$ (even closer than the behaviour in full detector simulation). The predicted efficiency drops to lower values than observed in data. This can be seen in Figures 4.12c and 4.13c. In both years, the fast simulation is underestimating the trigger efficiency in the bulk of the detector ($|\eta| < 1.5$, whereas full simulation is overestimating the efficiency (Figures 4.12b and 4.13b). This behaviour is also observable throughout the trigger turn-on in Figures 4.12a and 4.13a.

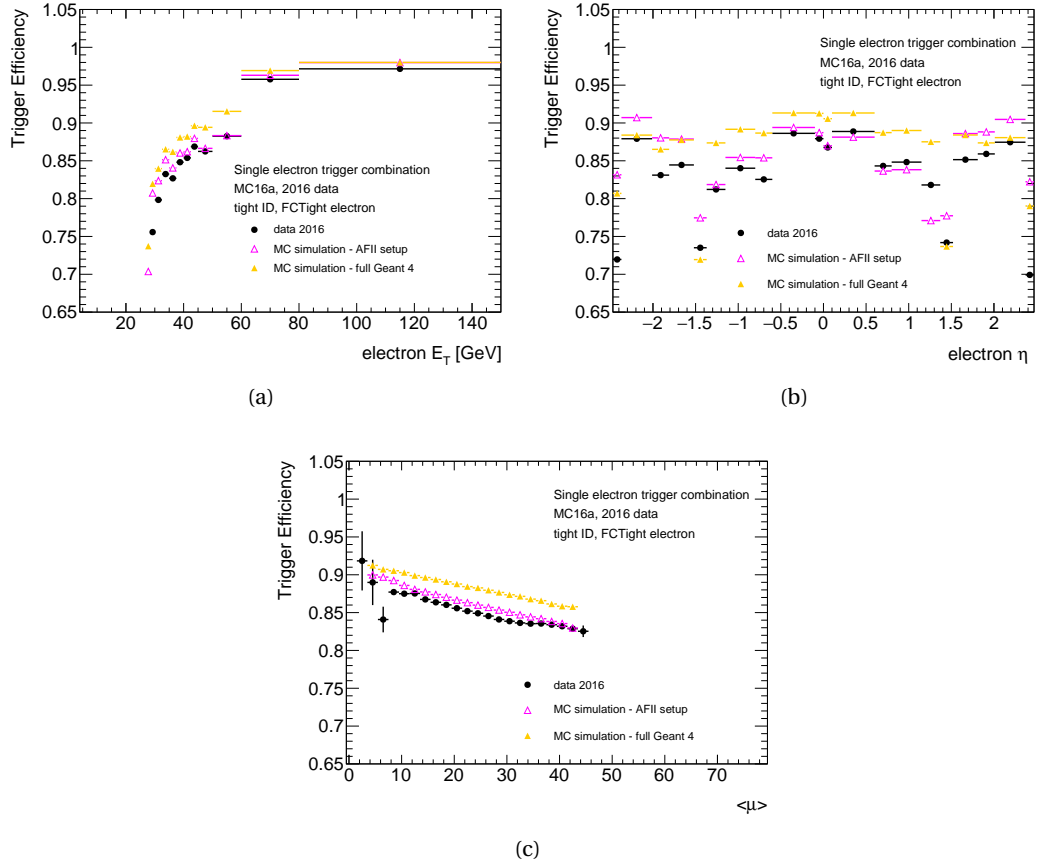


Figure 4.11: 2016 single electron trigger efficiency comparison of full simulation and fast simulation samples. Shown is the trigger efficiency with respect to the offline electron's transverse energy (a), pseudorapidity (b) and the pileup in the event.

The differences observed in the trigger efficiency are a culmination of multiple effects and can not be pointed towards one factor. Differences in performance of the online identification in full and fast simulation can be caused through varying modelling of e.g. the shower shape variables used in the identification likelihood (as described in section 3.2.1), only to name one.

The main objective of the described studies was to determine where an assumption of the full simulation trigger behaviour is accurate also in fast simulation samples and to provide correction factors for AF2 samples. An exemplary comparison of correction factors extracted from full simulation as well as AF2 samples can be seen in Figure 4.14. After the trigger has reached its efficiency plateau, the scale factors are largely within 1% difference to 1. The most significant differences are visible within the trigger turn on, below 60 GeV. Even though the scale factors are close to each other in AF2 and full simulation, they are not consistent within their uncertainties, given that the total scale factor errors are in the per-mill regime.

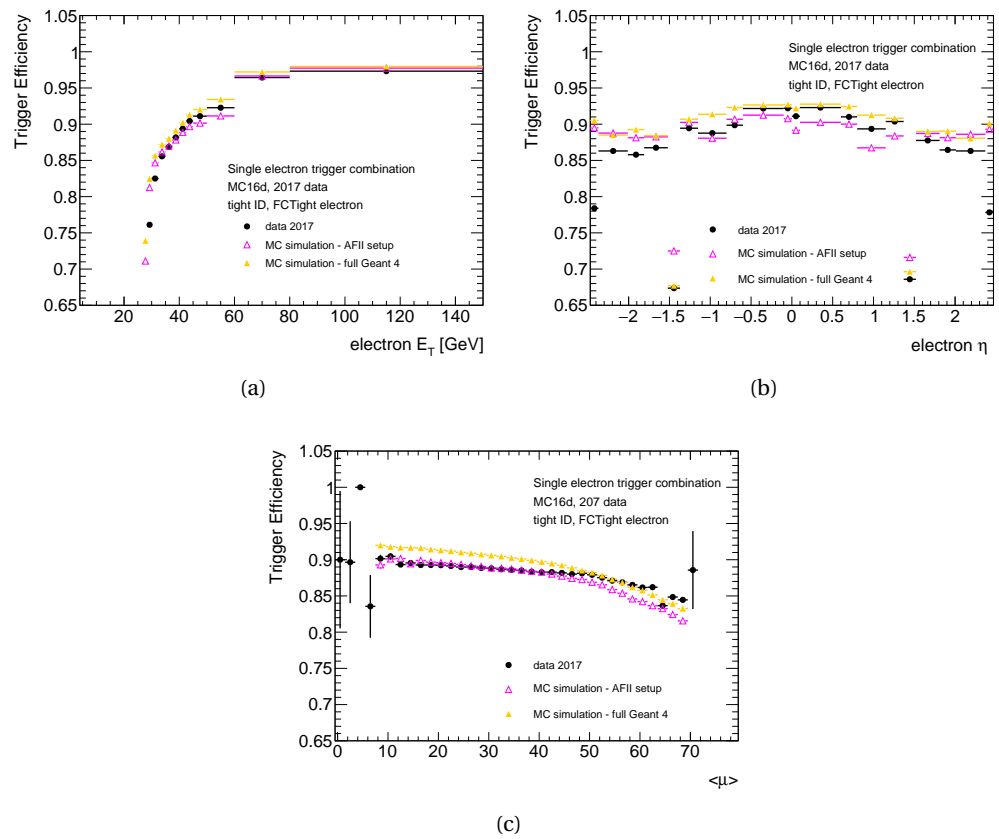


Figure 4.12: 2017 single electron trigger efficiency comparison of full simulation and fast simulation samples. Shown is the trigger efficiency with respect to the offline electron's transverse energy (a), pseudorapidity (b) and the pileup in the event.

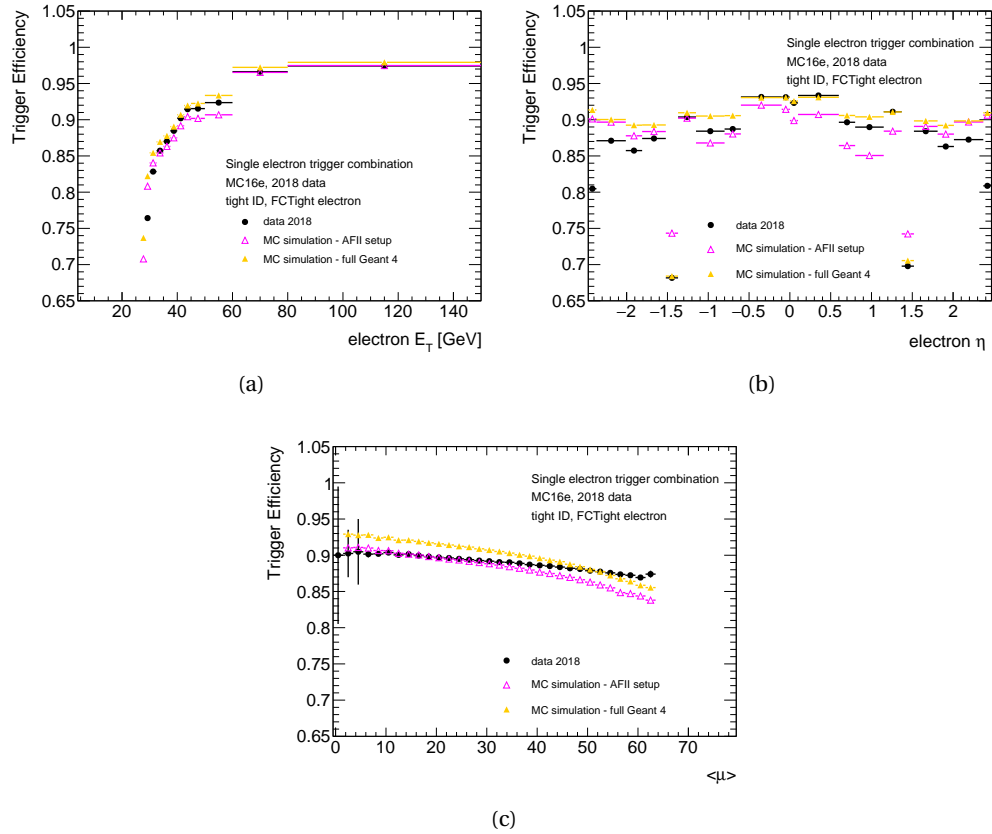
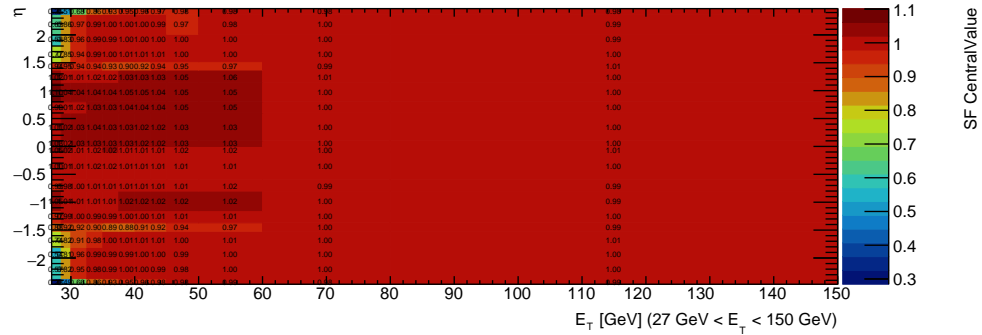
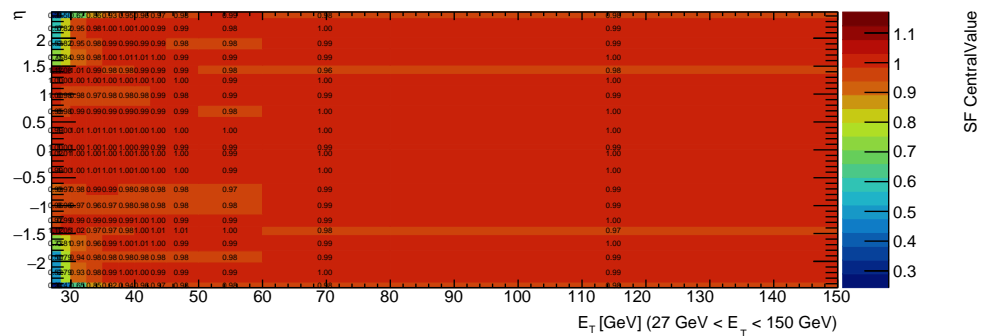


Figure 4.13: 2018 single electron trigger efficiency comparison for full and fast simulation. samples. Shown is the trigger efficiency with respect to the offline electron’s transverse energy (a), pseudorapidity (b) and the pileup in the event.



(a) Fast Simulation scale factor



(b) Full Simulation scale factor

Figure 4.14: Scale Factor maps in dependency of η and E_T for fast simulation (a) as well as full simulation (b).

4.6 Summary and future perspectives of this work

The studies presented in this chapter comparing fast and full simulation have shown the need for specific trigger scale factors for samples simulated with the AF2 procedure. Many precision measurements in ATLAS have since moved to using these scale factors provided to the ATLAS community. Currently, there are large efforts under way further improving the AF2 fast simulation using machine learning algorithms and further tunings to data [94]. Given the convolution of factors contributing to the efficiency of a trigger in data as well as simulation, next to ongoing efforts on a move to the improved parametrised detector simulation, no in-depth studies were performed to reach a complete understanding of all visible effects of the AF2 trigger performance. Following the studies above, rather similar studies of the trigger efficiency on these improved parametrised detector simulation have been encouraged for Run-3.

SEARCH FOR SUSY IN A FINAL STATE WITH AT LEAST TWO HADRONICALLY DECAYING TAU LEPTONS

5

*"Let us choose for ourselves our path
in life, and let us try to strew that
path with flowers."*

Emilie du Chatelet

This chapter is describing a search for supersymmetric particles in a final state with at least two hadronically decaying tau leptons. This search has been the author's main project and has been the author's sole responsibility. This work has been published as [ATLAS](#) conference note [\[95\]](#) and was presented at ICHEP2022 through a poster contribution by the author [\[96\]](#). An introduction to the theoretical model of interest to this search, together with a short motivation of the model is given in section [5.1](#). In section [5.2](#), an overview of other experimental searches for this model is given. The strategy of the analysis discussed here is given in section [5.3](#), with an overview of the considered samples ([5.4](#)) and the selection process employed in this search ([5.5](#)). Definitions of the analysis objects are given in section [5.6](#), followed by the signal region optimisation ([5.8](#)) and background estimation ([5.9](#)). An overview of the considered uncertainties is given in section [5.10](#). Before discussing the final results and interpretation in section [5.12](#) and [5.13](#), the statistical concepts relevant for this analysis ([5.11](#)) are summarised. The described search has then been combined with a search for the same model in a different final state. This search has not been performed by the author but the statistical combination has been; therefore a brief overview of this orthogonal search is given in section [5.14](#), before illustrating the gain of the statistical combination of the analyses in section [5.15](#).

5.1 Introduction and theoretical motivation

Supersymmetry is a promising extension of the [SM](#), with a multitude of possible production mechanism of supersymmetric particles at the [LHC](#). In hadron-hadron collisions, the production of particles through strong interactions is the dominant mechanism. As can be seen in [Figure 5.1](#), the strong production of supersymmetric particles has a larger cross section than an electroweak production through gauginos or sleptons. However, if strongly produced particles

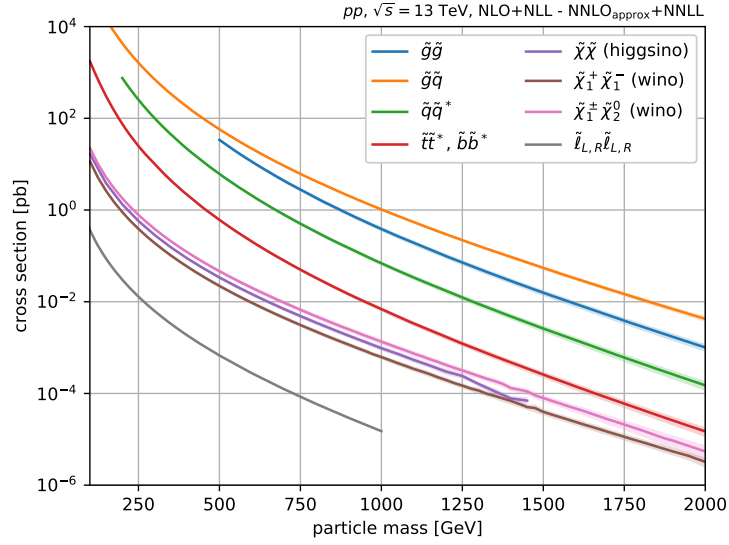


Figure 5.1: Cross section comparison in 13 TeV proton-proton collisions [97, 98].

(gluinos and squarks) are heavy, electroweak production cross sections can become the leading production mode of **SUSY** particles at the **LHC**. Given the latest status of strong and third generation squark searches as discussed in section 1.4, gluinos and squark masses are expected to be larger than 1 TeV in most cases. This is motivating the investigation of electroweak production modes of **SUSY** as presented within this thesis.

This electroweak production of **SUSY** particles includes the production of charginos and neutralinos. Assuming R-Parity conservation (see equation (1.15)), **SUSY** particles are pair-produced and the lightest **SUSY** particle is stable. A stable lightest supersymmetric particle can be a candidate for Dark Matter. In the search for **SUSY** particles described here, a simplified model (Figure 5.2) is considered in order to optimise search regions and interpret the results. The lightest Chargino ($\tilde{\chi}_1^\pm$) is produced together with the next-to-lightest neutralino ($\tilde{\chi}_2^0$). This can happen through a multitude of proton-proton interactions, which is visualised through the larger gray shaded area.

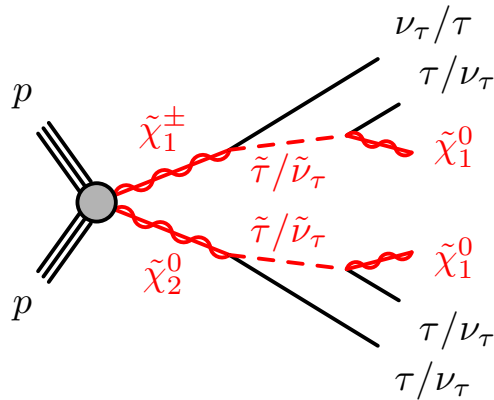


Figure 5.2: Feynman diagram of the simplified supersymmetric model considered in this thesis [95].

In this simplified **SUSY** model, the $\tilde{\chi}_2^0$ and $\tilde{\chi}_1^\pm$ are assumed to be mass degenerate and Wino

dominated. The $\tilde{\chi}_1^\pm, \tilde{\chi}_2^0$ consecutively decay via a $\tilde{\tau}$ or $\tilde{\nu}$ into the lightest, bino-like neutralino ($\tilde{\chi}_1^0$). In many parameter configurations of **SUSY**, third generation sleptons can be the lightest sleptons [6], motivating the $\tilde{\chi}_1^\pm \tilde{\chi}_2^0$ decay via $\tilde{\tau}$ or $\tilde{\nu}$. The $\tilde{\chi}_1^0$ is assumed to be the lightest supersymmetric particle and therefore stable under R-parity conservation and a **DM** candidate. The $\tilde{\tau}$ and $\tilde{\nu}$ masses are fixed through a parameter x as described in equation (5.1) (adapted from [99]). In the investigation of the model considered here, this parameter is fixed to 0.5. As discussed in section 1.3, the gauge and mass eigenstates of the $\tilde{\tau}$'s can differ. In this simplified model, $\tilde{\tau}_L$ and $\tilde{\tau}_R$ are assumed to be mass-degenerate.

$$m_{\tilde{\tau}/\tilde{\nu}_\tau} = m_{\tilde{\chi}_1^0} + x * \Delta m(\tilde{\chi}_2^0 - \tilde{\chi}_1^0) \quad (5.1)$$

In this simplified model, the $\tilde{\chi}_1^\pm$ decays via a $\tilde{\tau}$ and ν_τ or $\tilde{\nu}$ and τ further into either a τ or ν_τ and a $\tilde{\chi}_1^0$. In both cases, one neutrino, one tau and one **LSP** are the final state of this leg of the simplified model. The $\tilde{\chi}_2^0$ decays via a $\tilde{\tau}$ or $\tilde{\nu}$ into a pair of two τ leptons or τ neutrinos. In order to achieve a final state with at least two hadronically decaying tau leptons, the $\tilde{\chi}_2^0$ has to decay via a $\tilde{\tau}$.

Supersymmetric models with light sleptons, such as the $\tilde{\tau}$ considered in the discussed model, can offer a Dark Matter candidate that can be compatible with the observed relic Dark Matter density, thanks to possible co-annihilation of neutralinos via these light sleptons [100]. Since lepton flavour universality is not a fixed symmetry in the **SM** and **SUSY**, considering all lepton flavours in searches for new physics is crucial.

5.2 Previous model investigations

The above described simplified model has been previously investigated with the **ATLAS** detector during Run-1 [101, 102] and most recently using partial Run-2 data [99]. Within the partial Run-2 data analysis, a search for the $\tilde{\chi}_1^\pm \tilde{\chi}_2^0$ production described above, as well as a simplified model of $\tilde{\chi}_1^\pm$ pair production decaying via staus, was considered. In the analysis, a final state with at least two hadronically decaying taus of opposite electric charge was considered. No significant excesses were observed, leading to an interpretation in the $\tilde{\chi}_2^0, \tilde{\chi}_1^0$ mass plane given in Figure 5.3a. For a massless **LSP**, $\tilde{\chi}_2^0$ masses up to 760 GeV were excluded. In addition to mass points with a fixed stau and sneutrino mass parameter x (as defined in equation (5.1)), two benchmark points were investigated with x varying between 0.05 and 0.95. The CL_s significance for a scenario with lower mass splitting, investigating a signal point with $\tilde{\chi}_1^0$ mass of 100 GeV and $\tilde{\chi}_2^0$ mass of 250 GeV is shown in Figure 5.3b. The CL_s significance is here used to express the confidence level connected with the CL_s value - a detailed discussion of the statistical concepts behind the model-dependent exclusion discussed here is given in section 5.11.

As can be seen in both exclusion plots, the mass point $(\tilde{\chi}_2^0, \tilde{\chi}_1^0) = (250, 100)$ GeV is excluded by the analysis. For no values of x the CL_s significance has dropped below the dashed line, highlighting a confidence level below 95%. Even though there is a visible dependency on the stau mass parameter x on the sensitivity of the analysis, this dependency does not change the conclusion of the model investigation. This is a further motivation to continue with an assumption

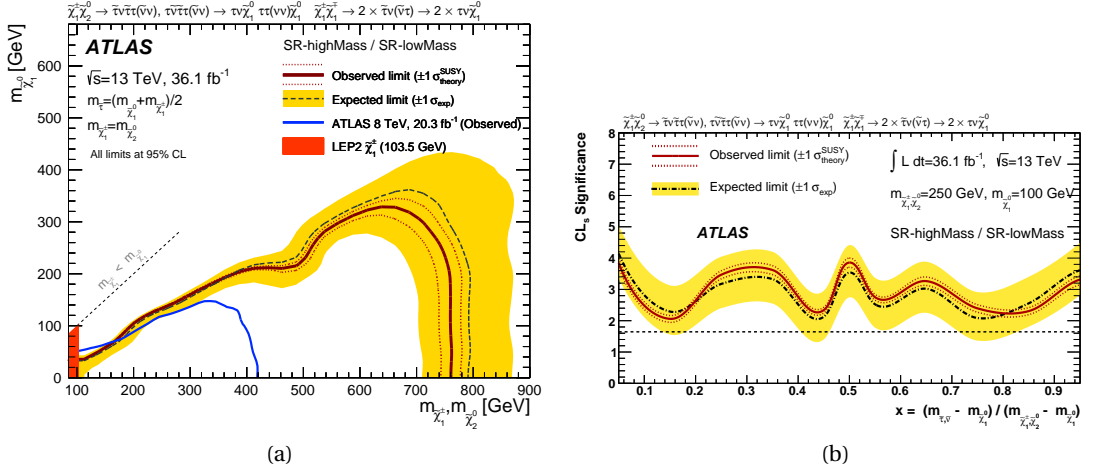


Figure 5.3: Results of previous model investigations in partial Run-2 data [99]. In its $m_{\tilde{\chi}_1^0}$ vs $m_{\tilde{\chi}_2^0}$ interpretation, as well as for a benchmark point in dependency of the stau mass splitting parameter x .

of $x = 0.5$ within the analysis described in the following.

The CMS Collaboration has performed a search for the production of a $\tilde{\chi}_1^\pm$ and $\tilde{\chi}_2^0$ with a consecutive decay via sleptons [103] that includes a decay via stau leptons as described above. This search in 2016-2018 proton-proton collisions used multiple final states, including multi-leptonic final states with a light lepton and at least one hadronically decaying tau. A parametric neural network was used to enhance the sensitivity to the supersymmetric particle signal. No significant excesses have been observed in this search, leading to the exclusion of $\tilde{\chi}_2^0$ masses up to 970 GeV for massless $\tilde{\chi}_1^0$. The larger available statistics offered by the full LHC Run-2 dataset used within this thesis allows for an investigation of the previously inaccessible regions of phase space, particularly towards higher $\tilde{\chi}_1^\pm$ masses and low mass splittings between $\tilde{\chi}_1^\pm$ and $\tilde{\chi}_2^0$. The same-sign di-tau final state considered in this thesis will offer an orthogonal approach to the analyses considered before, with different background compositions than in an opposite sign di-tau final state. The orthogonality of both approaches will significantly increase the phase space coverage of the model.

5.3 Analysis strategy

The simplified supersymmetric model presented in section 5.1 has been investigated in a final state with at least two hadronically decaying tau leptons, with the leading two taus of same electric charge. Apart from the hadronic tau final state, the composition of SM backgrounds largely depends on the additional objects in the event. One significant difference in the composition of the collision events considered is the amount of missing transverse momentum present. In regions with low and moderate amount of E_T^{miss} , the dominant processes have E_T^{miss} originating from single neutrinos or from mis-measurements. SM decays involving more neutrinos in the decay chain can lead to higher E_T^{miss} . Differences in the magnitude of missing momentum in the event are directly connected with differences in the assumed masses of the supersymmetric particles. The lightest neutralino, $\tilde{\chi}_1^0$, will not decay into SM particles, nor interact with

the detector material. Therefore the magnitude of missing transverse energy reconstructed is connected with the mass and momentum of the $\tilde{\chi}_1^0$. To target different mass ranges of the simplified model, two strategies have been designed. One targeting low $\tilde{\chi}_1^0$ masses as well as low mass splittings between the $\tilde{\chi}_1^0$ and $\tilde{\chi}_1^\pm$, a second scenario targets high $\tilde{\chi}_1^0$ and $\tilde{\chi}_1^\pm$ masses, leading to higher E_T^{miss} .

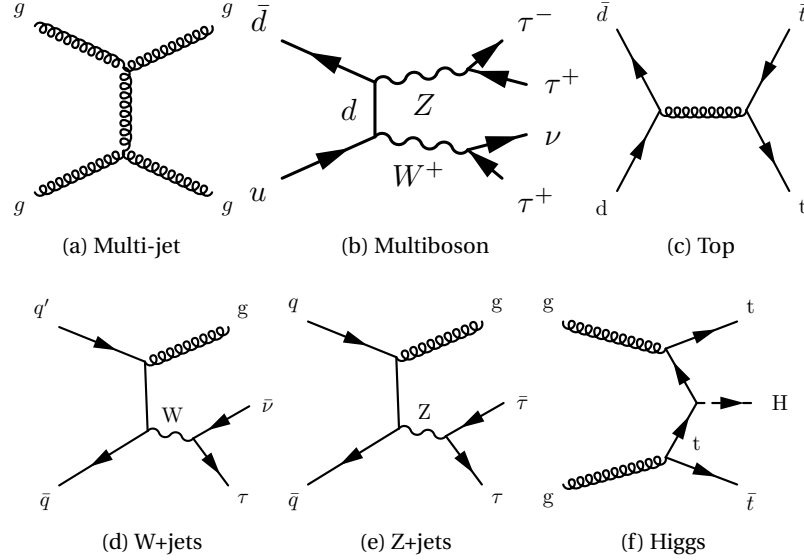


Figure 5.4: Overview of SM processes contributing to a di-tau final state.

An overview of the SM processes considered, which can enter a di-tau final state is given in Figure 5.4. Here only a few selected feynman diagrams for these SM processes are shown for illustration. *Multi-jet* processes include all QCD processes that end up in a final state with multiple jets. The example shown in Figure 5.4a shows a gluon fusion process. The parton showering of these gluons into jets can lead to jets that are mis-identified as hadronically decaying tau leptons. In *Multi-boson* processes, the associate production of multiple SM Z or W bosons can lead to a final state with two tau leptons. This is governed by the branching ratios of the Z and W boson decaying into tau leptons (3.37% and 11.38% respectively [32]). This also applies to the associate production of W or Z bosons with jets, as shown in Figures 5.4d and 5.4e. In this single boson productions, at least one of the hadronic taus in the final state is a so-called *fake tau*, originating from mis-identified jets. Processes associated with top quarks like the top quark pair production shown in Figure 5.4c can contribute to a di-tau final state both through hadronically decaying taus or mis-identified, fake taus. This is due to the decay of the top quarks into a bottom quark and W boson, which can consecutively decay into a tau lepton. In this thesis, all SM processes containing a Higgs boson, even in association with top quarks as depicted in Figure 5.4f are considered as *Higgs* processes. Similar to the top associated processes, whether the final state tau objects are misidentified jets or tau leptons depends on the decay of the Higgs boson as well as the top quark decay. The background estimation techniques described within section 5.9 do not separate the backgrounds based on the number of fake taus, but rather based on the SM processes as highlighted in Figure 5.4.

5.4 Data and simulation samples

An introduction to Monte Carlo simulation principles used in particle physics as well as an overview of the Monte Carlo generators of importance to this thesis was given in section 3.3. In the following, details about the simulated events used in this analysis for the various **SM** backgrounds as well as **SUSY** signal is given.

For all samples considered here, PYTHIA8 was used to overlay simulated soft QCD processes. This simulation is usually performed before the exact pile-up conditions in data are known. Therefore the simulation is corrected through re-weighting of events to match the year-by-year pileup conditions described in section 2.1.

Top related processes include top quark pair production ($t\bar{t}$) as well as single-top production via s-, t- and Wt-channels. These processes were simulated using POWHEG, interfaced with PYTHIA8 for the parton showering. POWHEG includes a next-to-leading order matrix element calculation. A Next-to-Next-to-Leading Order (**NNLO**) cross section calculation, including re-summation of Next-to-Leading-Logarithmic (**NLL**) soft-gluon terms was used to normalise the top quark pair production [104–110]. Single top production via the Wt-channel was normalised using **NNLO** cross sections with Next-to-Next-to-Leading-Logarithmic (**NNLL**) corrections, s- and t-channels were normalised using NLO cross section calculations [111, 112]. Top quark pair productions with an additional W or Z boson were simulated using MadGraph5_aMC@NLO for a Next-to-Leading Order (**NLO**) matrix element calculation, in combination with PYTHIA8 for fragmentation and hadronisation. The cross-section calculation was done at next-to-leading order [113, 114].

W/Z + jets production was generated using Sherpa, with **NLO** matrix elements with up to two additional partons and Leading Order (**LO**) with four additional partons. All decays of W into $e/\mu/\tau + \nu$ were considered. For the Z boson production in association with jets, $Z \rightarrow ee$, $Z \rightarrow \mu\mu$, $Z \rightarrow \tau\tau$ as well as $Z \rightarrow \nu\nu$ decay was considered. The cross-sections used were next-to-next-to leading order [115].

Multi-boson production includes di-boson as well as tri-boson production, with the **SM** bosons here excluding the Higgs boson. Di-boson samples including WW, WZ and ZZ production decaying semi- or fully leptonic were generated using Sherpa. Tri-boson samples simulated with Sherpa were also included. The matrix elements were generated at **NLO**.

Higgs boson related events produced in gluon-gluon fusion and vector-boson fusion were generated using POWHEG next-to-leading order matrix element in combination with PYTHIA8 parton showering. The production of a Higgs boson in association with a vector boson was simulated using PYTHIA8; the production of a Higgs boson in association with a top pair was simulated using MadGraph5_aMC@NLO. Cross-sections from [116] were used to normalise the samples.

SUSY signal samples were generated using MadGraph5_aMC@NLO in combination with PYTHIA8. The signal cross section was calculated up to next-to-leading order in QCD coupling constant,

including resummation up to next-to-leading logarithmic accuracy using the RESUMMINO framework [117, 118]. Uncertainties on the nominal cross section were included based on an envelope of variations of PDF as well as factorisation and renormalisation scales [119]. In the simplified model described in section 5.1, two parameters of the model are free. The masses of the $\tilde{\chi}_1^\pm / \tilde{\chi}_2^0$ as well as the LSP mass, $\tilde{\chi}_1^0$. A set of signal samples have been generated, varying the two mass parameters. An overview of the available signal mass points can be seen in Figure 5.5. Towards the kinematic diagonal, with small mass differences between $\tilde{\chi}_1^\pm$ and $\tilde{\chi}_1^0$, a finer granularity in signal mass points has been chosen. In this phase space region, small mass differences can lead to noticeable differences to the analysis' signal selection efficiency. A finer granularity allows for a more stable extrapolation of the analysis' sensitivity and helps avoid fluctuations in sensitivity due to statistical fluctuations.

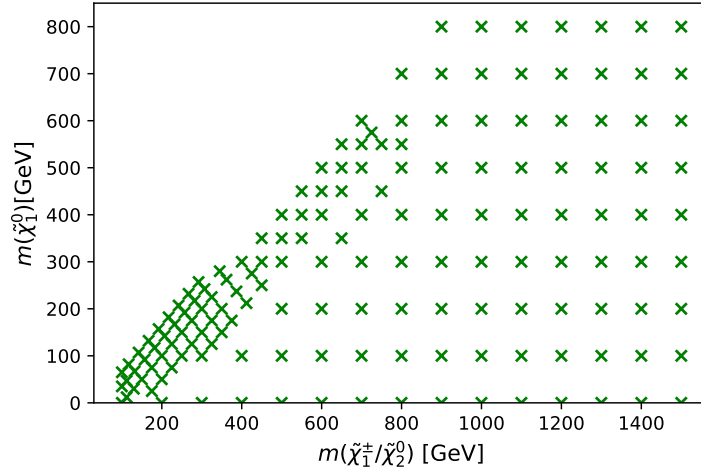


Figure 5.5: Visualisation of the available signal mass points.

Data is collected by the ATLAS detector as described throughout chapter 2. A total of 139 fb^{-1} integrated luminosity collected during Run-2 of data-taking has been analysed. The selection procedure for collision events is described in section 5.5. These selection criteria are mimicked in the Monte Carlo simulation.

5.5 Event selection

Three types of proton-proton collision events are considered: Events are selected with at least two hadronically decaying tau leptons, for the definition of signal and control regions. For background estimation and validation, events are selected with either exactly one muon and at least one tau lepton, or two muons and at least one tau lepton. These events are selected through the use of multiple triggers, summarized in table 5.1, together with the offline cuts required when a given trigger is used. As can be seen in table 5.1, the tau trigger includes a medium1 selection, specifying the tau trigger BDT identification requirement with at least one associated track. The tracktwo specification in the trigger highlights that a two-step tracking procedure is used. From 2015-2017 this two-step tracking was performed as a fast tracking step,

in 2018 the EF highlights the tracking procedure being performed at the precision step. The use of a ditau + E_T^{miss} trigger allows for lower tau p_T thresholds. Due to a slow turn on in efficiency of the E_T^{miss} trigger, a cut of 150 GeV is required in order to reach the trigger efficiency plateau. For the single muon trigger, a combination of the lowest unprescaled, isolated trigger (i1oose) in 2015, ivarmedium from 2016 onwards) with higher momentum threshold is used.

asymmetric di-tau trigger		offline requirements [GeV]
2015-2017	HLT_tau80_medium1_tracktwo_L1TAU60_tau50_medium1_tracktwo_L1TAU12	$\tau_1 p_T > 95$ $\tau_2 p_T > 60$
2018	HLT_tau80_medium1_tracktwoEF_L1TAU60_tau60_medium1_tracktwoEF_L1TAU40	$\tau_1 p_T > 95$ $\tau_2 p_T > 75$
ditau + E_T^{miss} trigger		offline requirements [GeV]
2015-2017	HLT_tau35_medium1_tracktwo_tau25_medium1_tracktwo_xe50	$E_T^{\text{miss}} > 150$ $\tau_1 p_T > 50$ $\tau_2 p_T > 40$
2018	HLT_tau60_medium1_tracktwoEF_tau25_medium1_tracktwoEF_xe50	$E_T^{\text{miss}} > 150$ $\tau_1 p_T > 75$ $\tau_2 p_T > 40$
single muon trigger		offline requirements [GeV]
2015	HLT_mu20_i1oose_L1MU15 HLT_mu50	$\mu_1 p_T > 50$
2016-2018	HLT_mu26_ivarmedium HLT_mu50	$\mu_1 p_T > 50$

Table 5.1: Trigger strategy for the used Run-2 dataset.

After the events are selected by the triggers, multiple steps of *event cleaning* are applied. This starts with removing runs of data-taking that are not included in a so-called Good Runs List (GRL). GRLs are used during data-taking as a result of dedicated monitoring and data-quality checks to record the detector status and mark periods of stable data-taking useful for physics analyses [120]. Events are required to have at least one primary vertex [121], where a primary vertex is defined as a vertex with at least two associated tracks with $p_T > 400$ MeV. In case an event has more than one primary vertex, the vertex with the larger momentum of associated tracks is selected. Additionally, to remove events with cosmic muons crossing the ATLAS detector, events with muon candidates with large longitudinal or transverse impact parameters ($|z_0| > 1$ mm or $|d_0| > 0.2$ mm, respectively) are removed.

5.6 Object definitions

SM particles and their reconstruction and identification as *physics objects* in ATLAS is a multi-step process with different choices of possible properties. A first, loose, *baseline* definition of objects is used to identify candidate objects. At this stage, objects can be considered by multiple reconstruction algorithms, therefore an *overlap removal* between close-by objects is performed. Stricter requirements are then required on top of baseline objects to define *signal* objects, used in the analysis.

Hadronically decaying tau leptons follow the offline reconstruction and identification procedures described in section 3.2.4. Baseline taus have a minimum p_T of 20 GeV and lie outside the detector's transition region ($|\eta| \in [0., 1.37] \text{ or } [1.52, 2.5]$) to avoid inefficiencies in reconstruction and identification due to inactive material. The tau candidates have either exactly one asso-

ciated track or three associated tracks. A *medium* BDT working point is required to separate taus from electrons. A *medium* RNN identification working point is required for baseline and signal tau leptons to distinguish hadronically decaying taus from jets. For some background estimation techniques, described in section 5.9, the baseline tau ID working point is lowered to *very loose*.

Jet reconstruction is seeded by particle flow jets with the anti- k_T clustering algorithm and a 0.4 radius parameter. Their minimum p_T is 20 GeV, with a pseudorapidity $|\eta| < 2.8$. Events with at least one jet from non-collision backgrounds are removed [122]. Non-collision background for jets can come from beam-induced background (such as proton losses before the ATLAS interaction point), cosmic ray showers or calorimeter noise. A *Tight* working point of the **JVT** is chosen, together with a maximum transverse momentum of 60 GeV.

Jets associated with a decay of a b-quark are based on the particle flow jets with the anti- k_T clustering algorithm, but with a slightly smaller pseudorapidity range of $|\eta| < 2.5$. The DL1 algorithm [123] is used to identify jets as associated to a b-quark. A b-jet efficiency working point of 77% is used, which offers a light quark rejection factor over 100 for a c-jet rejection of five.

Electron objects at baseline level have a minimum transverse momentum of 4.5 GeV and a pseudorapidity of $|\eta| < 2.47$, to stay within the coverage of the electromagnetic calorimeter. An electron identification working point of *LooseAndBLayerLLH* is required for the likelihood discriminant discussed in section 3.2.1. Quality restrictions on the transverse and longitudinal impact parameter significances are applied ($\frac{d_0}{\sigma(d_0)} < 5$, $z_0 \sin \theta < 0.5$ mm, respectively), with σ denoting the uncertainty on the impact parameters. Signal electrons need to pass a *TightLLH* likelihood identification criteria as well as the isolation working points *FCLoose* for $p_T < 200$ GeV or a loosened, calorimeter only working point, *FCHighPtCaloOnly* for $p_T > 200$ GeV.

Muon candidates at baseline level are defined as having $p_T > 3$ GeV, $|\eta| < 2.7$, a *medium* ID requirement and a cut on the quantity $z_0 \sin(\theta)$ (< 0.5 mm). If the candidate muons have a large uncertainty on their momentum to charge measurement ($\frac{\sigma(q/p)}{|q/p|} > 0.2$), they are rejected. Muons with larger transverse momentum of $p_T > 25$ GeV as well as $\frac{d_0}{\sigma(d_0)} < 3.0$, together with a *FCLoose* isolation are defined as signal muons.

Based on the baseline objects described above, an overlap removal procedure is performed to remove ambiguities in the object definitions. The steps performed are described and summarised in table 5.2. The steps in the overlap removal procedure are performed consecutively, as described in the first column of table 5.2. Two types of baseline objects are compared with each other, based on their closeness in terms of ΔR as well as other criteria. In each step, if the overlap criteria highlighted under *Condition* is met, the object listed under the *Object removed* column gets discarded, whereas the *Object compared to* is kept in the event. This way ambiguities in the object reconstruction are resolved and double counting of detector signals as two different types of objects is avoided.

Step	Object removed	Object compared to	Condition	Further Comment
1	jet	muons	multiple overlap criteria	Includes restrictions on ΔR , jet track multiplicity, muon ID/isolation
2	tau	electron	$\Delta R < 0.2$	
3	tau	muon	$\Delta R < 0.2$	
4	electron	muon	shared ID track	
5	jet	electron	$\Delta R < 0.2$	
6	electron	jet	$\Delta R < rad$	$rad = \min(0.04 + \frac{10 \text{ GeV}}{p_T(e)}, 0.4)$
7	jet	muon	Number of tracks < 3 $\Delta R < 0.2$	
8	muon	jet	$\Delta R < rad$	$rad = \min(0.04 + \frac{10 \text{ GeV}}{p_T(\mu)}, 0.4)$
9	jet	tau	$\Delta R < 0.2$	

Table 5.2: Summary of the overlap removal process.

5.7 Signal region, control region and validation region definitions

In this analysis, three different regions are considered, referring to specific areas in the kinematic phase space of the collected events (see Figure 5.6).

Signal Regions (SRs) are regions in phase space showing the largest possible contributions of the **BSM** signal searched for and the most promising differentiation between the signal and **SM** background. In this regions, a *blinded analysis approach* is followed. Until all background estimations in the signal region with their associated systematic uncertainties are finalised, no comparison of data to the background or signal expectation can be performed.

Control Regions (CRs) are used to estimate the backgrounds in the signal region by comparing the prediction of background processes with the data observed in the said region. They are designed to be enriched with one specific background. Details about the way in which backgrounds in the **SRs** are estimated are given later in this chapter. Control Regions are orthogonal to signal regions to make a statistically independent measurement of the background normalisation.

Validation Regions (VRs) are defined in combination with control regions in order to validate the extrapolation from **CR** to **SR**.

5.8 Signal region optimisation

In the following, a description of the optimisation procedure used to define the signal regions is given. A grid of simulated signal events obtained by varying the masses of $\tilde{\chi}_1^0$ and $\tilde{\chi}_1^\pm / \tilde{\chi}_2^0$ has been used to perform the signal region optimisation. The overall signal mass point grid can be seen in Figure 5.5.

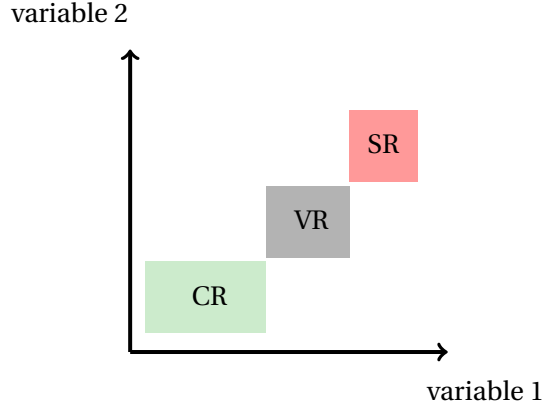


Figure 5.6: Visualisation of signal, control and validation regions and a typical arrangement in phase space.

5.8.1 Choice of kinematic variables

To understand the difference between a potential supersymmetric particle production compared to a [SM](#) process, various kinematic variables can be studied.

One of the kinematic variables of interest in a di-tau final state is the *visible mass* of the di-tau system, $m_{vis}(\tau_1, \tau_2)$, constructed using the four-momenta of the two leading tau candidates in the event. This variable only takes into account the visible components of the hadronic decaying tau, therefore not considering the missing momentum carried by the tau neutrinos.

To account for the invisible decay products, the missing transverse momentum can be included in an adapted "invisible" mass, the transverse mass m_T :

$$m_T = \sqrt{2p_T^\ell E_T^{\text{miss}}(1 - \cos(\Delta\phi(\vec{\ell}, \vec{p}_T^{\text{miss}}))} \quad (5.2)$$

For example, in the case of a leptonic W-bosons decay, the m_T shows an endpoint at the mass of the W boson.

In the case of two hadronically decaying tau leptons, the sum of the transverse masses m_{Tsum} can be powerful in discriminating [SM](#) background from signal:

$$m_{Tsum} = m_T(\tau_1) + m_T(\tau_2) \quad (5.3)$$

With $m_T(\tau_1)$ denoting the transverse mass as defined in equation (5.2) with the lepton as the leading, highest momentum, hadronic decaying tau lepton. The transverse mass concept can be extended to pair produced particles partially decaying into invisible particles, using the definition by Barr, Lester, Stephens and Summers [124, 125] of the stransverse mass:

$$m_{T2}(\mathbf{p}_T^{\ell_1}, \mathbf{p}_T^{\ell_2}, \mathbf{p}_T^{\text{miss}}) \equiv \min_{\mathbf{p}_1^{\text{miss}} + \mathbf{p}_2^{\text{miss}} = \mathbf{p}_T^{\text{miss}}} \left[\max\{m_T(\mathbf{p}_T^{\ell_1}, \mathbf{p}_1^{\text{miss}}), m_T(\mathbf{p}_T^{\ell_2}, \mathbf{p}_2^{\text{miss}})\} \right] \quad (5.4)$$

Here the momentum ($\mathbf{p}_T^{\ell_1}, \mathbf{p}_T^{\ell_2}$) of the two leptons in the event (for example the visible part of the hadronic tau decay) are combined into a transverse mass with parts of the missing transverse momentum, split into $\mathbf{p}_1^{\text{miss}}$ and $\mathbf{p}_2^{\text{miss}}$. This variable shows an endpoint at the mass of the pair-produced particle, leading to a usually lower end-point of the distribution for **SM** background processes in comparison to the **SUSY** model considered. The mass of the invisible particles is assumed to be zero.

If an event includes more than two leptons (with a maximum number of leptons n_ℓ), it can be useful to perform a maximisation over the m_{T2} values resulting from all possible lepton pairs:

$$m_{T2}^{\text{max}} = \max_{\substack{i=1,\dots,n_\ell \\ j=2,\dots,n_\ell \\ i \neq j}} \left[m_{T2}(\mathbf{p}_T^{\ell_i}, \mathbf{p}_T^{\ell_j}, \mathbf{p}_T^{\text{miss}}) \right] \quad (5.5)$$

5.8.2 SR optimisation procedure

As starting point of the optimisation, the kinematic variables described in the previous section are studied for **SM** background events and signal events. In the following plots, all **SM** background distributions shown are obtained from Monte Carlo. In Figure 5.7, some kinematic variables are shown after the selection with an asymmetric di-tau trigger selection as well as a b-jet veto and light lepton veto. A selection of signal points is used to gauge the effectiveness of the variables to isolate a signal. In Figure 5.7a, m_{T2}^{max} , as defined in (5.5) can be compared with Figure 5.7b, showing m_{T2} . The maximisation over all tau pairs in the event leads to a slight improvement in sensitivity compared to m_{T2} calculated using the two leading tau candidates. In the lower panels of Figure 5.7, a simplified sensitivity measure Z_n [126] including a 30% flat systematic uncertainty is used to gauge the sensitivity of each variable to the signal model. A Z_n implementation of the RooStats [127] package within the ROOT [128] software framework is used. This sensitivity measure is used to estimate the signal to background separation power as fully estimated with hypothesis testing as described in section 5.11. As can be seen in Figures 5.7c and Fig. 5.7d in comparison to the sum of both m_T shown in Figure 5.7e, summing the transverse mass of the two leading taus offers a slightly higher discriminating power than the single transverse masses.

In case of a low $m(\tilde{\chi}_1^\pm, \tilde{\chi}_2^0)$ (low mass scenario, SR-C1N2SS-LM), a cut of $E_T^{\text{miss}} < 150$ GeV is introduced. The case of high $\tilde{\chi}_1^\pm, \tilde{\chi}_2^0$ mass (SR-C1N2SS-HM) is defined by $E_T^{\text{miss}} > 150$ GeV. The effect of multiple cuts (not applied consecutively) on the overall sensitivity is given in Figure 5.8.

An $m_{T\text{sum}} > 200$ GeV selection was chosen because it gives a higher sensitivity toward the diagonal of the $(\tilde{\chi}_1^\pm / \tilde{\chi}_2^0, \tilde{\chi}_1^0)$ mass plane. The additional requirement $\Delta\phi(\tau_1, \tau_2) > 1.5$ is included in the signal region definition, to reduce the signal contamination when estimating the multi-jet background (see section 5.9.1. The optimisation for the high mass case followed a very similar approach, leading to the two orthogonal signal regions defined in Table 5.3.

An overview of the event yields in both signal regions is shown in table 5.4. All backgrounds

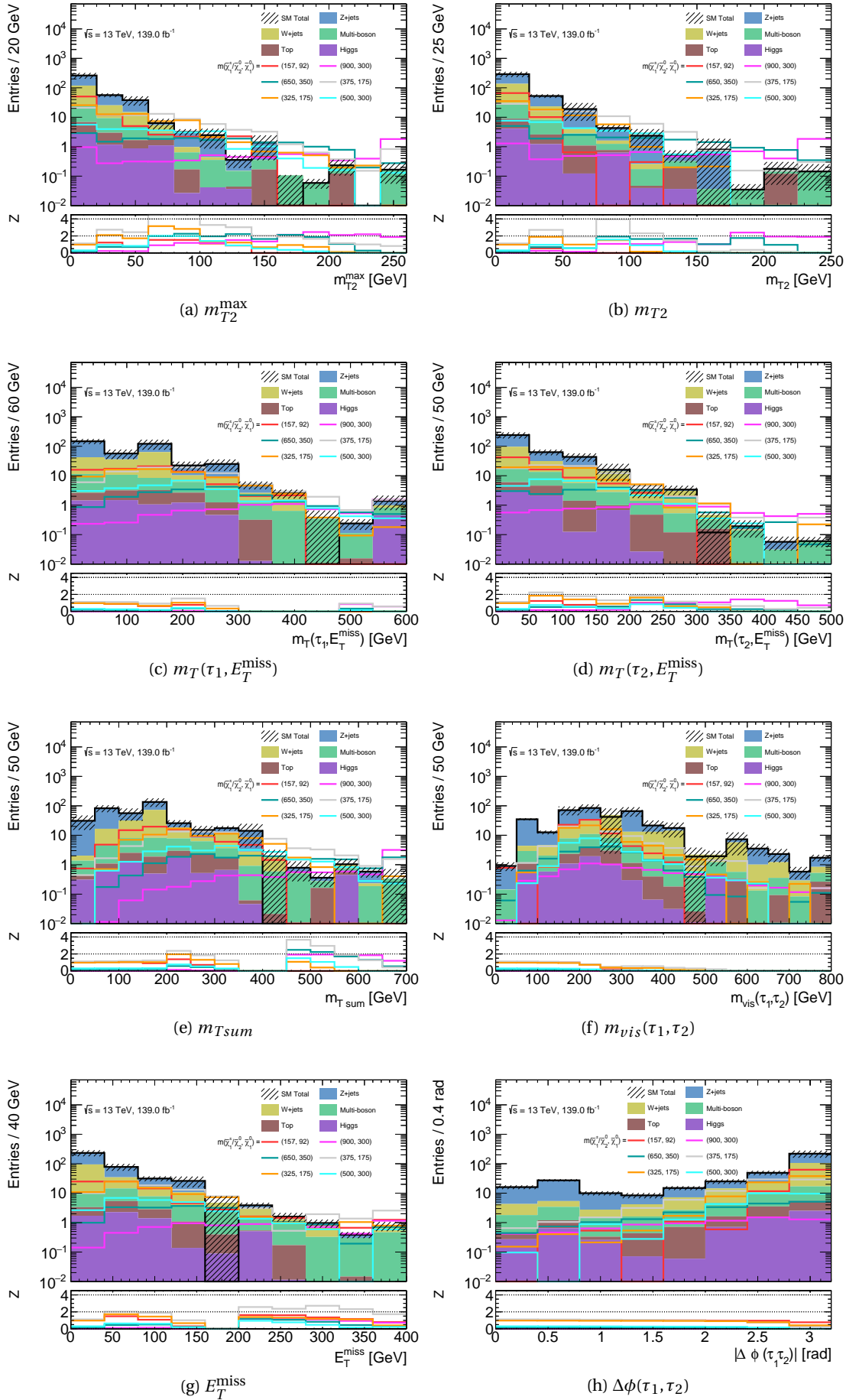


Figure 5.7: Kinematic variable distributions for SS scenario after a loose preselection. Error bands include statistical uncertainties only. The lower panel shows the significance Z_n including a 30 % systematic uncertainty assumption.

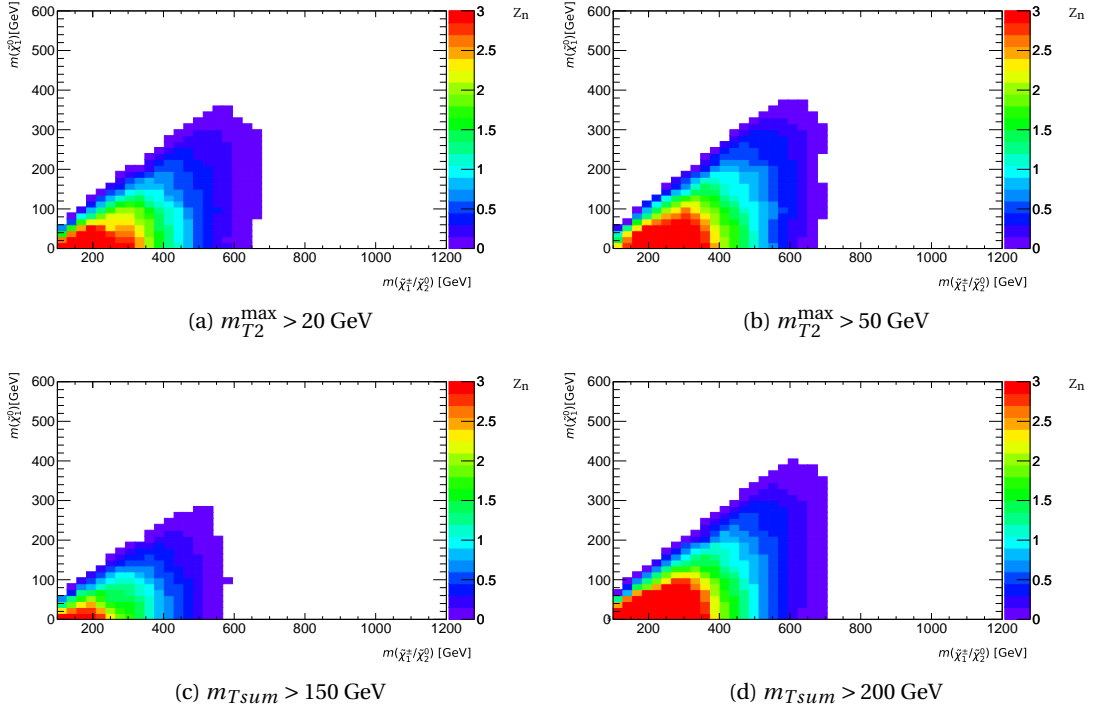


Figure 5.8: Significance estimation including a 30% flat systematic uncertainty.

SR-C1N2SS-LM	SR-C1N2SS-HM
≥ 2 medium taus (SS)	
b -jet veto	
$\Delta\Phi(\tau_1, \tau_2) > 1.5$	-
$N_{jets} < 3$	-
$m_{Tsum} > 200 \text{ GeV}$	$m_{Tsum} > 450 \text{ GeV}$
$m_{T2}^{\max} > 80 \text{ GeV}$	
asymmetric di-tau trigger	di-tau+ E_T^{miss} trigger
$E_T^{\text{miss}} < 150 \text{ GeV}$	$E_T^{\text{miss}} > 150 \text{ GeV}$
τ_1 and τ_2 p_T requirements described in Table 5.1 in Section 5.5	

Table 5.3: Summary of selection requirements for the signal regions.

apart from the Multi-jet background are taken from MC simulation with only statistical uncertainties included below. The Multijet estimation is performed using a data-driven method, discussed in detail in section 5.9.1.

Kinematic distributions in the signal regions, with requirements on the shown variable removed ("N-1 distributions"), can be seen in figure 5.9 for SR-C1N2SS-LM, and figure 5.10 for SR-C1N2SS-HM, already including the multi-jet estimation as well as systematic uncertainties discussed in section 5.9 and 5.10, respectively.

Further kinematic distribution in both signal regions can be seen in 5.11 and 5.12, respectively. This clearly shows that no further requirements on other kinematic variables are able to gain in sensitivity, at least not while allowing for sufficient remaining statistics in the SM background simulations.

The estimated sensitivity of both signal regions, using the significance measure Z_n is shown

SM-process	SR-C1N2SS-LM	SR-C1N2SS-HM
Top	0.01 ± 0.01	0.84 ± 0.36
Multi-boson	0.47 ± 0.11	0.81 ± 0.21
Multi-jet	0.94 ± 0.27	-0.086 ± 0.31
W+jets	0.32 ± 0.32	0.10 ± 0.10
Z+jets	0.20 ± 0.20	0.59 ± 0.56
Higgs	0.00 ± 0.00	0.02 ± 0.00
SM total	1.95 ± 0.48	2.35 ± 0.80
Ref. point (325, 175)	7.80 ± 1.27	2.26 ± 0.71
Ref. point (500, 300)	3.78 ± 0.65	5.62 ± 0.88
Ref. point (900, 300)	0.84 ± 0.07	6.23 ± 0.21

Table 5.4: Number of events in the signal regions for SM backgrounds, including statistical uncertainties. The SM MC backgrounds are normalised to 139 fb^{-1} . The multi-jet contribution is estimated from data with a simplified ABCD method described in Section 5.9.1. Only statistical uncertainty are considered for MC estimated processes and multi-jet.

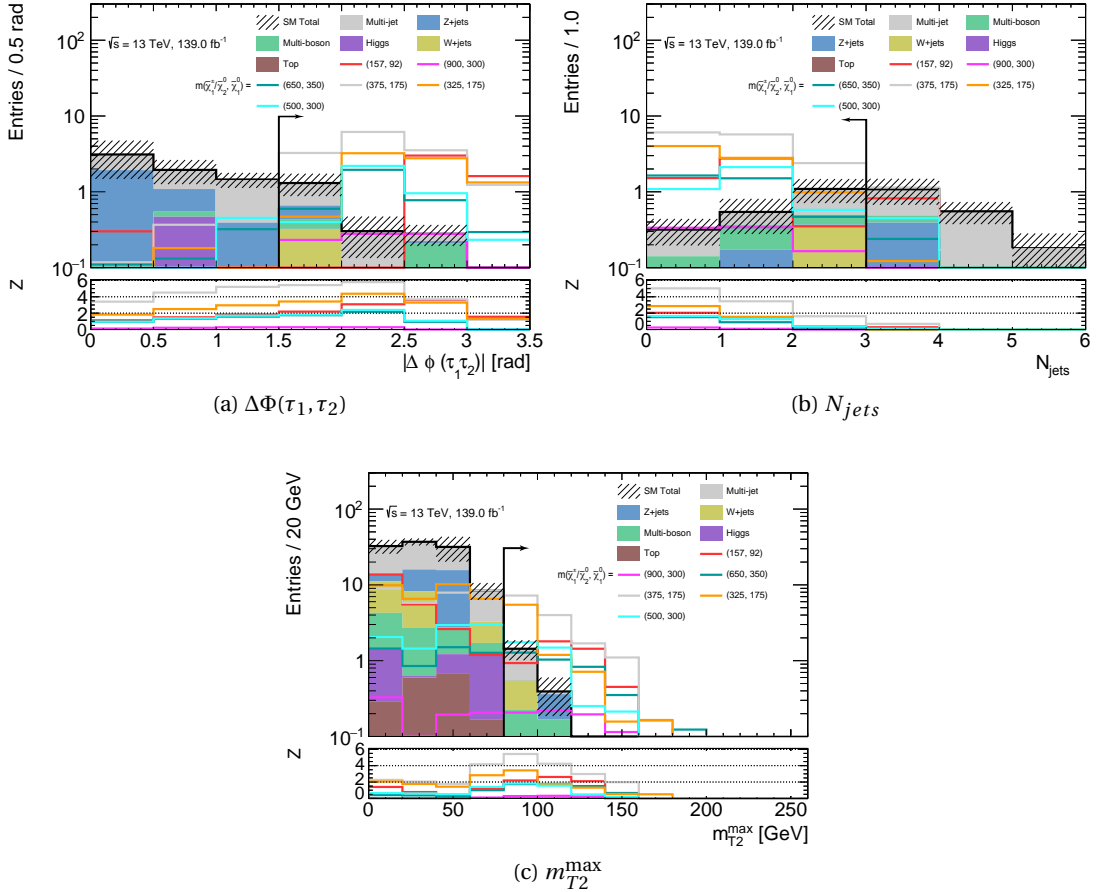


Figure 5.9: “N-1” distributions of relevant kinematic variables after SR-C1N2SS-LM requirements, except the one on the shown variable, have been applied. The stacked histograms show the expected SM backgrounds estimated from MC, normalised to 139 fb^{-1} as well as Multi-jet expectation as described in section 5.9.1. Statistical uncertainties and systematic uncertainties as discussed in section 5.10 are included in the error band.

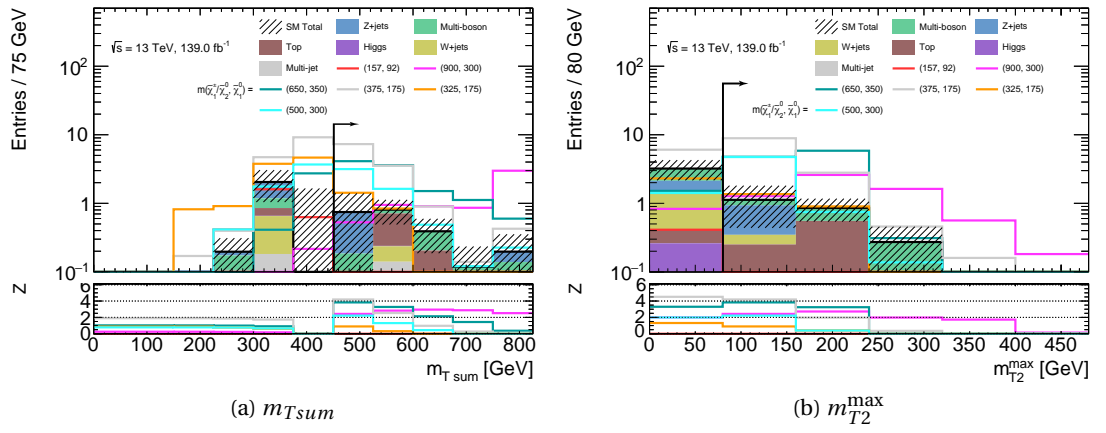


Figure 5.10: “N-1” distributions of relevant kinematic variables after SR-C1N2SS-HM requirements, except the one on the shown variable, have been applied. The stacked histograms show the expected SM backgrounds estimated from MC, normalised to 139 fb^{-1} as well as Multi-jet expectation as described in section 5.9.1. Statistical and systematic uncertainties as discussed in 5.10 are included in the error band.

in figure 5.13. This is a first estimate of the sensitivity of these regions to the gaugino pair production under investigation.

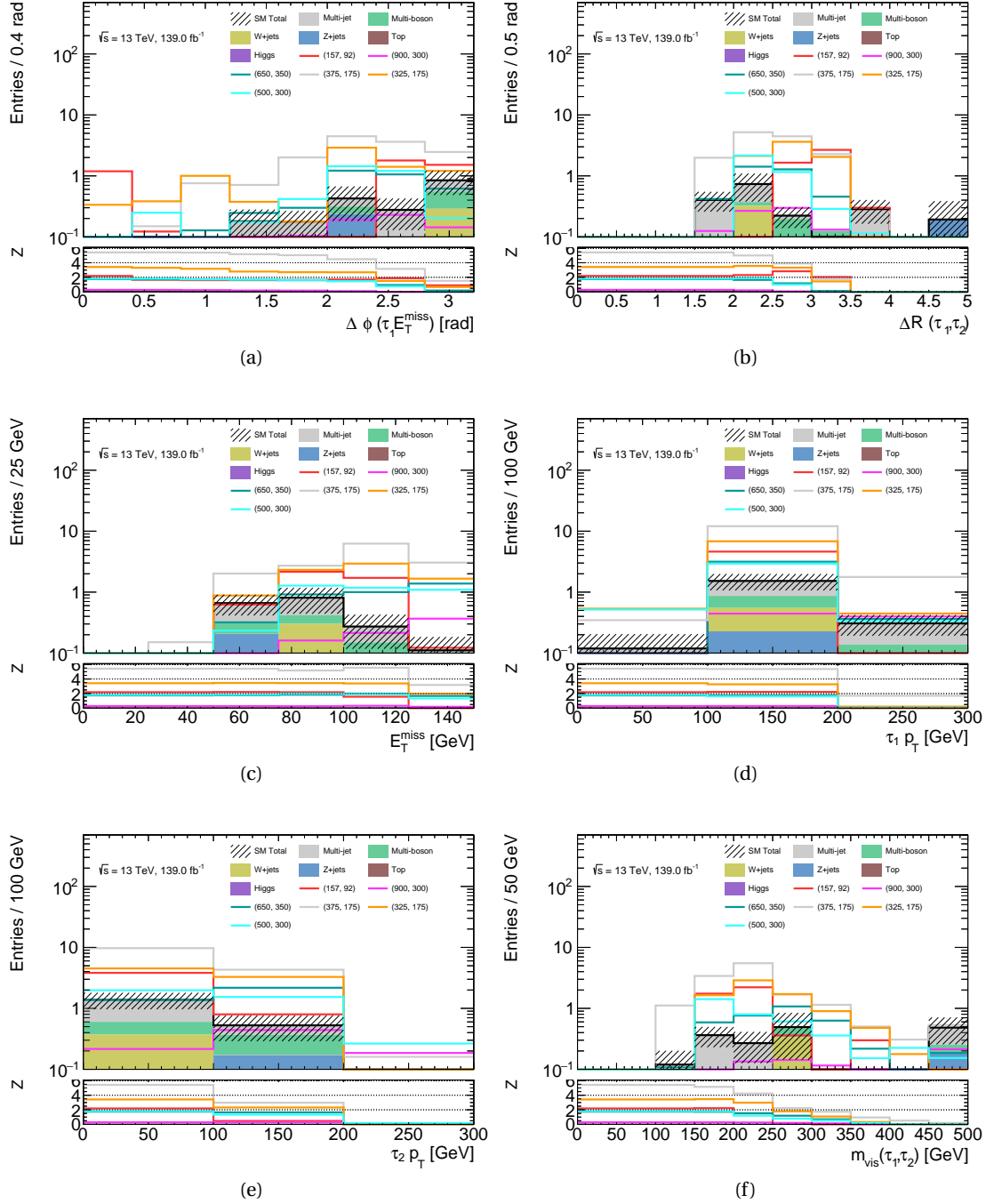


Figure 5.11: Remaining kinematic distributions in SR-C1N2SS-LM, for all variables not used in the signal region definition. The error band includes statistical and systematic uncertainties. The lower panel shows the significance Z_n including a 30 % systematic uncertainty assumption.

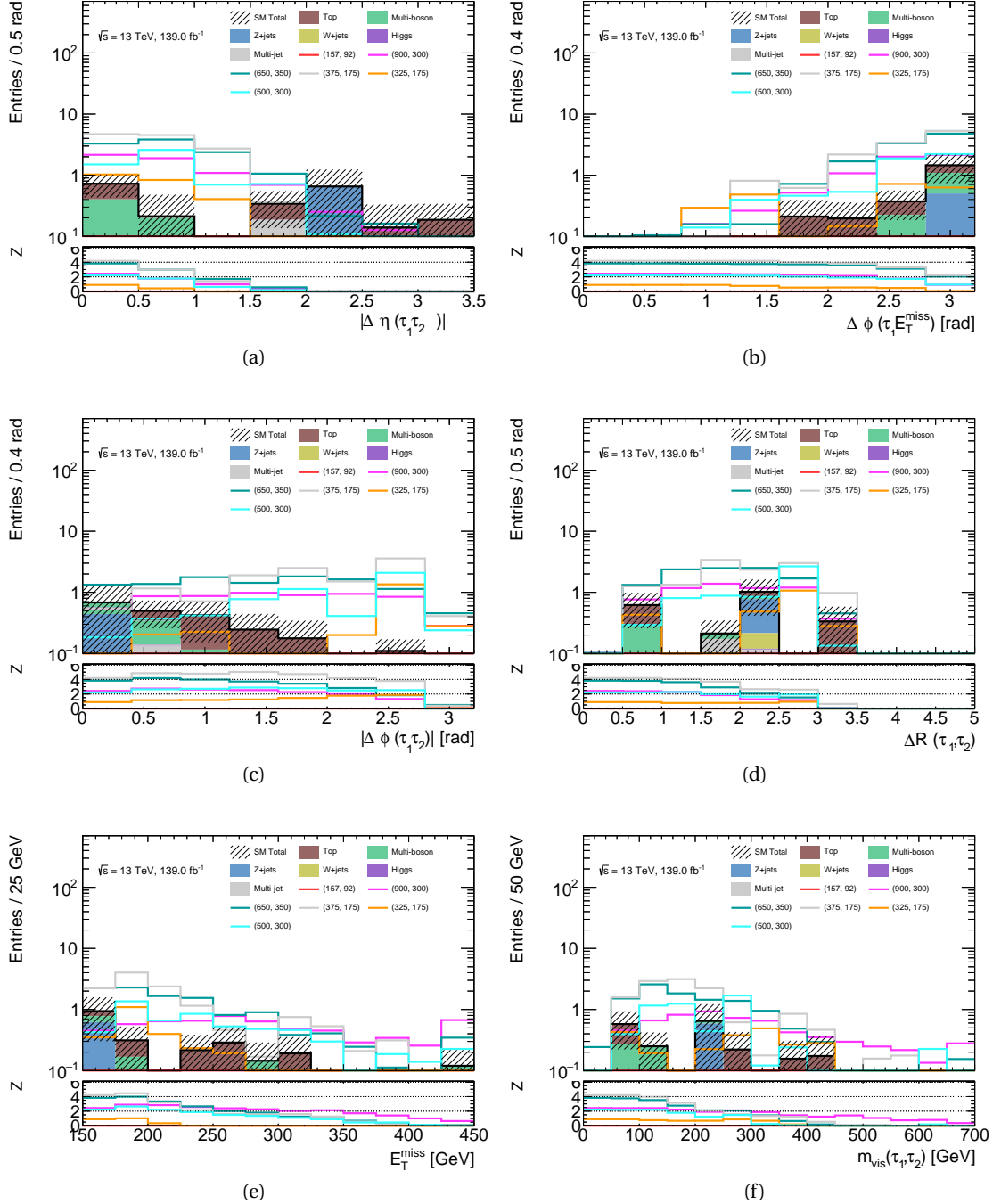


Figure 5.12: Remaining kinematic distributions in SR-C1N2SS-HM, for all variables not used in the signal region definition. The error band includes statistical and systematic uncertainties. The lower panel shows the significance Z_n including a 30 % systematic uncertainty assumption.

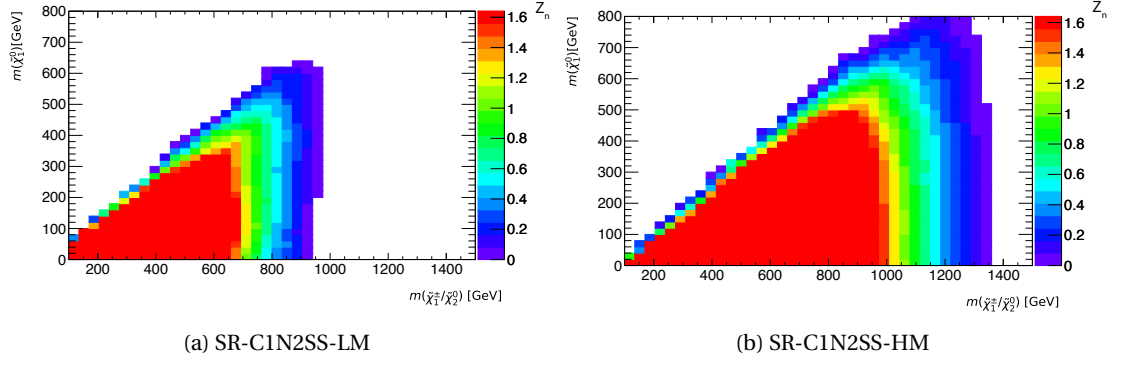


Figure 5.13: Significance distribution for the (a) SR-C1N2SS-LM, (b) SR-C1N2SS-HM for 139 fb^{-1} . The statistical uncertainty and 30% systematic uncertainty on SM backgrounds are included in the Z_N calculation.

5.9 Standard Model background estimations

The analysis presented takes an inclusive approach to its background estimation strategies. Instead of separating backgrounds based on the number of fake taus or origin of fake taus, the backgrounds are estimated based on the underlying **SM** process, including prompt and fake tau leptons. **SM** processes dominated by QCD interactions, leading to multiple jets in the final state, can enter a di-tau final state through at least one jet being misidentified as hadronically decaying tau lepton. This background is estimated via a so called "ABCD" method. $W+$ jets events can similarly end up in a di-tau final state through at least one fake tau. A muon plus tau final state is used to normalise the Monte Carlo estimation of this process. Since top related backgrounds (with and without fake taus) are the leading contribution to the high mass signal region, an additional estimation of this background in a control region is performed. To validate the modelling of WW and WZ processes contributing to the SR-C1N2SS-HM, a validation region was designed, using a pair of opposite-sign muons to enhance the statistics of this process.

5.9.1 Estimation of Multi-jet background

The multi-jet **SM** background includes all strong interactions producing a final state with multiple jets. Due to the similarity of jets and tau signatures, this process is populating the final state considered in this analysis of at least two hadronically decaying taus. In contrast to the **SUSY** signal model of interest, this standard model process does not have large E_T^{miss} . Any missing transverse energy in the events is caused by mismeasurements. A quark or gluon jet could be misidentified as a one or three-prong tau, discarding some of the **ID** tracks that would otherwise be taken into account in the jet momentum. These unaccounted tracks can increase the instrumental E_T^{miss} . Due to the instrumental origin of the E_T^{miss} in the event, the multi-jet processes predominantly populate phase space regions with low missing transverse momenta. Since the multijet background originates in soft QCD processes, its simulation through Monte Carlo generators is unreliable, especially in high momentum phase spaces considered in this analysis. A data-driven estimation method, the *ABCD* method, is therefore used to extract a

multi-jet estimation from data.

Two kinematic variables are used to construct a set of orthogonal regions: the tau identification working point of the leading two taus and sum of the m_T of the two leading taus. Any additional cuts that have been defined in the signal region optimisation are not applied to the control and validation regions built for the ABCD method. A sketch of the regions described is given in figure 5.14. A detailed definition of the kinematic cuts applied to the regions in order to define the ABCD regions is given in table 5.5. The signal region phase spaces present the regions denoted as D within this methodology.

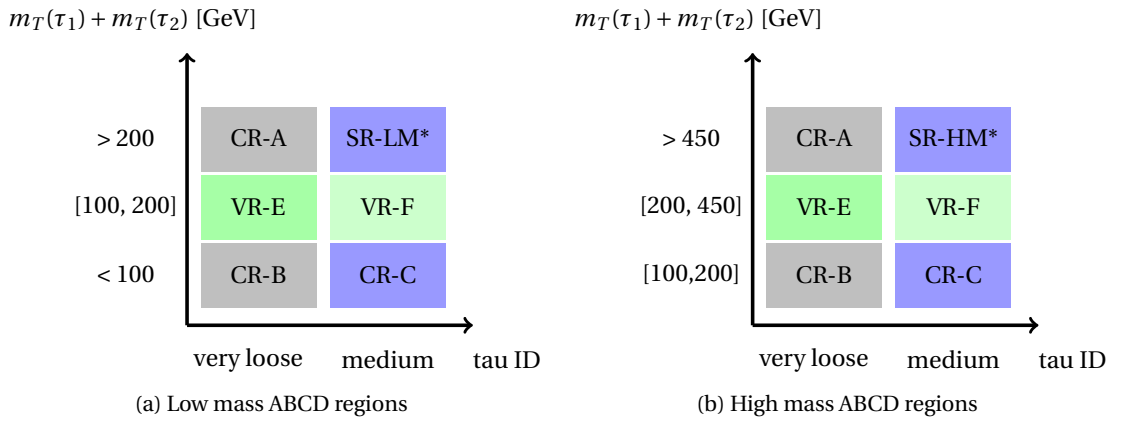


Figure 5.14: ABCD region illustration for the low and high mass signal regions Here only the cuts on $m_T(\tau_1) + m_T(\tau_2)$ and the tau-ID are shown. * As described in section 5.8.2, further requirements on other kinematic variables are applied to define the signal regions

CR-A	SR-LM	CR-A	SR-HM
≥ 2 very loose or loose τ 's < 2 medium τ 's $m_{Tsum} \geq 200$ GeV $\Delta\Phi(\tau_1, \tau_2) \geq 1.5$	≥ 2 medium τ 's - $m_{Tsum} \geq 200$ GeV $\Delta\Phi(\tau_1, \tau_2) \geq 1.5$	≥ 2 very loose or loose τ 's < 2 medium τ 's $m_{Tsum} \geq 450$ GeV $E_T^{miss} \geq 50$ GeV	≥ 2 medium τ 's - $m_{Tsum} \geq 450$ GeV $E_T^{miss} \geq 150$ GeV
VR-E	VR-F	VR-E	VR-F
≥ 2 very loose or loose τ 's < 2 medium τ 's $m_{Tsum} \in [100, 200]$ GeV $\Delta\Phi(\tau_1, \tau_2) \leq 1.5$	≥ 2 medium τ 's - $m_{Tsum} \in [100, 200]$ GeV $\Delta\Phi(\tau_1, \tau_2) \leq 1.5$	≥ 2 very loose or loose τ 's < 2 medium τ 's $m_{Tsum} \in [200, 450]$ GeV $E_T^{miss} \geq 50$ GeV	≥ 2 medium τ 's - $m_{Tsum} \in [200, 450]$ GeV $E_T^{miss} \geq 50$ GeV
CR-B	CR-C	CR-B	CR-C
≥ 2 very loose or loose τ 's < 2 medium τ 's $m_{Tsum} < 100$ GeV $\Delta\Phi(\tau_1, \tau_2) \leq 1.5$	≥ 2 medium τ 's - $m_{Tsum} < 100$ GeV $\Delta\Phi(\tau_1, \tau_2) \leq 1.5$	≥ 2 very loose or loose τ 's < 2 medium τ 's $m_{Tsum} \in [100, 200]$ GeV $E_T^{miss} \geq 50$ GeV	≥ 2 medium τ 's - $m_{Tsum} \in [100, 200]$ GeV $E_T^{miss} \geq 50$ GeV

Table 5.5: The multi-jet control region and validation region definitions for signal regions described in Table 5.3. Only those requirements regarding the $m_T(\tau_1) + m_T(\tau_2)$ that are different in the CRs/VRs with respect to the SRs are listed.

The multi-jet (MJ) contribution in CR-B and CR-C is obtained from the data yields in the respective regions, with all other background contributions from Monte Carlo simulation subtracted;

$$N_{CR-B/C}^{MJ} = N_{CR-B/C}^{data} - N_{CR-B/C}^{MC} \quad (5.6)$$

a transfer factor is extracted from the yields in CR-B and CR-C to extrapolate the multi-jet contribution to the medium ID validation and signal regions (VR-F and SR).

$$TF = \frac{N_{CR-C}^{MJ}}{N_{CR-B}^{MJ}} \quad (5.7)$$

The systematic uncertainty on the transfer factor is estimated in the validation regions using formula (5.8) and is visualised in Figure 5.15.

$$\Delta(TF)_{sys} = \left| \frac{N_{CR-C}^{MJ}}{N_{CR-B}^{MJ}} - \frac{N_{VR-F}^{MJ}}{N_{VR-E}^{MJ}} \right| \quad (5.8)$$

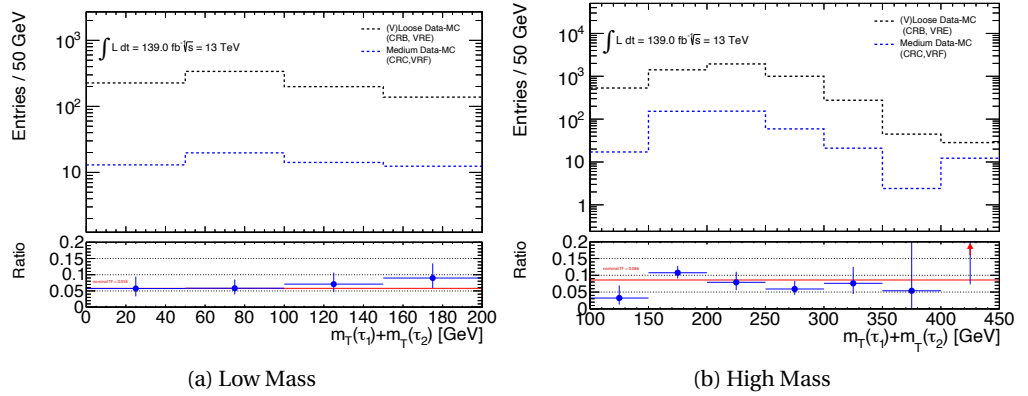


Figure 5.15: Dependency of the transfer factor on $m_T(\tau_1) + m_T(\tau_2)$ for low mass and high mass regions. Highlighted in the lower panel in red is the nominal used transfer factor value. All uncertainties are statistical only.

The multi-jet yield in the signal region is then given by the multi-jet contribution in CR-A (given through data subtracted by other SM contributions from Monte Carlo simulation) multiplied by the transfer factor with additional cuts. The results of the ABCD method are summarised in Table 5.6. The SM predictions are in agreement with the observed data counts in the multi-jet validation regions, as shown in Table 5.7.

In Figure 5.16 (Figure 5.17), distributions of the relevant kinematic variables are shown for data, SM expectations and illustrative SUSY benchmark models for the multi-jet validation regions VR-F-LM (VR-F-HM). The multi-jet contribution in VR-F is given through the multijet contribution in VR-E (as data subtracted by other SM contributions) times the transfer factor as defined in equation (5.7). The signal contamination in VR-F-LM is below 10%, in VR-F-HM below 30%. The SM background distributions are taken from MC simulation, except for the multi-jet contribution, which is estimated using the ABCD method described above. The distributions include statistical and systematic error on the ABCD method added in quadrature. Reasonable data and SM agreement are observed within uncertainty and show good extrapolation in m_{T2}^{\max} .

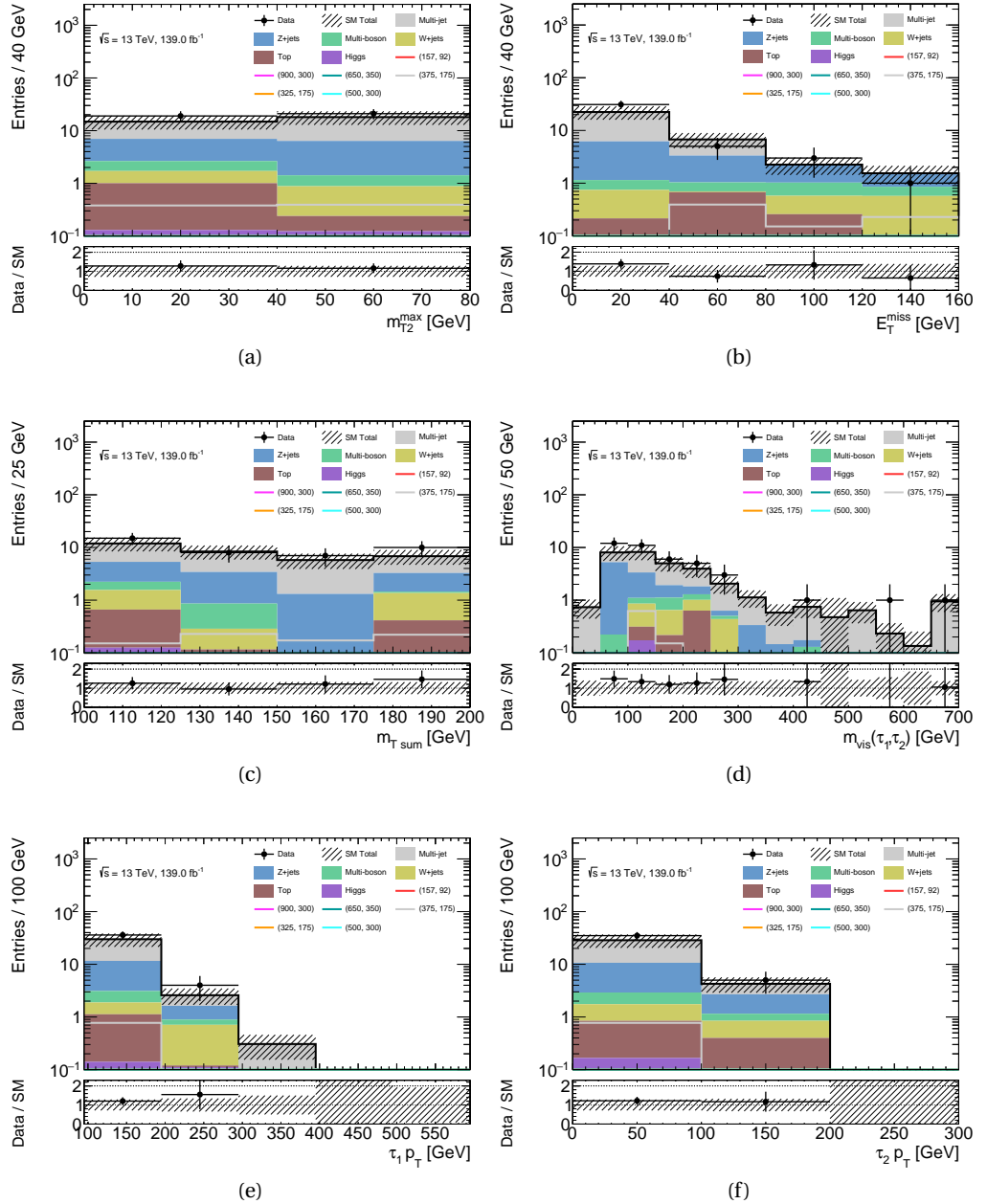


Figure 5.16: Data/MC distributions in VR-F-LM, the uncertainty band includes statistical and systematic uncertainties. No normalisation factors as extracted in the background-only fit described in section 5.12 are applied.

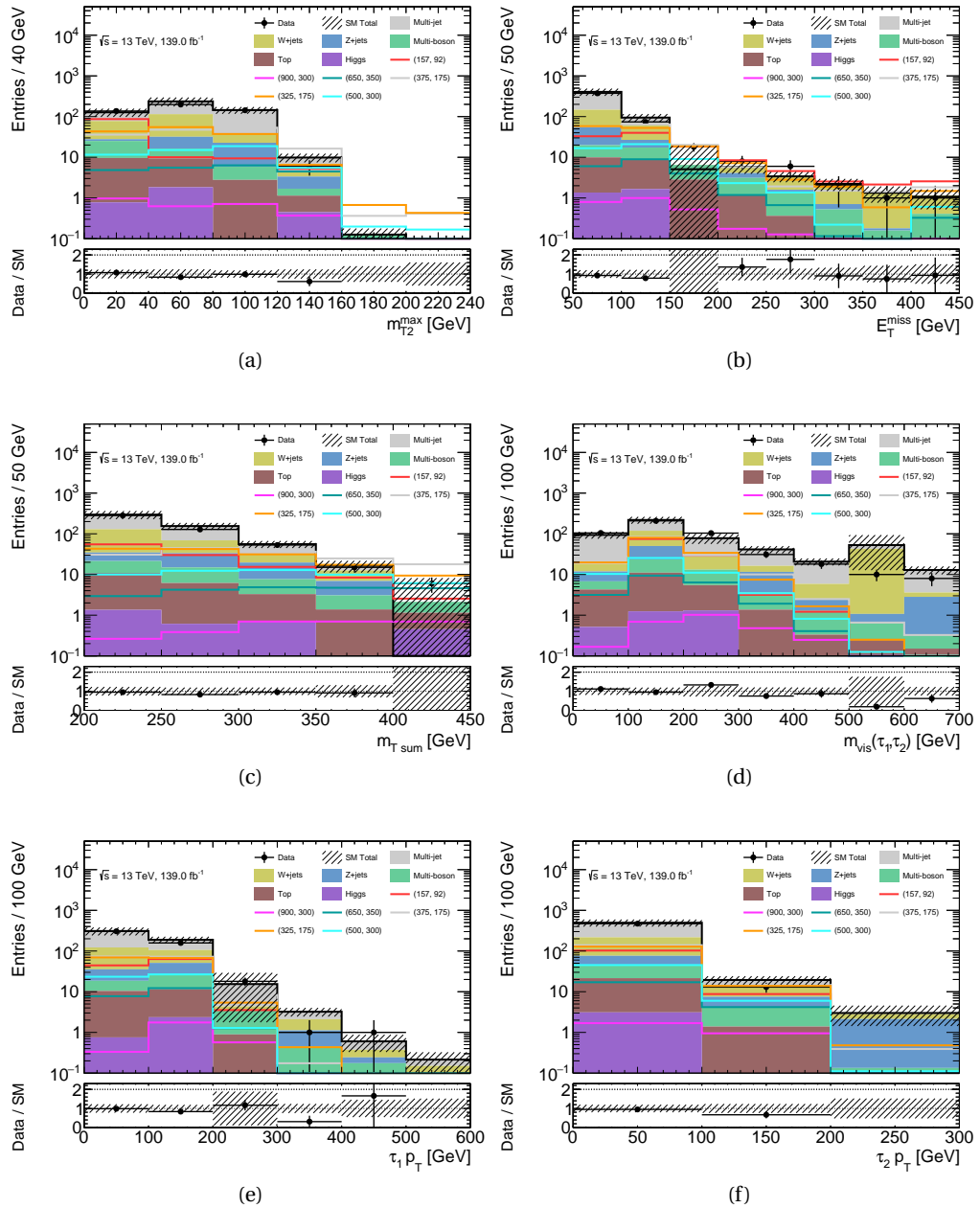


Figure 5.17: Data/MC distributions in VR-F-HM, the uncertainty band includes statistical and systematic uncertainties. No normalisation factors as extracted in the background-only fit described in section 5.12 are applied.

	Sample	CR-B	CR-C	VR-E	CR-A	T=C/B	multi-jet in VR-F	multi-jet in SR-C1N2SS
LM	Data	585	65	356	1505			
	Z+ jets	11.70 ± 2.11	25.92 ± 2.70	3.62 ± 1.06	32.85 ± 11.07	0.058	19.55 ± 1.13	0.94 ± 0.27
	W+ jets	4.84 ± 2.35	3.29 ± 0.96	11.48 ± 4.67	32.21 ± 10.06	±0.015		
	Multi-boson	0.80 ± 0.38	2.04 ± 0.35	1.20 ± 0.40	2.18 ± 0.50	±0.020		
	Top	2.54 ± 0.75	0.16 ± 0.27	2.45 ± 0.88	5.24 ± 0.93			
	Higgs	0.13 ± 0.04	0.73 ± 0.09	0.09 ± 0.05	0.53 ± 0.46			
	Multi-jet	564.98 ± 24.41	32.86 ± 8.57	337.16 ± 19.49	1431.98 ± 41.59			
HM	Data	2185	309	3651	14			
Z+ jets	30.81 ± 7.41	32.53 ± 10.81	56.12 ± 17.74	2.64 ± 1.37	0.086	283.10 ± 7.738	-0.086 ± 0.31	
W+ jets	178.87 ± 51.40	74.13 ± 15.33	248.68 ± 64.10	6.35 ± 2.58	±0.014			
Multi-boson	6.03 ± 0.87	18.35 ± 0.97	14.42 ± 1.44	0.83 ± 0.29	±0.011			
Top	20.73 ± 2.01	14.38 ± 1.53	39.23 ± 2.72	2.10 ± 0.57				
Higgs	0.53 ± 0.38	1.27 ± 0.58	0.71 ± 0.47	0.01 ± 0.00				
Multi-jet	1948.04 ± 69.90	168.34 ± 25.78	3291.83 ± 89.91	2.07 ± 4.79				

Table 5.6: Monte Carlo backgrounds in the ABCD regions of the signal regions defined in Table 5.3. The uncertainties given on the transfer factor are statistical followed by systematic uncertainties.

Sample	VRF-LM	VRF-HM
W+jets	1.35 ± 0.88	149.75 ± 42.98
Z+jets	9.30 ± 1.30	36.82 ± 19.62
top	0.99 ± 0.48	19.78 ± 1.85
Muliboson	1.47 ± 0.35	26.31 ± 1.2
Higgs	0.25 ± 0.06	3.16 ± 1.13
multi-jet	19.55 ± 1.13	283.10 ± 7.73
SM total	32.92 ± 2.02	518.92 ± 47.94
Data	40	484

Table 5.7: Event yields in VR-F-LM and VR-F-HM. Only statistical uncertainties are included in the multi-jet yield.

5.9.2 Estimation of W+jets background

The production of a W boson in association with a jet can enter a di-tau final state if one or more of the associated jets is misidentified as hadronic decaying tau lepton. The W+jets background contributes to both low and high mass signal regions, through moderate E_T^{miss} contributions of the neutrinos in the W bosons decay and mismeasured E_T^{miss} . A control and validation region targetting both signal regions is defined to estimate this background. A summary of the requirements applied to define the regions is given in Table 5.8. A final state with precisely one hadronically decaying tau lepton and one muon, both with the same electric charge, is selected to increase the available statistics. This final state targets to model events entering the signal regions with at least one fake tau, replacing the prompt tau through a prompt muon. A veto on baseline electrons is applied to target the muon plus hadronic tau final state. A veto on b-jets is used to constrain contributions from top related processes, whereas a cut on the transverse mass of the muon is used to remove Z+jets contaminations. A lower cut on the E_T^{miss} of 50 GeV is used to veto events with very close by muons and taus, which accumulate at low E_T^{miss} due to failed separation in overlap removal procedures. A cut on the m_{T2} variable, built with the muon and tau, is required to achieve similar event structures and phase spaces to the signal regions. This mimics the kinematic restrictions on the two leading taus used in the signal regions.

W-CR	W-VR
	pass TrigHLT_mu20_loose_L1MU15 (2015) and HLT_mu26_ivarmedium (2016-2018)
	== 1 medium tau and 1 isolated muon (SS)
	baseline electron veto
	b-veto
	$50 < m_T(\mu) < 150 \text{ GeV}$
	$m_T(\tau) + m_T(\mu) > 80 \text{ GeV}$
	$E_T^{\text{miss}} > 50 \text{ GeV}$
$m_{T2}(\mu, \tau) < 60 \text{ GeV}$	$m_{T2}(\mu, \tau) \geq 60 \text{ GeV}$

Table 5.8: Wjets control and validation region definition

With the cuts specified in Table 5.8, control and validation regions with high statistics are constructed, with a breakdown of the background yields, estimated purely from Monte Carlo simulation, which can be seen in table 5.9. The yield does not include systematic uncertainties. Both control and validation region show a high purity in W+jets processes, above 80% in both cases, as shown in figure 5.18. The signal contamination in both regions is negligible(see Fig. 5.19). Kinematic distributions in the W-CR and W-VR are shown in Figure 5.20 and 5.21, respectively.

Sample	W-CR	W-VR
W+jets	21005.90 ± 880.74	5852.23 ± 502.55
Z+jets	2529.68 ± 205.40	737.16 ± 90.34
top	1148.86 ± 12.66	185.39 ± 5.18
Multiboson	629.41 ± 8.79	122.50 ± 3.62
Higgs	20.70 ± 3.31	5.49 ± 1.72
Multi-jet	0.00 ± 0.00	0.00 ± 0.00
SM total	25334.55 ± 904.51	6902.76 ± 510.65
Data	25728	6662

Table 5.9: Event yields in W+jets Control and Validation region. The shown uncertainties for SM backgrounds are the statistical uncertainties only.

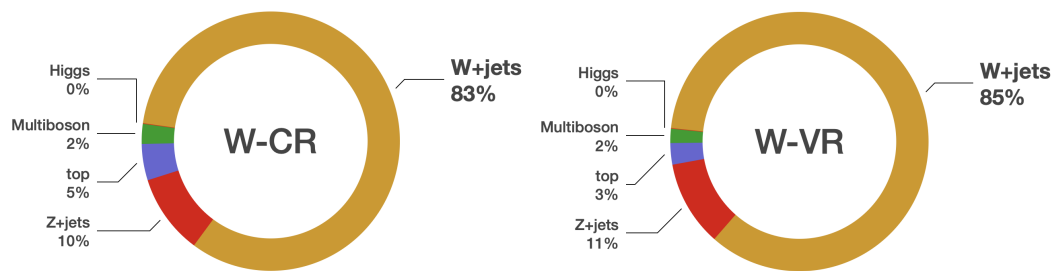


Figure 5.18: Background composition in W+jet Control and Validation region

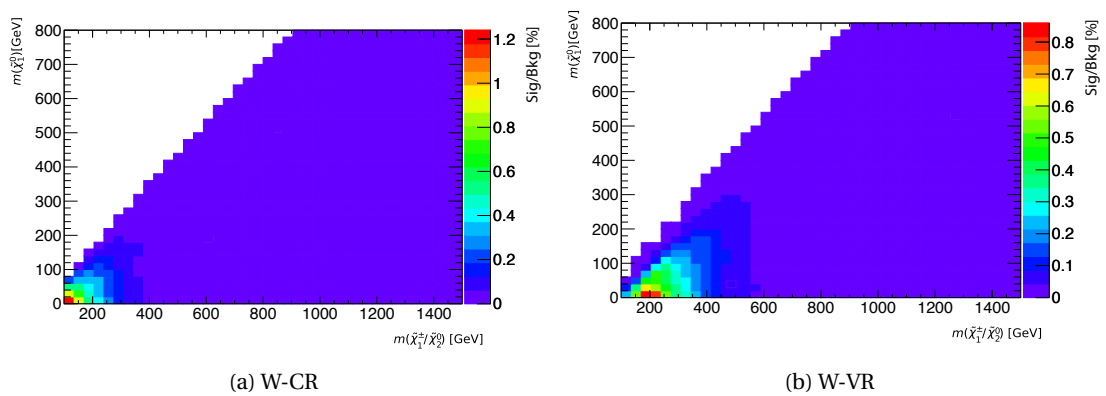


Figure 5.19: Signal contamination in percentage in W-CR and W-VR.

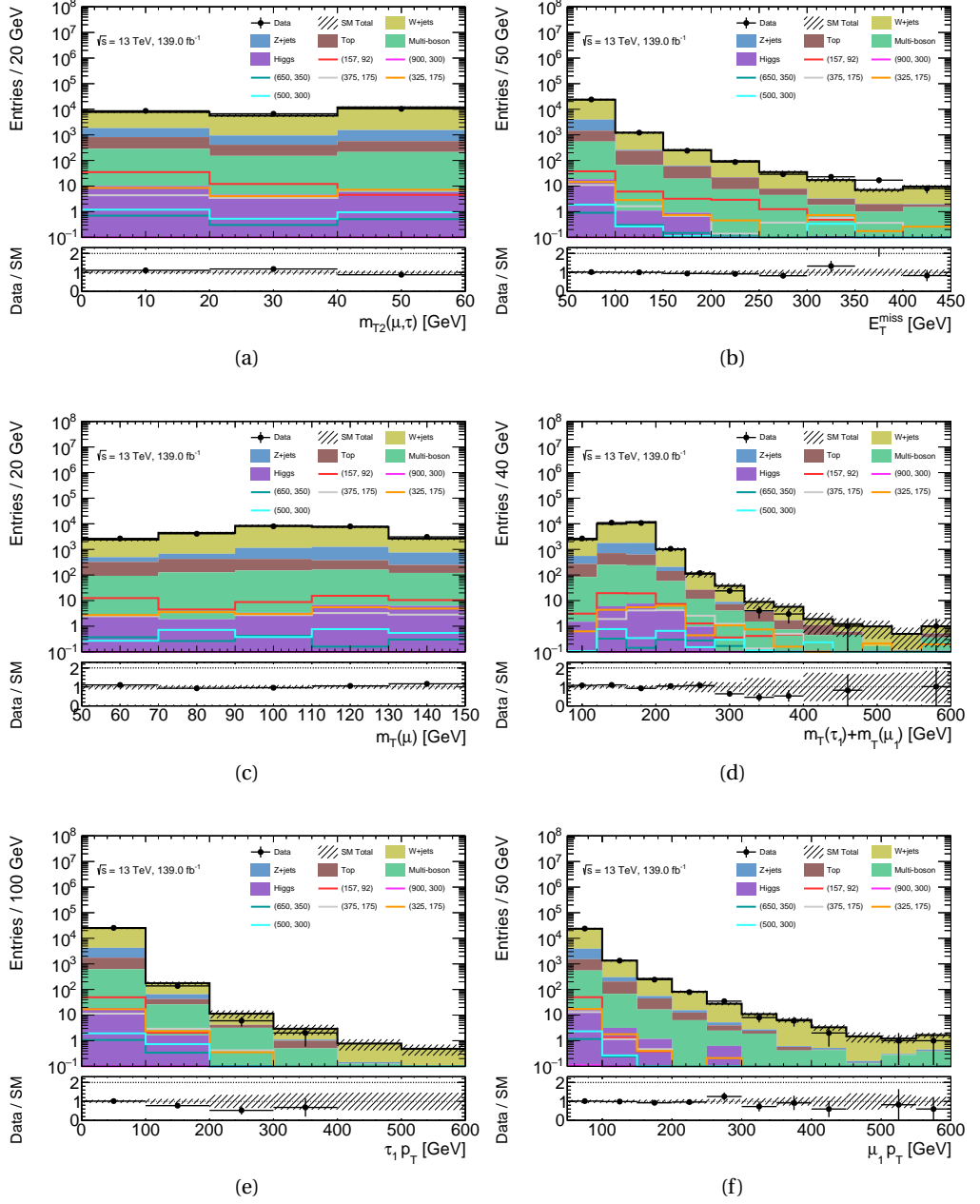


Figure 5.20: Distributions of relevant kinematic variables in the W -CR. The SM backgrounds other than multi-jet production are estimated from MC simulation and normalised to 139 fb^{-1} . The hatched bands represent the statistical uncertainties and systematic uncertainties discussed in 5.10. The lower panel shows the ratio of data to the SM background estimate. No normalisation factors as extracted in the background-only fit described in section 5.12 are applied.

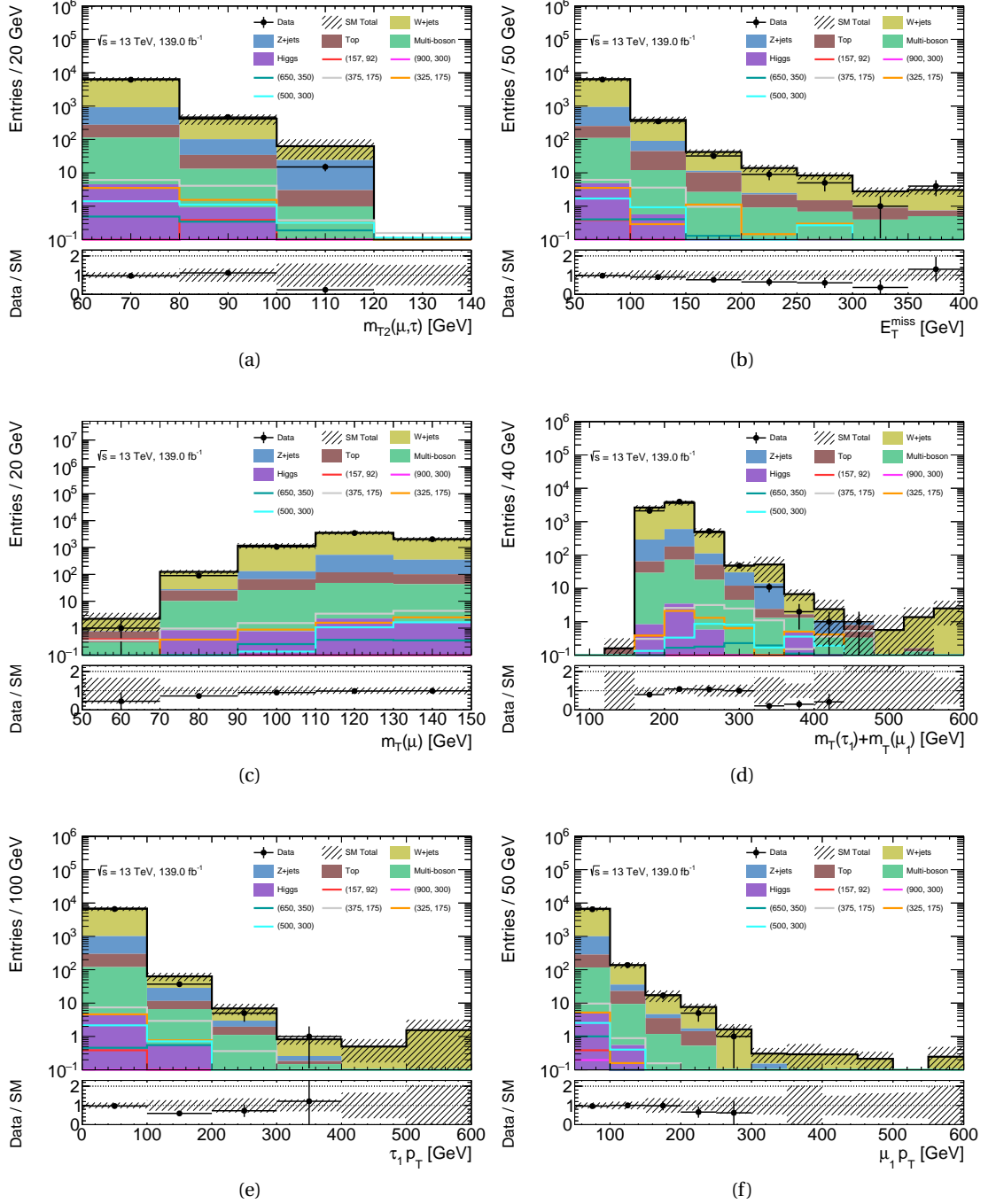


Figure 5.21: Distributions of relevant kinematic variables in the W -VR. The SM backgrounds other than multi-jet production are estimated from MC simulation and normalised to 139 fb^{-1} . The hatched bands represent the statistical uncertainties and systematic uncertainties discussed in 5.10. The lower panel shows the ratio of data to the SM background estimate. No normalisation factors as extracted in the background-only fit described in section 5.12 are applied.

5.9.3 Top background estimation

Top-related processes are a dominant background contribution, especially in SR-C1N2SS-HM (with around 35% of the overall background expectation, as given in 5.4). To estimate this background, a data-driven approach is used in the high mass scenario, using a control region (TCR-HM) to extract a normalisation factor. This is validated in a high mass Top validation region (TVR-HM). The kinematic cuts used to define these regions can be seen in table 5.10, where the tau identification working point has been lowered to increase the available statistics. A lower E_T^{miss} requirement is applied to reduce the contribution of multi-jet processes.

TCR-HM	TVR-HM
$n_{\text{at least very loose taus}} \geq 2$ $n_{\text{at least loose taus}} \geq 1$ $n_{\text{medium taus}} < 2$ $n_{B\text{Jets}} \geq 1$	
di-tau plus met trigger $E_T^{\text{miss}} \geq 150 \text{ GeV}$ $m_{T\text{sum}} \leq 400 \text{ GeV}$ $m_{T\text{sum}} \geq 400 \text{ GeV}$	

Table 5.10: Definition of Top Validation and Control regions

An overview of the event yields is shown in Table 5.11, with a visualisation of the background contributions in the validation and control regions in Figure 5.22.

Sample	TCR-HM	TVR-HM
W +jets	13.23 ± 1.74	1.06 ± 0.31
Z + jets	4.31 ± 0.90	0.81 ± 0.43
top	104.49 ± 4.04	16.97 ± 1.58
Multiboson	3.13 ± 0.92	0.22 ± 0.08
Higgs	0.98 ± 0.04	0.13 ± 0.01
multi-jet	0.00 ± 0.00	0.00 ± 0.00
SM total	126.13 ± 4.58	19.20 ± 1.66
Data	96	12

Table 5.11: Event yields of TCR-HM, TVR-HM . All uncertainties are statistical only.

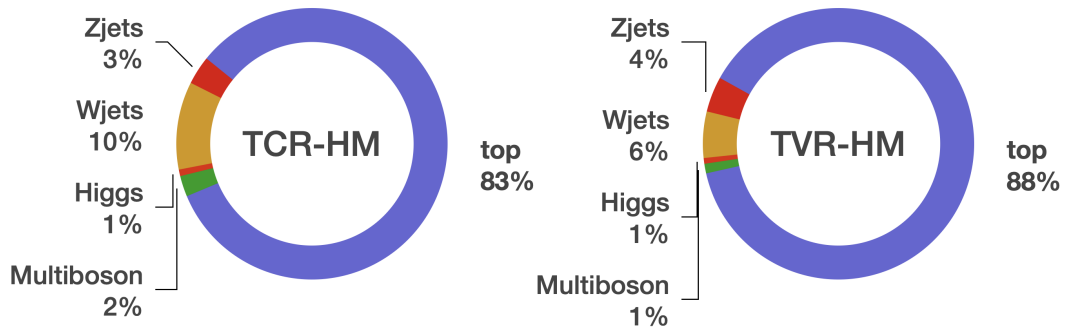


Figure 5.22: Process composition in Top Control and Validations

An overview of the signal contamination in percentage points in the top validation and control regions is shown in 5.23. The signal points with high contamination have been already

excluded in a previous publication, using opposite-sign tau final states discussed in [99].

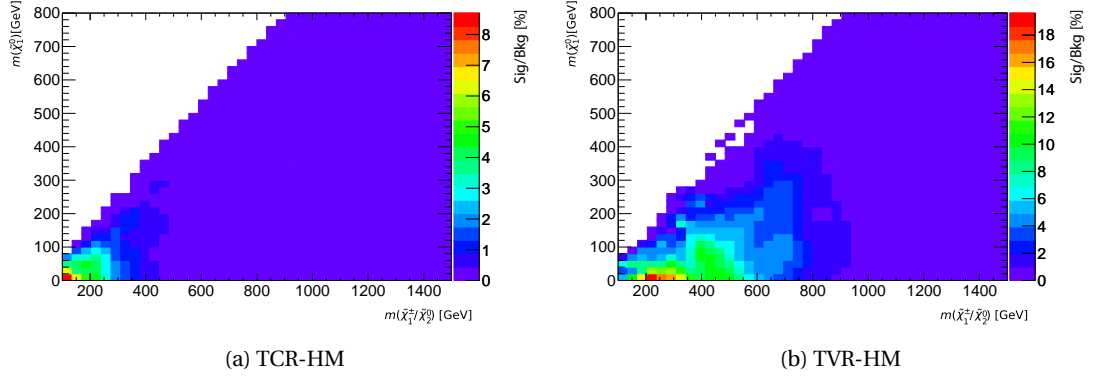


Figure 5.23: Signal contamination of high mass Top CR and VR in percent

A downward trend in the data with respect to Monte Carlo simulation can be observed in some variables in Figure 5.24 and 5.25 of the T-CR and T-VR, most dominantly in Figure 5.24e, showing the $m_T(\tau_1) + m_T(\tau_2)$ distribution in the high mass top control region. This shift in the Monte Carlo simulation agreement is due to a changing composition of the top contributions. Towards higher transverse masses, a slight increase in events with at least two fake taus can be observed. Fake taus are poorly modelled in Monte Carlo and are leading to an overestimation of the Monte Carlo with respect to data. This trend is broken down in Figure 5.26, showing an inclusive $m_T(\tau_1) + m_T(\tau_2)$ distribution, with all requirements from Table 5.10, except the $m_T(\tau_1) + m_T(\tau_2)$ cut separating the control and validation regions. The analysis decomposing the top contribution based on the number of fake, non-prompt tau leptons is done using truth information of the Monte Carlo generators, providing information of the generated process before detector simulation. As can be seen, the previous observed downward trends in data can be related to an increase in the top contribution with at least two fake taus. The cut in $m_T(\tau_1) + m_T(\tau_2)$ separating the control and validation region at 400 GeV has been chosen to enhance the two fake tau composition in the control region, while still retaining enough background statistics in the validation region. A breakdown of the top background composition in the high mass signal region as well as T-CR and T-VR is given in Table 5.12.

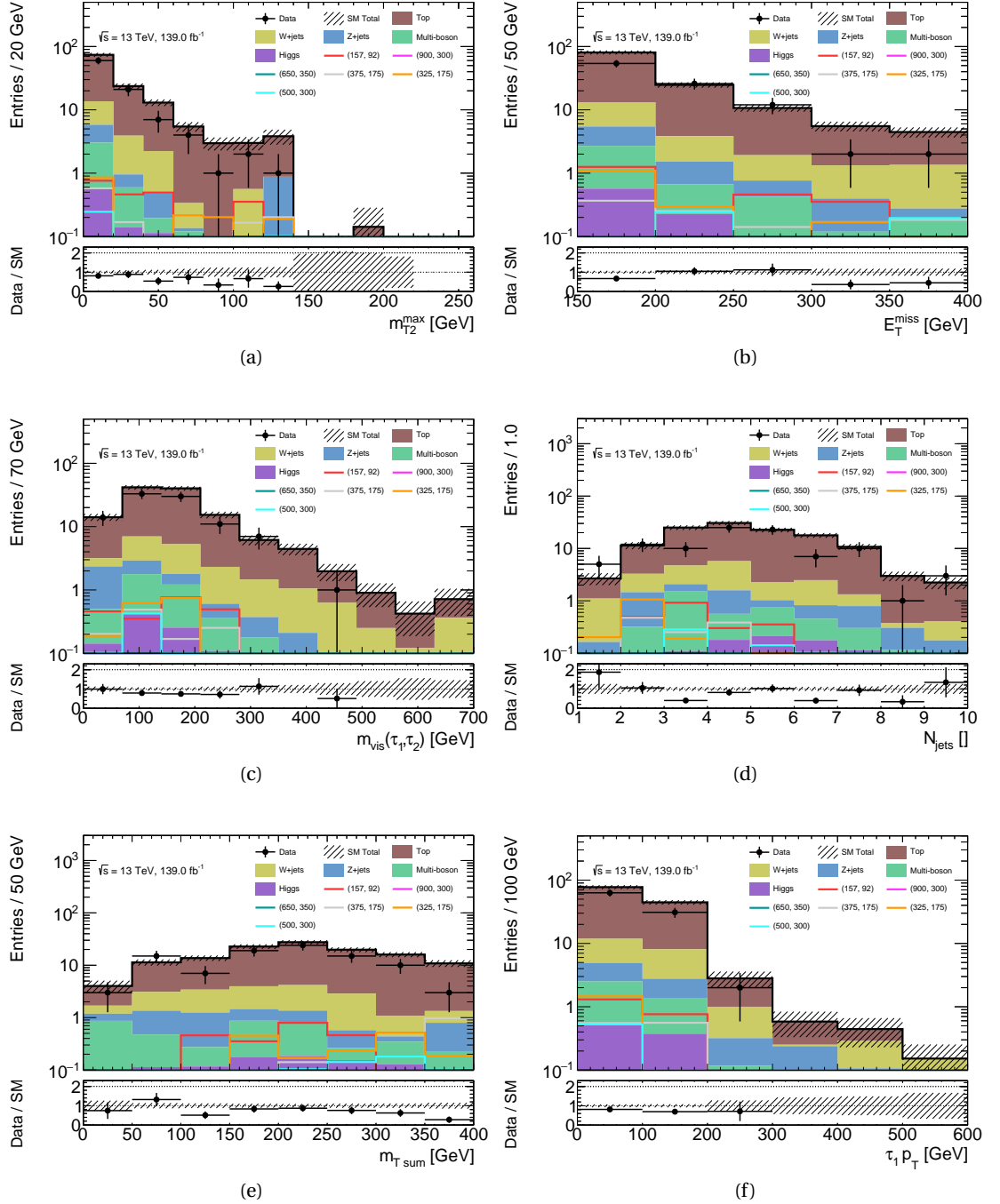


Figure 5.24: Top High mass control region data/MC distributions. The hatched band is including the statistical and systematic uncertainties. No normalisation factors as extracted in the background-only fit described in section 5.12 are applied.

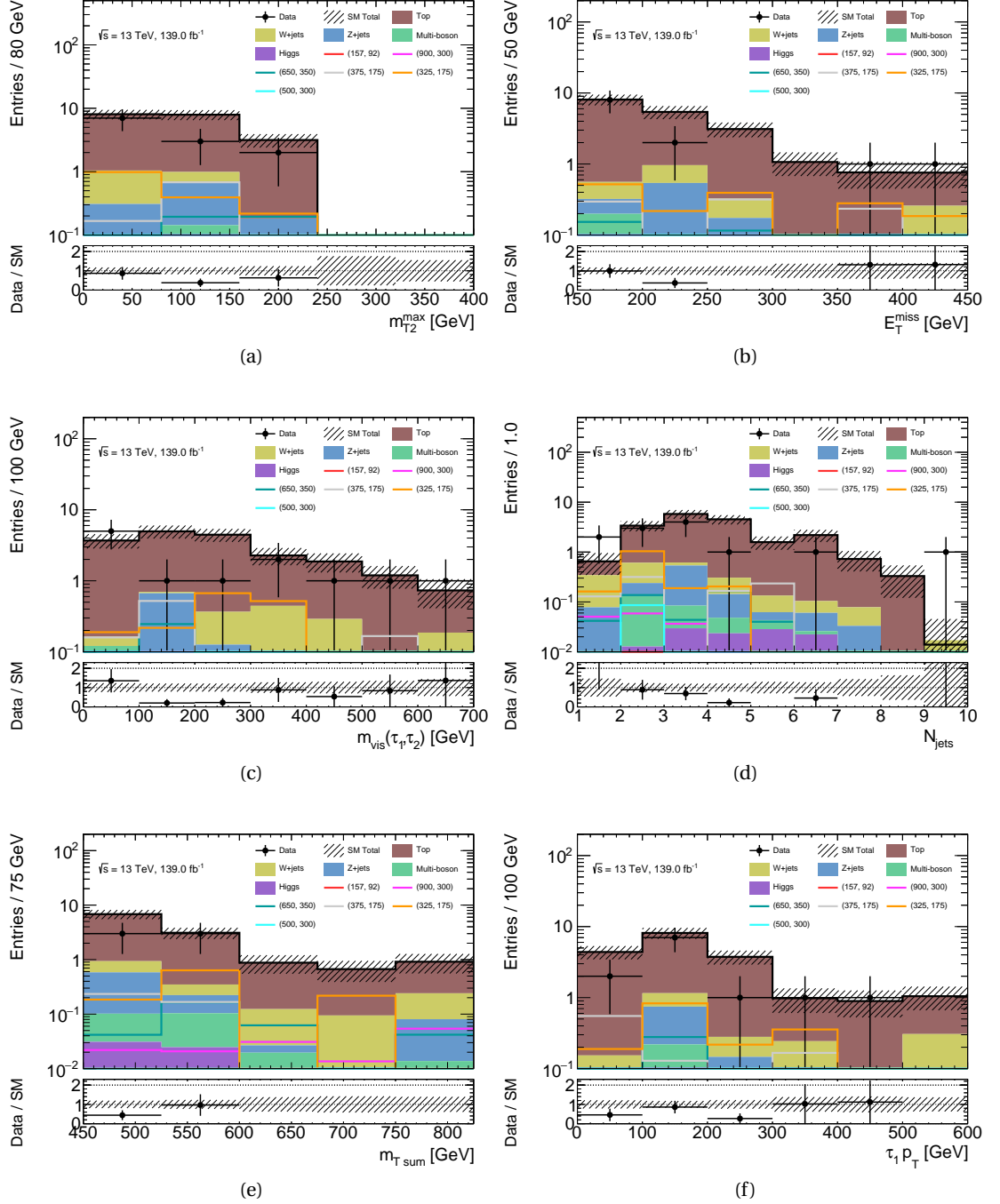


Figure 5.25: Top High mass validation region data/MC distributions. The hatched band is including the statistical and systematic uncertainty. No normalisation factors as extracted in the background-only fit described in section 5.12 are applied.

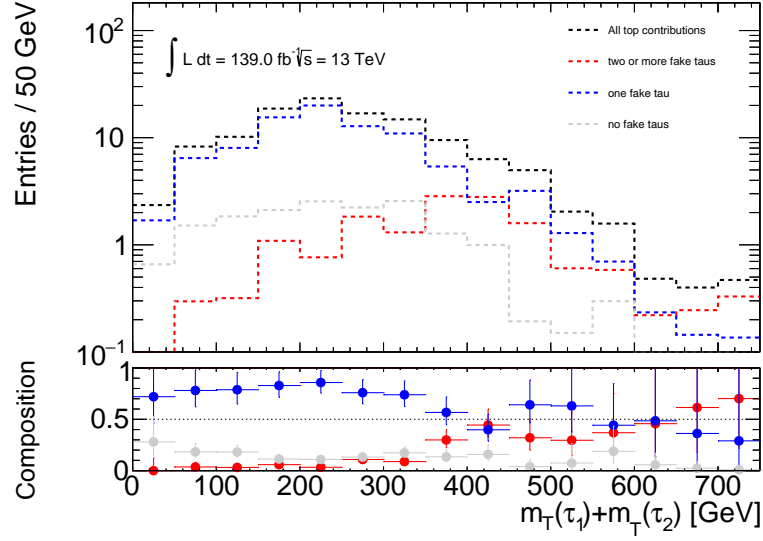


Figure 5.26: Breakdown of the top compositions in the top control and validation region

	SR-HM	TCR-HM	TVR-HM
all Top	0.84 ± 0.36	104.49 ± 4.04	16.97 ± 1.58
=0 fakes	0.028 ± 0.014	14.89 ± 1.49	1.71 ± 0.47
=1 fake	0.49 ± 0.28	81.14 ± 3.58	8.87 ± 1.15
>=2 fakes	0.319 ± 0.23	8.46 ± 1.12	6.39 ± 0.98
ttbar	0.61 ± 0.31	91.00 ± 3.71	15.67 ± 1.53
=0 fakes	–	11.80 ± 1.31	1.52 ± 0.47
=1 fake	0.30 ± 0.21	71.69 ± 3.31	8.20 ± 1.11
>=2 fakes	0.319 ± 0.23	7.51 ± 1.04	5.95 ± 0.95
singletopWt	0.19 ± 0.19	10.18 ± 1.56	0.56 ± 0.29
ttV	0.034 ± 0.016	1.98 ± 0.17	0.41 ± 0.076
tZ	–	0.27 ± 0.060	0.014 ± 0.027
singletopTchan	–	0.83 ± 0.31	0.28 ± 0.20

Table 5.12: Breakdown of top background contributions in the high mass regions by top processes and number of fake taus. Uncertainties included are statistical only.

5.9.4 Multi-boson background estimation

Multi-boson processes are one of the leading contributions to SR-C1N2SS-HM (as in 5.3). A validation region was designed to validate the modelling of these background processes from Monte Carlo simulation. To target the WZ and WW processes dominating the multi-boson contribution in the signal regions, a selection of an opposite-sign muon pair and a hadronically decaying tau was used. This has been selected to target the contribution from real tau leptons, dominating this background process, and estimate it through replacing real tau leptons with light leptons. As shown in Table 5.13, a b-jet veto is used to suppress top-quark related backgrounds, an upper bound of $\Delta\phi(\tau, E_T^{\text{miss}}) \leq 1.75$ is used to restrict the number of Z+jets events populating the multi-boson validation region. A summary of yields in the MBVR-SS is shown in Table 5.14.

An overview of the background composition and multiboson purity, as well as the signal con-

MBVR-SS
Two OS signal muons == 1 signal tau b-Jet Veto $E_T^{\text{miss}} \geq 100\text{GeV}$ $\Delta\Phi(\tau, E_T^{\text{miss}}) \leq 1.75$

Table 5.13: MBVR-SS definition

Sample	MBVR-SS
Multiboson	144.22 ± 1.96
Top	33.30 ± 2.13
Zjets	16.44 ± 29.32
Higgs	4.30 ± 1.26
Wjets	0.08 ± 0.08
Total Bkg	198.32 ± 29.49
Data	200
(325, 175)	0.29 ± 0.22
(375, 175)	1.07 ± 0.39

Table 5.14: Yields in MBVR . All uncertainties are statistical only.

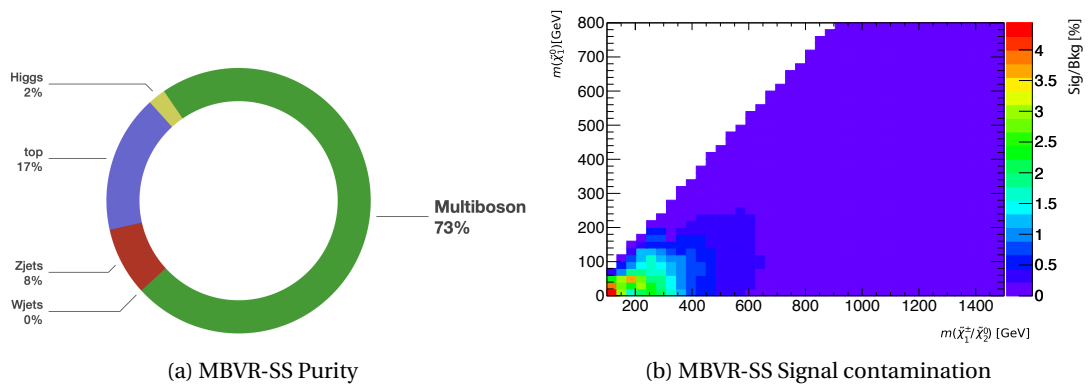


Figure 5.27: Multiboson purity in MBVR-SS as well as signal contamination in %

tamination in the region, is given in Figure 5.27. A few selected kinematic variable distributions are given in Figure 5.28, showing good agreement between the SM expectation and data.

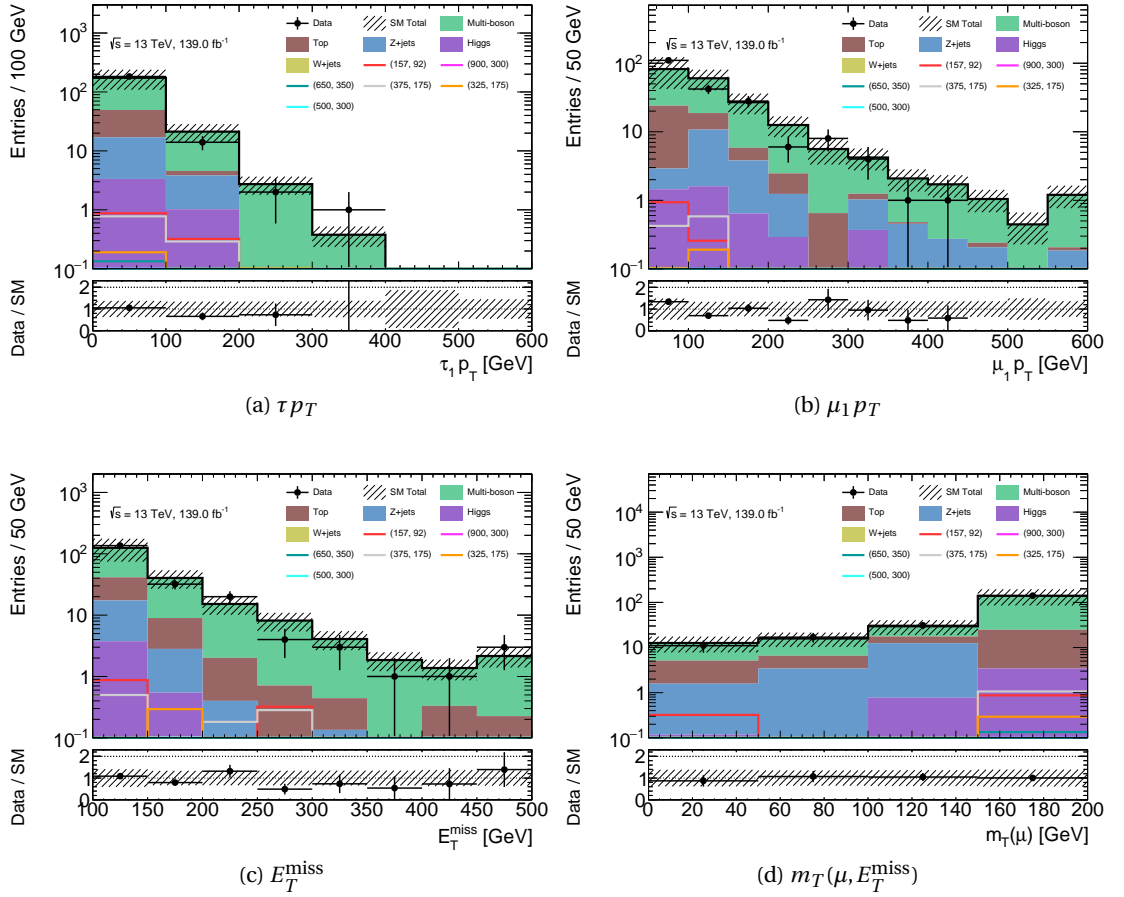


Figure 5.28: Kinematic distributions comparing data/MC in the Multiboson validation region. The hatched uncertainty band includes statistical and systematic uncertainties. No normalisation factors as extracted in the background-only fit described in section 5.12 are applied.

5.9.5 Z+jets and Higgs processes

Similarly to W+jets processes, Z+jets and Higgs SM processes can end up in a final state with at least two hadronically decaying taus. Here Higgs productions and di-Higgs productions can produce two prompt taus. Due to the low associated cross-section, both the Z+jets and Higgs processes contribute a small part to the signal regions. The estimation of both of these rely on Monte Carlo simulation. No dedicated validation region has been designed. Its modelling can sufficiently be validated through its presence in the Multi-jet, top, W+jets and Multi-boson validation and control regions.

As can be seen in the agreement with Monte Carlo simulation and data in figures 5.21, 5.25 and 5.28, no significant contribution from any other backgrounds, especially Multi-jet backgrounds is expected. Due to its QCD interactions, multi-jet backgrounds are not expected to prefer same-sign and opposite-sign final states. Therefore, they are expected to populate an opposite-sign tau final state in an equal manner to a same-sign tau final state. In opposite-sign regions, a large negative contribution of multi-jet has been observed, further confirming that there is no contribution of the multi-jet background not already accounted for by Monte Carlo simulation

that needs to be taken into account in the non-multi-jet control or validation regions.

5.10 Systematic uncertainties

5.10.1 Experimental uncertainties

To construct a complete statistical model of the analysis (see section 5.11), all sources of uncertainties influencing the background and signal compositions have to be included. In the following, a description of the *experimental* uncertainties is given. Here referred to as experimental uncertainties are uncertainties related to all steps in the data collection, from uncertainties on the collected luminosity to object reconstruction and identification uncertainties.

Tau reconstruction The reconstruction and identification of tau leptons is associated with systematic uncertainties [76]. Considered here are systematic uncertainties connected with the RNN based differentiation between jets and hadronic taus. Additionally tau reconstruction efficiency uncertainties, uncertainties on the tau energy scale and systematics in the BDT used to distinguish taus from electrons are included.

Light lepton reconstruction A simplified model considering uncorrelated uncertainties for the electron energy calibration (scale and resolution) is assumed [92]. Uncertainties related to the efficiency estimation of the electron and muon reconstruction, identification and isolation are included in the analysis. For muons, additional uncertainties take into account variations of the muon momentum scale as well as uncertainties in the track-to-vertex association [70].

Jet reconstruction Uncertainties on the jet energy scale are taken into account through a reduced set [129], additionally uncertainties on the jet energy resolution are included. Scale Factors and their uncertainty correcting the efficiency performance of the DL1 b-tagging in Monte Carlo have been taken into account.

E_T^{miss} reconstruction Systematic uncertainties of the E_T^{miss} reconstruction include uncertainties on the scale and resolution of the track soft term. This is extracted through comparisons of data and simulation as well as Monte Carlo generator comparisons [77].

Event based uncertainties A $\pm 1.7\%$ uncertainty on the measured luminosity is taken into account [130], next to variations in the applied pileup reweighting and uncertainties on trigger scale factors for Monte Carlo Simulation.

5.10.2 Theoretical and Modelling uncertainties

The experimental uncertainties described above affect the reconstructed objects and, as a consequence, the observed yields in data as well as simulation. Additionally, uncertainties connected to Monte Carlo simulation have to be taken into account. These uncertainties can be es-

timated by varying the parameters in the Monte Carlo simulation, affecting all aspect of Monte Carlo event generation. The evaluation of these uncertainties is described in the following for the main **SM** backgrounds as well as **SUSY** signal.

Top related backgrounds Hard scattering and parton showering uncertainties have been extracted based on generator comparisons. This has been evaluated separately for $t\bar{t}$ as well as single top Wt contributions. To avoid large uncertainties solely due to limited statistics available in the truth-level generator comparisons a loosened selection has been used. The nominal generator used to simulate $t\bar{t}$ events is a combination of POWHEG for the **NLO** matrix element generation, interfaced to PYTHIA for parton showering. A hard scattering, matrix element related uncertainty is calculated through a comparison of truth-level Powheg Pythia 8 samples with MadGraph5_aMC@NLO and PYTHIA. A variation in parton showering is achieved by replacing the PYTHIA shower through Herwig7. The systematic uncertainty associated to these variations in regions i is given by equation 5.9.

$$\sigma^i = \frac{N_{nom}^i - N_{var}^i}{N_{nom}^i} \quad (5.9)$$

An additional weight has been introduced into the simulation to estimate the effect of a change in Parton Distribution Function (**PDF**) on the acceptance of the analysis. An uncertainty related to the PDF variation has been calculated according to the PDF4LHC recommendations [131]. A similar weight has been included to estimate effects on Initial State Radiation (**ISR**) and Final State Radiation (**FSR**) in for example showering or scale differences. An uncertainty is extracted based on these internal reweighting of the Monte Carlo sample. An uncertainty accounting for individual variations in the factorisation and renormalisation scale is included. Additionally, a joint variation is taken into account.

Multi-boson backgrounds The **PDF** as well as factorisation and renormalisation related uncertainties are estimated as described for the top backgrounds. Additionally for the Multi-boson backgrounds, uncertainties related to the matching between matrix element and parton showering as well as the resummation scale has to be taken into account. Another part in the Monte Carlo event generation that can lead to different predicted event kinematics is the parton shower recoil scheme used. All of these possible variations in the Monte Carlo event generation are taken into account through an uncertainty, which is extracted by comparing truth-level simulations with adapted Monte Carlo parameters. Multi-boson processes are not normalised in control regions in the analysis described, therefore an additional uncertainty on the inclusive cross section of 20% is included, following recommendations of the ATLAS Multi-boson focus group.

V+jets backgrounds Vector boson production in association with jets is simulated using *Sherpa* within this thesis. Internal weight variations are used to assign an uncertainty accounting for the renormalisation, factorisation as well as PDF variations. For the considered *Sherpa*

samples, a parametrised approach is used to estimate uncertainties related to the resummation and matching scales. This parametrised approach is based on previous generator comparisons. For Z boson production with associated jets an additional uncertainty on the inclusive cross section of 5% is included, following recommendation from the ATLAS Boson and Jets focus group.

Higgs related backgrounds Uncertainties on the modelling of Higgs boson related processes are included for scale variations as well as PDF variations. Similar to top related processes, uncertainties connected to [ISR](#) and [FSR](#) are included. Within the regions of the same-sign di-tau analysis, Higgs related backgrounds are predominantly the production of a top pair in association with a Higgs. Following inclusive cross section uncertainty studies performed in [\[116\]](#), an additional 15% uncertainty is assigned to the Higgs background modelling.

Signal cross section uncertainties For the simplified signal model, similar modelling uncertainties due to the Monte Carlo generator configurations have to be taken into account. One uncertainty is defined for a joint variation of the renormalisation and factorisation scale, a second joint uncertainty considering the matching and merging scale. Lastly, a radiation uncertainty is taken into account. The uncertainties are extracted through comparisons to dedicated varied truth-level samples. The uncertainty based on these variations have been evaluated for every mass point separately. Due to limited available statistics in the truth samples, loosened kinematic selections have been used. To avoid further statistical fluctuations related to the limited statistics, an envelope of multiple averages over close-by mass points have been performed. An uncertainty of $\pm 1.5\%$ will be considered as the joint renormalization and factorisation scale uncertainty. The merging scale variations are largely asymmetric, with its downward variation leading to very large uncertainties. To mitigate this, an averaged value of the upward fluctuation will be used, leading to a $\pm 7.0\%$ merging scale uncertainty. A conservative 3.5% will be used for the radiation uncertainty.

An overview of the theoretical uncertainty values is given in [appendix A.1](#).

5.11 Statistical concepts

All regions defined in the analysis as described in [section 5.7](#), [5.8](#) and [5.9](#) are combined into a joint likelihood. In general, a likelihood $L(\theta)$ is the probability of the outcome of an experiment with measured value x , given a model with parameter θ (see [\(5.10\)](#)).

$$L(\theta) = P(x|\theta) \tag{5.10}$$

In the case of this analysis, the measurement is that of the data events in all kinematic phase space regions defined, in the following denoted as n . The regions are defined in orthogonal phase spaces and are therefore statistically independent. As is given and discussed for example in reference [\[132\]](#), the probability of independent measurements is given through the product

of their probabilities. The probability density function of a number of data events in region i , n_i is given through a Poisson distribution (λ_i) in dependency of the free parameters, $\boldsymbol{\theta}$, the signal and background expectation s, \mathbf{b} , as well as normalisation factors for signal and backgrounds ($\mu_{SIG}, \boldsymbol{\mu}$). This would lead to a likelihood function, (5.11), with free model parameters $\boldsymbol{\theta}$.

$$L(\mathbf{n}|\boldsymbol{\theta}, s, \mathbf{b}, \mu_{SIG}, \boldsymbol{\mu}) = \prod_{i \in \text{regions}} P(n_i | \lambda_i(\mu_{SIG}, \boldsymbol{\mu}, s, \mathbf{b}, \boldsymbol{\theta})) \quad (5.11)$$

The free model parameters $\boldsymbol{\theta}$ include all systematic as well as statistical uncertainties since they can vary the signal and background expectation. In the likelihood given in (5.11), these uncertainties are free parameters in the background and signal modelling, in the following also called *nuisance parameters*.

The vector $\boldsymbol{\mu}$ in the likelihood includes all normalisation factors for all normalised backgrounds. The definition of a normalisation factor μ_p for a SM background process p and its connection to the background estimated in the signal region ($N_p(SR)$) is shown in equation (5.12), in dependence on the Monte Carlo expectation in the control and signal region ($MC_p(CR)$ and $MC_p(SR)$, respectively).

$$\begin{aligned} N_p(CR) &= \mu_p \times MC_p(CR) \\ N_p(SR) &= \mu_p \times MC_p(SR) \end{aligned} \quad (5.12)$$

This is how the normalisation factor is included in the likelihood, the same factor simultaneously applied in all regions to scale a background contribution. Since the control regions are designed to be pure in the specific background, these regions will define the normalisation factor. An alternative formulation of the normalised background contribution through a transfer factor, extrapolating the background estimation from a control region to the signal region is shown in (5.13) (adapted from [133]).

$$\begin{aligned} N_p(SR) &= N_p(CR) \times TF_p \\ TF_p &= \frac{MC_p(SR)}{MC_p(CR)} \end{aligned} \quad (5.13)$$

This interpretation of the connection between control region and signal region yields is particularly helpful in connection with systematic uncertainties. Due to the ratios of Monte Carlo expectations, some systematic uncertainties can be partially cancelled in the extrapolation from the control to the signal region.

In the reality of the experiment conducted here, the uncertainties of the model are constrained through auxiliary measurements. The experimental and theoretical uncertainties have a measured value θ^0 , but also these uncertainty parameters follow an underlying statistical model. To constrain the free parameters $\boldsymbol{\theta}$, they are assumed to follow a Gaussian distribution around the central values $\boldsymbol{\theta}^0$. All auxiliary measurements are assumed to be statistically independent,

leading to a product of Gaussian distributions of all $\boldsymbol{\theta}$ components. This additional term is becoming part of the likelihood (adapted from [133]):

$$L(\mathbf{n}, \boldsymbol{\theta}^0 | \boldsymbol{\theta}, s, \mathbf{b}, \mu_{sig}, \boldsymbol{\mu}) = \prod_{i \in \text{regions}} P(n_i | \lambda_i(\mu_{sig}, \boldsymbol{\mu}, s, \mathbf{b}, \boldsymbol{\theta})) \times \prod_{j \in \text{systematics}} G(\boldsymbol{\theta}_j^0 - \boldsymbol{\theta}_j) \quad (5.14)$$

The likelihood described above can give a probabilistic model of the observed events given specific values of the model parameters. An important quantity needed to gauge the agreement of the model with different hypotheses is the test statistic. Within the analysis and inherent measurement described here, a profile likelihood test statistic is used as given in equation (5.15) (from [133]) and discussed in detail in [134].

$$q_{\mu_{sig}} = -2 \log \left(\frac{L(\mu_{sig}, \hat{\boldsymbol{\theta}})}{L(\hat{\mu}_{sig}, \hat{\boldsymbol{\theta}})} \right) \quad (5.15)$$

The numerator $L(\mu_{sig}, \hat{\boldsymbol{\theta}})$ shows the likelihood as defined in equation (5.14) with parameters $\hat{\boldsymbol{\theta}}$ maximising the likelihood for the fixed choice of μ_{sig} . In the denominator likelihood, $L(\hat{\mu}_{sig}, \hat{\boldsymbol{\theta}})$, both μ_{sig} and $\boldsymbol{\theta}$ are chosen to jointly maximise the likelihood. Assuming the case of high enough statistic, the distribution of this test statistic follows a χ^2 distribution. Within this thesis, this limit has been assumed, but validated through toy experiments, sampling the test statistic distribution.

Two hypotheses are of importance for a search for new physics described here. A *background-only* hypothesis, assuming that there is no **BSM** signal present and only contributions from the **SM** have to be taken into consideration. In contrast to this, a *background plus signal* hypothesis, assuming a **BSM** signal is present in addition to the **SM** prediction. Once a distribution of the test statistic is evaluated for these two hypotheses (fixing the assumptions on μ_{SIG}), p-values and composite expression of p-values are used to make statements of the statistical likelihood of the observation or a more extreme outcome to agree with one or the other hypothesis. A possible definition of the p-value with respect to the test statistic $q_{\mu_{sig}}$ defined in equation (5.15) is the following (adapted from [135]):

$$p_{\mu} = \int_{q_{\mu, obs}}^{\infty} f(q_{\mu_{sig}} | \mu_{sig}) dq_{\mu_{sig}} \quad (5.16)$$

A one-sided p-value is an integral of a probability density function from the observed value to the end of the distribution. In particle physics this is often displayed through a significance measure, Z (see equation (5.17), from [134]). This uses the Quantile (Φ) of a Gaussian distribution to transform the p-value into a measure of Z standard deviations of a Gaussian distribution away from the central value.

$$Z = \Phi^{-1}(1 - p) \quad (5.17)$$

To quantify whether an observation is in agreement with the *signal plus background* hypothesis in comparison with the *background-only* hypothesis, the CL_s value is used as defined in equation (5.18) [135].

$$CL_s = \frac{CL_{s+b}}{CL_b} \quad (5.18)$$

$$1 - CL_s \leq CL \quad (5.19)$$

With CL_{s+b} and CL_b representing the p-value of the signal plus background and background-only test-statistic, respectively. Even though the CL_s is not strictly a confidence level, it can be interpreted as such. In the following, a confidence level of 95% is associated with a CL_s value below 0.05, according to equation (5.19).

5.11.1 Fit strategies

As hinted in relation to equation (5.15), a maximisation of the likelihood for different choices of μ_{sig} is performed to evaluate the test statistic. Larger values of the test statistic for the background-only hypothesis (SM contribution only, $\mu_{SIG} = 0$) or background plus signal hypothesis (SM plus SUSY signal, $\mu_{SIG} = 1$) indicate better agreement with the respective hypothesis. In general, three strategies of a fit of the likelihood are used within the ATLAS BSM community and followed in this thesis:

Background-only fit A so-called *background-only* fit is aiming to extract a background estimate with normalisation factors and extrapolate the estimate to the signal and validation regions. This is done using a maximum likelihood estimation [132] of the normalisation parameters as free parameters and is performed in the control regions only. The parameters can then be applied to a fixed likelihood including the validation regions. Once the background predictions have been validated, the likelihood can be further expanded to include the signal regions. No contribution from signal processes is taken into account, neglecting any signal contamination in the control regions.

Model-independent fit In the case of a *model-independent* fit, the background estimation of the background-only fit is compared with a generic signal expectation. No model-dependent signal expectation is included, but an upper limit on the signal yield contributing to the signal regions is extracted by including a dummy signal in the signal regions only. No signal contamination in the control regions is assumed. This fit aims to evaluate the agreement with the background-only fit and extract an upper limit on the cross-section of a potential signal contribution that is not specifically investigated through the model in this thesis.

Model-dependent fit When including the signal expectation in a so-called *model-dependent* fit, the signal and control regions are used simultaneously. Under the signal-plus-background

hypothesis, a normalisation factor for the signal expectation as well as for the backgrounds is extracted simultaneously. If the CL_s value for a specific signal point falls below 0.05 (95 % confidence level), this signal point is excluded.

Within all performed fit strategies, a total error on the background estimation is extracted, based on the normalisation factors and nuisance parameters in the fit. The overall background error is following error propagation and includes a term with a correlation coefficient between different nuisance parameters and normalisations. This correlation can lead to larger or smaller overall errors than the uncorrelated squared sum of the single uncertainty errors would. All fits are performed using the HISTFITTER software framework [133], with dependencies to HistFactory [136].

5.12 Results

To test the background-only hypothesis versus the signal plus background hypothesis, a complete statistical model in the form of a likelihood is used. This likelihood as given in equation (5.14) is simultaneously fitted in all control regions to extract normalisation factors on the backgrounds defined through control regions. The result of the simultaneous likelihood fit for these normalisation factors can be seen in Table 5.15, which includes a normalisation of the Multi-jet contribution extracted in CRA-LM, a W+jets normalisation (W-CR) as well as a top background normalisation for the high mass case (TCR-HM). All values of normalisation factors described here are extracted simultaneously and therefore taking into account the effect of one normalised background onto another in each control region.

	Normalisation factor
μ_{MJLow}	1.00 ± 0.04
μ_W	1.04 ± 0.09
$\mu_{topHigh}$	0.71 ± 0.11

Table 5.15: Normalisation factors for the Multijet contribution (μ_{MJLow}) as well as W+jets and Top contribution.

Including CR-A of the ABCD multijet estimation for the low mass scenario (see Table 5.5) into the likelihood allows for a normalisation factor of the Multi-jet background. This is accounting for residual effects of the ABCD method (section 5.9.1), which is performed before the likelihood construction. A comparison of a kinematic distribution in CR-A of the low mass scenario before the background-only fit with the multijet VR-F (MJVR) is given in Figure 5.29. Clearly, the agreement of data and SM expectation in the control region is very good, even pre-fit (see Fig. 5.29a). This is confirmed in the validation region (see Fig. 5.29b) post-fit.

An overview of the pre and post-fit yields in the control regions and validation regions can be seen in Table 5.16.

In the simultaneous fit described here, the multi-jet contribution in both SR-LM and SR-HM is normalised according to the normalisation factor extracted in the Low-mass control region. The multijet normalisation factor is compatible with unity. The W+jets normalisation is equally

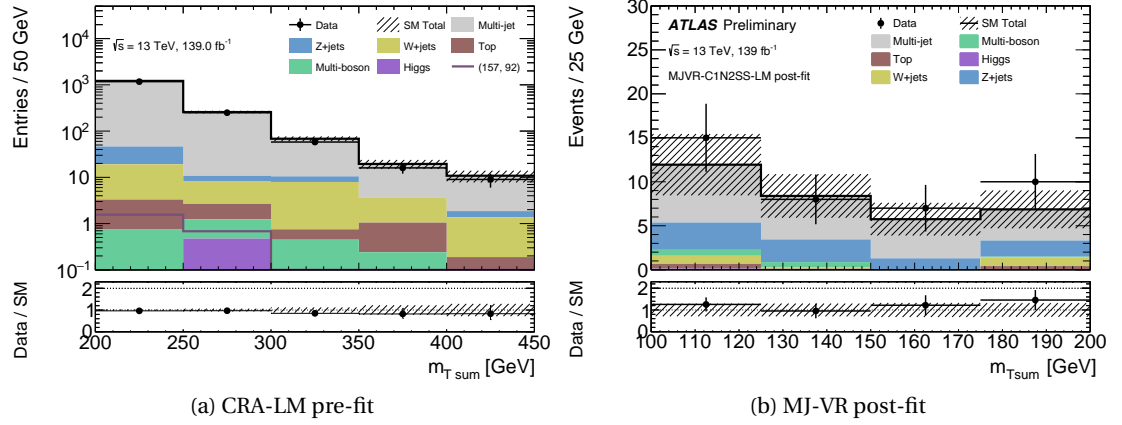


Figure 5.29: pre-fit Multijet CR-A (as defined in the ABCD method in section 5.9.1) and post-fit MJ-VR.

	WCR	WVR	TCRHighMass	TVRHighMass	CRALowMass	VRFLowMass
Observed events	25728	6662	96	12	1505	40
Fitted bkg events	25727.93 ± 160.69	7051.84 ± 937.00	96.00 ± 9.79	14.26 ± 2.29	1505.00 ± 38.79	32.95 ± 9.08
Fitted top events	812.54 ± 122.41	131.12 ± 21.28	73.90 ± 10.12	12.00 ± 2.20	5.24 ± 1.55	$0.99^{+1.04}_{-0.99}$
Fitted Zjets events	2529.37 ± 1242.66	737.12 ± 254.42	4.31 ± 1.92	0.81 ± 0.35	32.85 ± 16.36	9.30 ± 2.45
Fitted Wjets events	21735.92 ± 1292.76	6055.62 ± 869.02	13.69 ± 1.28	1.09 ± 0.13	33.33 ± 3.01	1.39 ± 1.31
Fitted Higgs events	20.70 ± 4.41	5.49 ± 1.23	0.98 ± 0.22	0.13 ± 0.03	0.53 ± 0.11	0.25 ± 0.06
Fitted Multiboson events	629.40 ± 175.98	122.50 ± 37.76	3.13 ± 1.12	0.22 ± 0.08	2.18 ± 0.96	1.47 ± 0.54
Fitted Multijet events	0.00 ± 0.00	0.00 ± 0.00	0.00 ± 0.00	0.00 ± 0.00	1430.86 ± 42.23	19.54 ± 8.55
MC exp. SM events	25334.52 ± 1840.56	6902.77 ± 896.15	126.13 ± 6.74	19.20 ± 2.16	1505.00 ± 47.18	32.92 ± 9.07
MC exp. top events	1148.86 ± 60.75	185.39 ± 15.50	104.49 ± 5.57	16.97 ± 2.02	5.24 ± 1.56	$0.99^{+1.04}_{-0.99}$
MC exp. Zjets events	2529.68 ± 1248.79	737.16 ± 255.66	4.31 ± 1.93	0.81 ± 0.35	32.85 ± 16.46	9.30 ± 2.47
MC exp. Wjets events	21005.88 ± 1110.67	5852.24 ± 739.21	13.23 ± 0.48	1.06 ± 0.09	32.21 ± 0.95	1.35 ± 1.26
MC exp. Higgs events	20.70 ± 4.44	5.49 ± 1.24	0.98 ± 0.22	0.13 ± 0.03	0.53 ± 0.11	0.25 ± 0.06
MC exp. Multiboson events	629.40 ± 177.17	122.50 ± 38.00	3.13 ± 1.13	0.22 ± 0.08	2.18 ± 0.97	1.47 ± 0.54
MC exp. Multijet events	0.00 ± 0.00	0.00 ± 0.00	0.00 ± 0.00	0.00 ± 0.00	1431.98 ± 42.07	19.55 ± 8.51

Table 5.16: Summary of post and pre-fit Yields in all control and validation regions

compatible with unity within the associated uncertainties. This is shown in Figure 5.30, comparing the W-CR pre-fit with the post-fit W-VR. A good agreement between data and SM expectation can be seen.

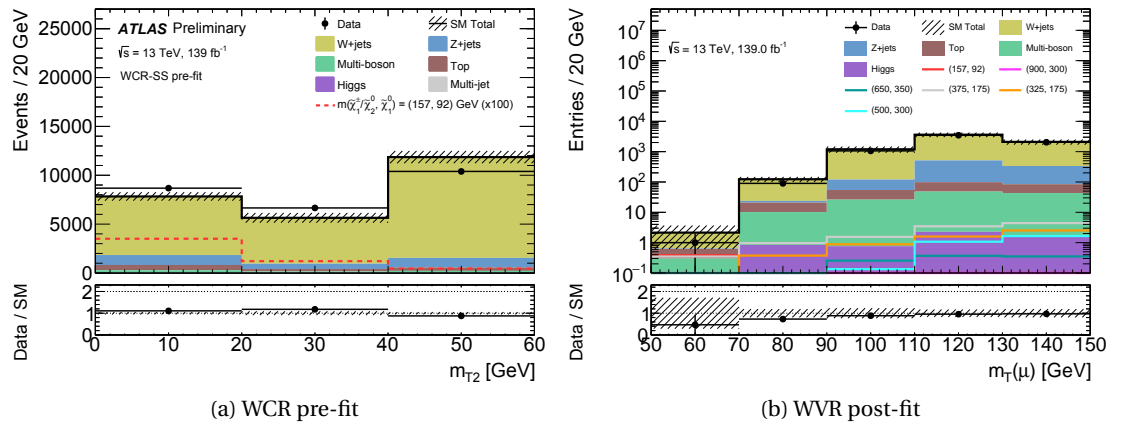


Figure 5.30: pre-fit WCR and post-fit WVR.

The top normalisation is leading to a normalisation of the Monte Carlo below its nominal value, which is motivated by the overestimation of Monte-Carlo simulation with respect to data vis-

ible in the Top control and validation regions pre-fit. After the background-only fit, a good agreement between SM prediction and observed data can be seen in Figure 5.31.

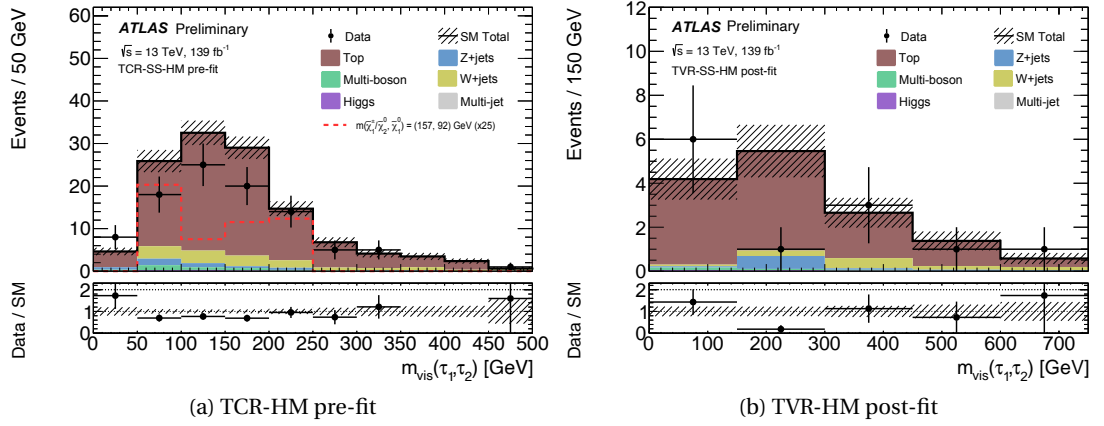


Figure 5.31: pre-fit Top control region and post fit top validation region - showing improvement in the top modelling through the fit [95].

The uncertainties on the normalisation factors are largely dominated by the statistical uncertainties in the control regions. Other contributions to the uncertainty can come from correlation effects. The normalisation factors and nuisance parameters describing all systematic uncertainties considered can be correlated. A reduced correlation matrix is shown in Figure 5.32.

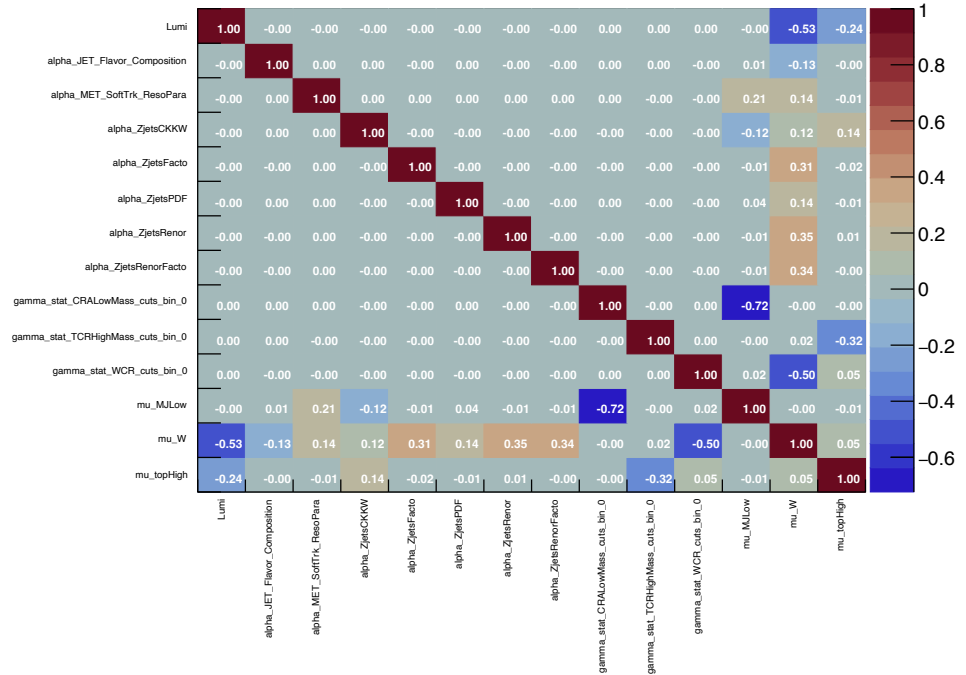


Figure 5.32: Reduced correlation Matrix for the C1N2SS background only fit.

This shows a correlation between the W+jets normalisation and the Z+jets theoretical uncertainties. This correlation is due to the sizeable (yet not dominating) Z+jets contribution in the WCR and WVR due to the large available statistics in the WCR and WVR compared to other analysis regions. A small change in the Z+jets yields due to one of the theory uncertainty related

Uncertainty of channel	SRLow	SRHigh
Total background expectation	1.96	2.10
Total statistical ($\sqrt{N_{\text{exp}}}$)	± 1.40	± 1.45
Total background systematic	± 0.71 [36.22%]	± 1.08 [51.52%]
Statistical uncertainty	± 0.48	± 0.64
Multi-jet background	± 0.41	–
MET soft-term resolution	± 0.26	± 0.07
Multi-boson theory uncertainty	± 0.15	± 0.24
Jet energy scale and resolution	± 0.10	± 0.81
Normalization factors	± 0.05	± 0.09
Tau identification and energy scale	± 0.04	± 0.05

Table 5.17: Breakdown of dominating uncertainties in the signal regions

nuisance parameters leads to comparatively large changes in the Z+jets yield, in itself leading to a smaller necessary W+jets normalisation.

With the normalisation factors extracted in the background only fit, also the systematic uncertainties included in the fit as nuisance parameters are constrained. A post-fit breakdown of the dominating uncertainties in the signal regions is given in table 5.17.

With this validated background estimation and systematic uncertainties in place, the signal regions were unblinded. Exemplary kinematic distributions of the unblinded SR-C1N2SS-LM are given in Figure 5.33 as well as in Figure 5.34 for SR-C1N2SS-HM.

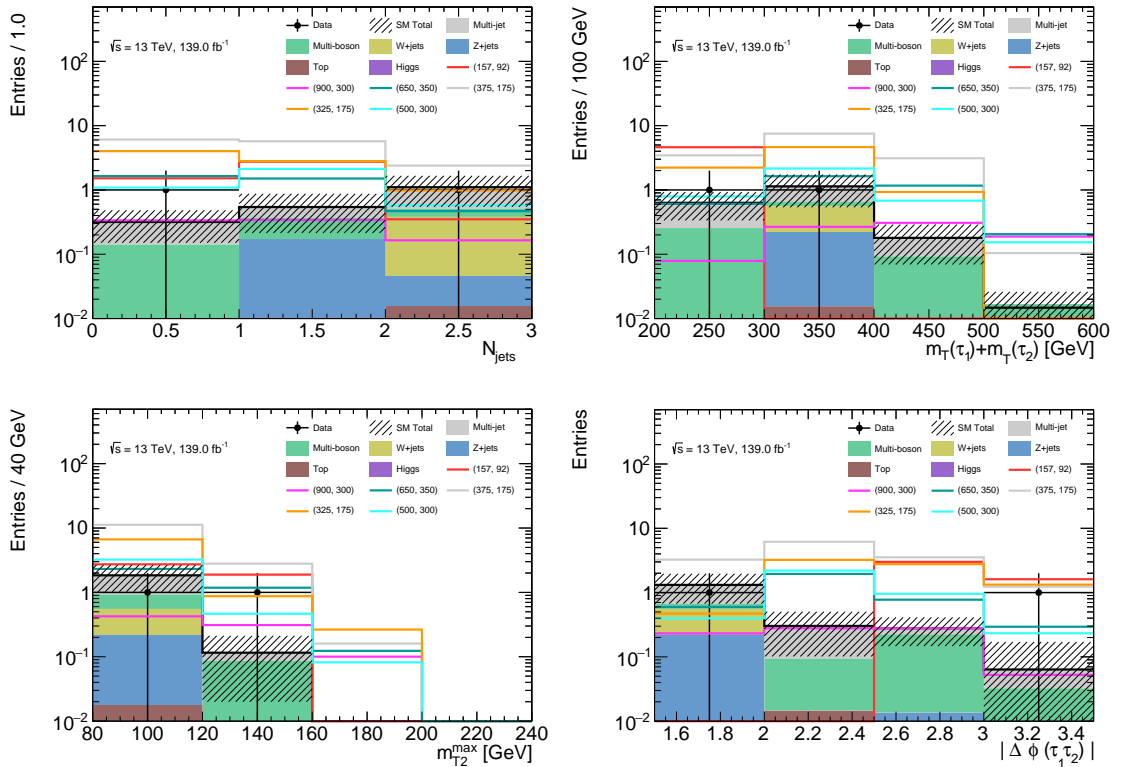


Figure 5.33: Unblinded signal region distributions for SR-C1N2SS-LM. All normalisation factors extracted in the background-only fit are applied. The hashed band includes statistical and systematic errors.

A breakdown of the signal region yields pre- and post-fit can be seen in table 5.18. This shows a

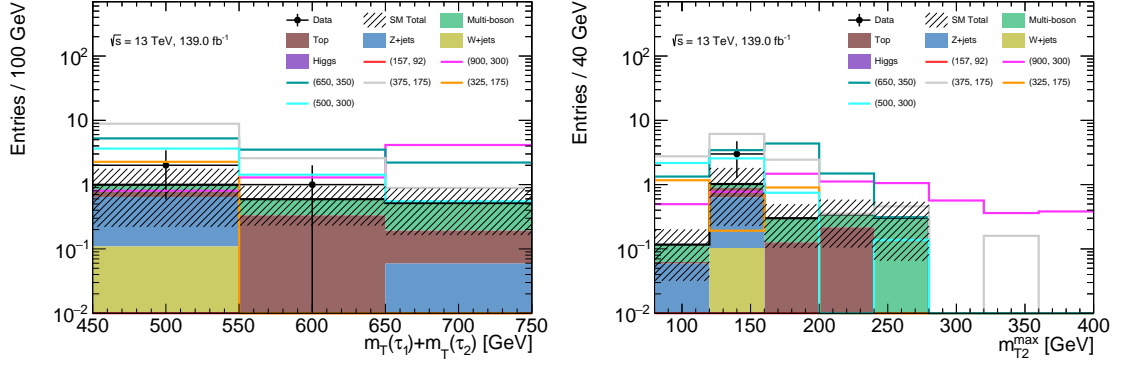


Figure 5.34: Unblinded signal region kinematic distributions for SR-C1N2SS-HM. All normalisation factors extracted in the background-only fit are applied. The hashed band includes statistical and systematic errors.

table.results.yields channel	SR-C1N2SS-LM	SR-C1N2SS-HM
Observed events	2	3
Fitted bkg events	1.96 ± 0.71	2.10 ± 1.08
Fitted top events	$0.01^{+0.02}_{-0.01}$	0.59 ± 0.20
Fitted Zjets events	0.20 ± 0.15	$0.59^{+0.85}_{-0.59}$
Fitted Wjets events	0.33 ± 0.25	0.10 ± 0.05
Fitted Higgs events	$0.00^{+0.01}_{-0.00}$	0.02 ± 0.01
Fitted Multiboson events	0.47 ± 0.20	0.81 ± 0.36
Fitted Multijet events	0.94 ± 0.47	–
MC exp. SM events	1.95 ± 0.71	2.35 ± 1.14
MC exp. top events	$0.01^{+0.02}_{-0.01}$	0.84 ± 0.25
MC exp. Zjets events	0.20 ± 0.15	$0.59^{+0.85}_{-0.59}$
MC exp. Wjets events	0.32 ± 0.25	0.10 ± 0.05
MC exp. Higgs events	$0.00^{+0.01}_{-0.00}$	0.02 ± 0.01
MC exp. Multiboson events	0.47 ± 0.20	0.81 ± 0.36
MC exp. Multijet events	0.94 ± 0.47	–

Table 5.18: pre and post fit yields in the signal regions

good agreement of the observed yields with the SM expectation within uncertainties. Comparing the pre- and post-fit yields, a clear reduction of the top contribution through its normalisation is visible. Due to its negligible, negative contribution in the SR-C1N2SS-HM, the multi-jet contribution is set to a zero value in the fit.

With the simultaneous likelihood fit performed in the background only fit, a statement on the agreement of the observed events with the background-only hypothesis can be made through a simple evaluation of the model differences, taking into account the systematic uncertainties. An overview of this statement in terms of significances in measures of standard deviations is given in Figure 5.35, showing a visualisation of the post-fit yields in all validation and signal regions; also including the Multiboson validation region. A good agreement between data and SM expectation, within the uncertainties can be observed throughout all regions.

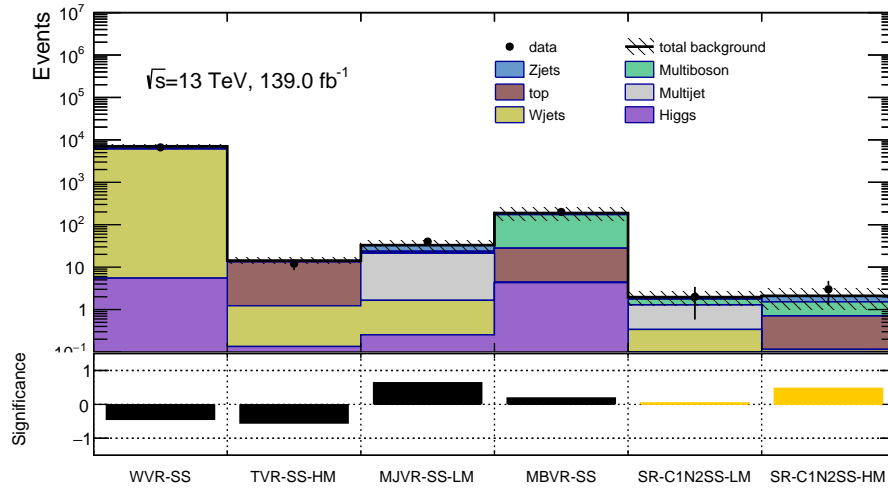


Figure 5.35: Pull Plot: Summary of all validation and signal regions included in the background only fit and the significance of the difference of background estimation compared to observed data.

5.13 Interpretation

With no significant excesses observed in the signal region, the observed results were interpreted in a model-dependent as well as model-independent approach described in the following sections.

5.13.1 Model dependent interpretation

As described in previous sections (sec. 5.1 and 5.8.2), the signal regions were designed to have sensitivity to the simplified model describing the production of a $\tilde{\chi}_1^\pm$ and $\tilde{\chi}_2^0$. Using the CLs approach described in section 5.11, a hypothesis test is performed for mass parameter value highlighted in section 5.4. Mass points with a CLs value below 0.05 are excluded. This can be seen through the exclusion contours in figure 5.36a, 5.36b and 5.36c. The CLs value can be calculated for each signal region independently, as well as the statistical combination of both regions. The contours are shown in the $\tilde{\chi}_1^0$ versus $\tilde{\chi}_1^\pm$ mass plane, with the stau mass parameter $x = 0.5$. The expected limit as dashed line is describing the limit up to which all enclosed mass points are excluded at a 95% confidence level, assuming that the observed data is equivalent to the SM expectation. This is a measure of the designed analysis sensitivity and is accompanied by the 'yellow band', visualising how the expected limit shifts when varying the associated experimental uncertainties by $\pm 1\sigma_{\text{exp}}$. This experimental uncertainty band includes all experimental and theoretical systematic uncertainties on the background estimations as well as on the signal prediction, apart from an inclusive cross section uncertainty on the signal prediction. This uncertainty purely due to the inclusive cross section uncertainty on the signal expectation is visualised in the dashed red band around the observed limit in Figure 5.36c.

The region SR-C1N2SS-LM (Fig. 5.36a) is able to exclude mass points with low masses and to-

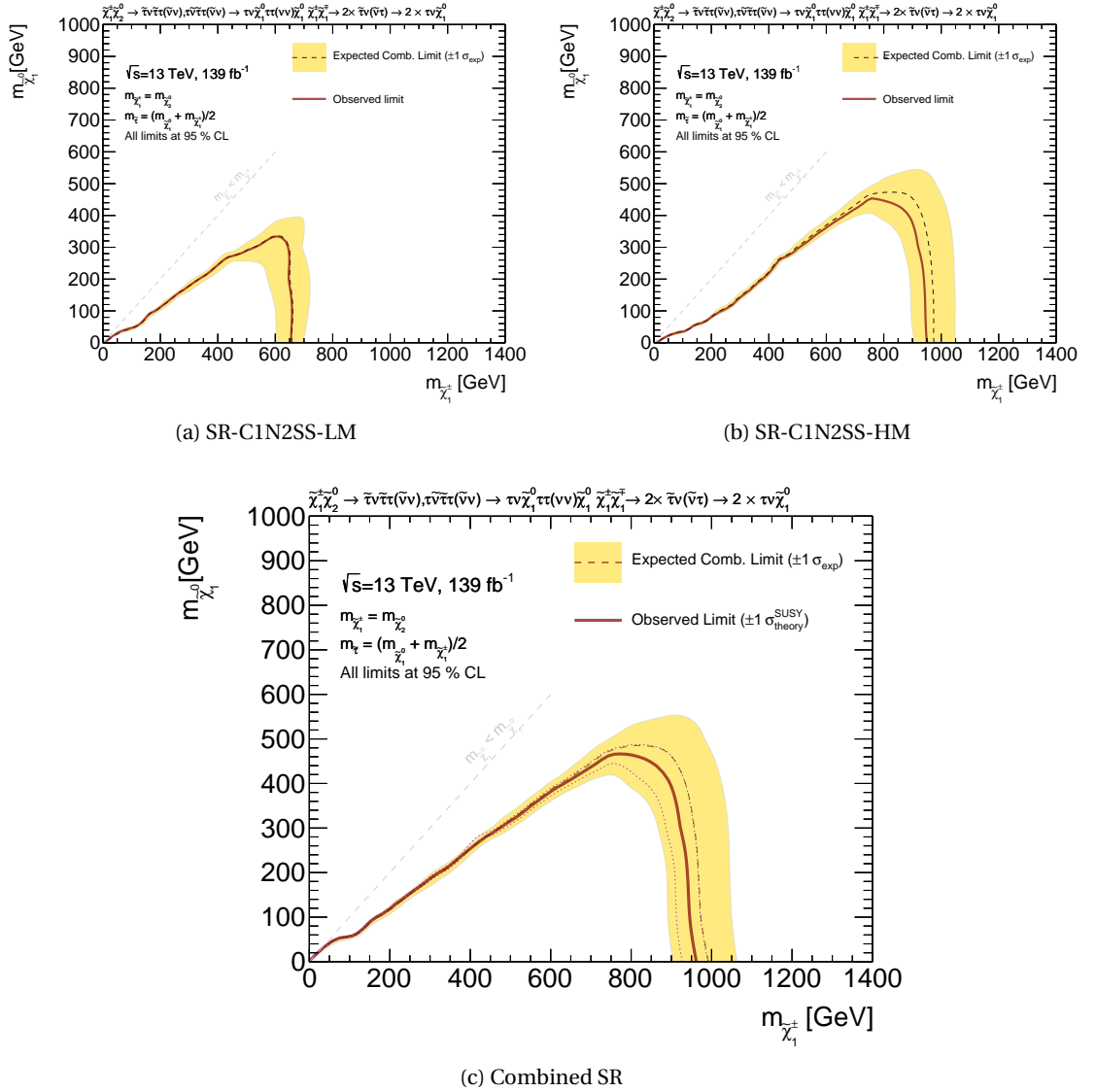


Figure 5.36: Exclusion limits in the SR-C1N2SS-LM (a), SR-C1N2SS-HM (b) as well as both signal regions statistically combined (c)

towards the kinematic diagonal. The region SR-C1N2SS-HM is pushing the analysis sensitivity towards higher chargino masses (Fig. 5.36b). The statistical combination of SR-C1N2SS-LM and SR-C1N2SS-HM is decreasing the associated statistical uncertainty and therefore further increasing the analysis sensitivity. As can be seen both in the SR-C1N2SS-HM as well as in the combined exclusion contour, for high $\tilde{\chi}_1^\pm$ masses the observed exclusion is weaker than the expected exclusion reach. This is due to a slight fluctuation in observed data in the SR-C1N2SS-HM compared to its nominal SM expectation. This fluctuation is well within the systematic uncertainties (within the yellow band). Masses of the lightest chargino up to 960 GeV for massless lightest neutralinos were excluded. Mass differences between the $\tilde{\chi}_1^\pm$ and $\tilde{\chi}_2^0$ as little as 30 GeV have been excluded for a $\tilde{\chi}_1^\pm$ mass of 80 GeV.

5.13.2 Model independent interpretation

The most general result of any **BSM** search is offered through model-independent interpretations. This neglects any assumption of the shape or yield of a signal model and offers an upper limit on the visible cross section. In both signal regions, an upper-limit, model-independent, fit is performed to extract the highest possible cross section that a **BSM** signal could have in order for the analysis to have noticed the contribution within 95% confidence level. This is measured through the maximum number of signal events that can populate the signal regions in order to still be in agreement with the background-only hypothesis.

Signal channel	$\langle\epsilon\sigma\rangle_{obs}^{95}$ [fb]	$\langle\epsilon\sigma\rangle_{exp}^{95}$ [fb]	S_{obs}^{95}	S_{exp}^{95}	CL_B	$p(s=0)$ (Z)
SR-C1N2SS-LM	0.03	0.03	4.7	$4.6^{+1.8}_{-0.5}$	0.56	0.41 (0.23)
SR-C1N2SS-HM	0.04	0.04	6.2	$5.0^{+2.1}_{-0.9}$	0.73	0.39 (0.29)

Table 5.19: Listed are the observed and expected 95% CL upper limit on the visible cross section ($\langle\epsilon\sigma\rangle_{obs}^{95}$, $\langle\epsilon\sigma\rangle_{exp}^{95}$ respectively), the upper limit on the number of signal events ($S_{obs/exp}^{95}$) as well as the confidence level for the background-only hypothesis CL_B . The last column describes the discovery p -value.

The results of the model-independent upper limits are shown in table 5.19. Listed are the observed and expected 95% CL upper limit on the visible cross section ($\langle\epsilon\sigma\rangle_{obs}^{95}$, $\langle\epsilon\sigma\rangle_{exp}^{95}$ respectively), the upper limit on the number of signal events ($S_{obs/exp}^{95}$) as well as the confidence level for the background-only hypothesis CL_B . The last column describes the discovery p -value. The largest difference between observed and expected upper limit on the signal events can be seen in SR-C1N2SS-HM, with an expected S_{exp}^{95} of $5.0^{+2.1}_{-0.9}$, whereas the observed limit reaches 6.2. This is due to the slight upward fluctuation in data in the SR-C1N2SS-HM, allowing for a larger potential signal contribution.

5.14 The opposite sign analysis

As was discussed in section 5.2, the simplified model under investigation in the same-sign di-tau final state search described above has been previously searched for in partial Run-2 data in an opposite-sign di-tau final state [99].

This opposite-sign di-tau final state search has been re-optimised for the full Run-2 data set and statistically combined with the same-sign analysis to improve the overall model sensitivity.

The author has not been involved in the design of the opposite-sign analysis, they have been developed alongside each other with a final statistical combination in mind, sharing the data and Monte Carlo samples described in section 5.4. The statistical combination has been performed by the author. For context, a quick overview of the opposite-sign analysis is given in the following.

Two separate analysis strategies have been developed for the two simplified models targeted (see Fig. 5.37. One for the chargino pair ($\tilde{\chi}_1^\pm \tilde{\chi}_1^\pm$) production (Fig 5.37b) and one for the chargino-neutralino ($\tilde{\chi}_1^\pm \tilde{\chi}_2^0$) production (Fig 5.37a). The signal regions used to target the two

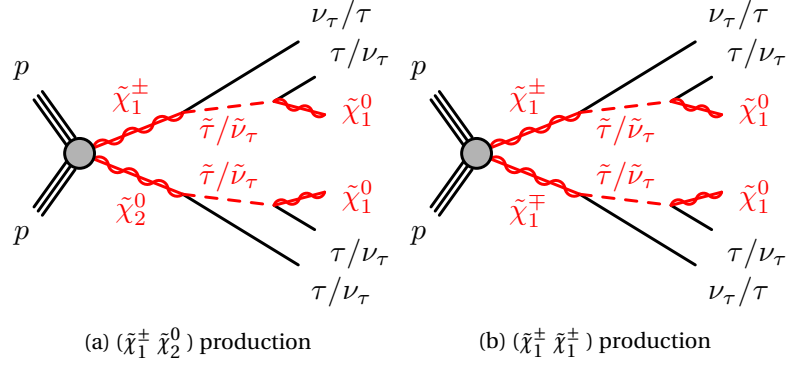


Figure 5.37: Simplified models considered in the opposite-sign analysis.

scenarios are not orthogonal. Therefore separate exclusion fits are performed for the two scenarios. If the $\tilde{\chi}_1^\pm$ mass is assumed to be equal to the $\tilde{\chi}_2^0$ mass in the chargino pair production model, the sensitivity of the opposite-sign analysis can be estimated to both scenarios jointly. This is done in the $(\tilde{\chi}_1^\pm \tilde{\chi}_2^0)$ signal regions. This combined sensitivity and combined exclusion contour of the opposite sign analysis is used for the statistical combination with the same-sign analysis.

The leading background contributions for the opposite-sign analysis are Multi-jet, Multi-boson, W+jets as well as Z+jets contributions. An ABCD method similarly to the one described in section 5.9.1 is used to estimate the Multi-jet contribution in the signal regions. A dedicated W+jets control and validation region is defined in a final state including a muon and a hadronically decaying tau lepton. Validation regions are defined for top related processes, Z+jets as well as Multi-boson processes.

5.15 Combined gaugino pair results

A summary of all validation and signal regions considered in both the opposite-sign as well as same-sign analyses after the analysis-specific background-only fit is shown in Figure 5.38. Good agreement between the SM expectation and data in all validation regions can be observed. In the SR-C1C1-LM, a slight underfluctuation of data with respect to the SM expectation can be seen.

Figure 5.39a shows the statistical combination of the opposite-sign and same-sign analyses. Shown in green is the expected and observed contour of the joint SR-C1N2SS-LM and SR-C1N2SS-HM exclusion. In blue is given the opposite-sign analyses sensitivity to both the chargino pair as well as chargino-neutralino production as achieved in the $(\tilde{\chi}_1^\pm \tilde{\chi}_2^0)$ signal regions.

To further visualise the gain in sensitivity through both analyses towards the kinematic diagonal, the $\Delta m(\tilde{\chi}_1^\pm, \tilde{\chi}_1^0)$ is given for low $\tilde{\chi}_1^\pm / \tilde{\chi}_2^0$ masses. The same-sign analysis extends the sensitivity in the di-tau final state to lower mass splittings, down to as little as 30 GeV for a $\tilde{\chi}_1^\pm$ mass of 80 GeV. The combined model interpretation is excluding $\tilde{\chi}_1^\pm$ masses up to 1160 GeV for a massless $\tilde{\chi}_1^0$, exceeding the sensitivity of previous model investigations. This result presents a

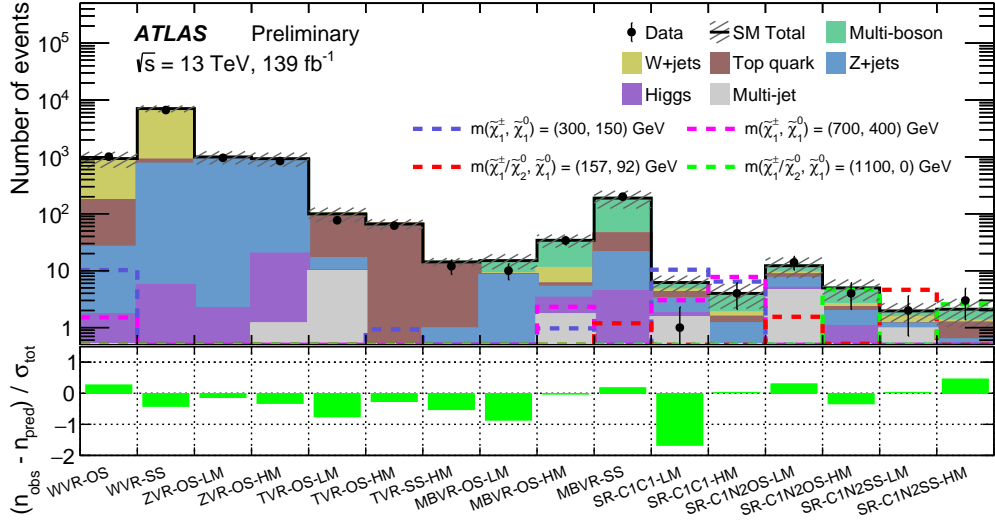


Figure 5.38: Summary of all validation and signal regions considered in the opposite-sign and same-sign analyses after the analysis-specific background-only fits [137].

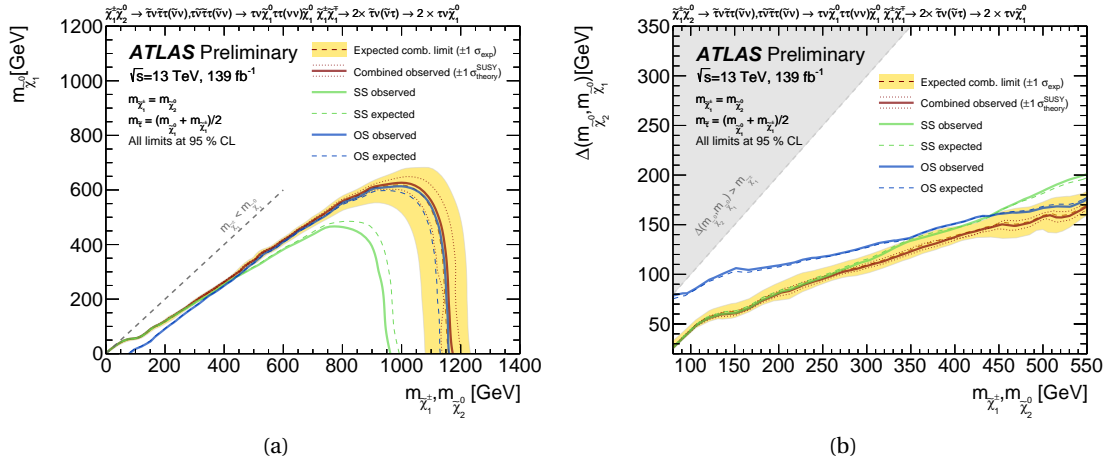


Figure 5.39: Combined exclusion contours of the opposite-sign and same-sign analysis [137]. In (a) the exclusion limits at 95 % CL are given in the $\tilde{\chi}_1^\pm / \tilde{\chi}_2^0$ versus $\tilde{\chi}_1^0$ mass plane. In (b) the same exclusion limits are shown with respect to the mass splitting $\Delta m(\tilde{\chi}_1^\pm, \tilde{\chi}_1^0)$ in dependency to the $\tilde{\chi}_1^\pm / \tilde{\chi}_2^0$ mass.

world-leading sensitivity to this simplified model both in the high $\tilde{\chi}_1^\pm / \tilde{\chi}_2^0$ mass range as well as low mass splittings of $\Delta m(\tilde{\chi}_1^\pm, \tilde{\chi}_1^0)$ in a hadronic di-tau final state and has not been investigated by other experiments to a similar extend.

CONCLUSIONS

*Don't let anyone rob you of your
imagination, your creativity, or
your curiosity.*

Mae Jemison

In this thesis, the extensive search program of the [ATLAS](#) experiment for supersymmetric particles was extended with a search for the production of the lightest chargino and next-to-lightest neutralino decaying via staus into a final state with at least two hadronically decaying tau leptons. This thesis has extended the Run-2 [ATLAS SUSY](#) search program in these scenarios into a final state with at least two same-sign hadronic taus. This final state had not been investigated during Run-2. The analysis has targeted not only higher $\tilde{\chi}_1^\pm / \tilde{\chi}_2^0$ masses than excluded by a previous analysis with partial Run-2 data and opposite-sign taus, but also aimed to push the sensitivity toward scenarios with small mass differences between the $\tilde{\chi}_2^0$ and $\tilde{\chi}_1^0$ and low $\tilde{\chi}_1^\pm$ masses. Dedicated signal regions have been designed for both scenarios.

A data-driven method was developed to estimate multi-jet backgrounds populating especially the low mass signal region. Very good agreement between the background expectation in designated multi-jet backgrounds has been observed. For top related background processes, a control and validation region approach has been taken. The choice of regions was designed to ensure a top background estimation including all type of tau contributions. For [SM](#) backgrounds with a W boson in association with jets, a dedicated strategy replacing one hadronically decaying tau with a light lepton has been designed. Similarly for the validation of Multi-boson processes, increased statistics in light-lepton final states have been utilized to estimate the background reliably.

A variety of experimental and theoretical uncertainties have been evaluated and considered in this analysis, ensuring a conservative but realistic statistical interpretation of the search results.

No significant excesses have been observed in the designed search regions. The observed data events in both signal regions are within the [SM](#) expectation. In the absence of an excess, this has been interpreted in 95% confidence level exclusion limits in the $\tilde{\chi}_1^\pm, \tilde{\chi}_1^0$ mass plane, as well as an additional interpretation in the $\Delta m(\tilde{\chi}_1^\pm, \tilde{\chi}_1^0)$ vs $\tilde{\chi}_1^0$ mass plane.

A statistical combination with a search for the same final state topology in an opposite di-tau final state has been performed. The combined model interpretation is increasing the excluded mass range up to $\tilde{\chi}_1^\pm$ masses of 1160 GeV for massless $\tilde{\chi}_1^0$. The same-sign analysis discussed in this thesis is significantly contributing to push the sensitivity towards low mass-splittings. This region is challenging due to its soft decay products, which is especially difficult in hadronic final states.

These efforts have further narrowed down on [SUSY](#) and additionally provided valuable model-independent results in terms of upper cross section limits on [BSM](#) signal contribution, in an extreme di-tau kinematic phase space. These model-independent results can be re-interpreted by the theory as well as extended experimental community.

Next to the search for new physics, performance studies of the [ATLAS](#) electron trigger have been presented. These performance studies have provided crucial understanding of electron trigger behaviour throughout Run-2. Studies on the electron trigger performance in AF2 detector simulation have highlighted the need to question and reassure previous modelling assumptions.

With Run-3 of the [LHC](#) just starting, particle physics has an exciting period ahead. The studies and analysis presented in this paper present a small but important wheel in the wide search program and [ATLAS](#) operation to continue to learn and unravel the open questions in particle physics lying ahead.

APPENDIX

A

A.1 Theoretical uncertainty breakdown

Summary of the theoretical uncertainty values calculated according to the procedure discussed in section 5.10. All values are given in %.

Top related theoretical uncertainties

	Wt single top		ttbar		Joint top background					
	σ_{HS}	σ_{PS}	σ_{HS}	σ_{PS}	σ_{PDF}	σ_{μ_F}	σ_{μ_R}	σ_{μ_R, μ_F}	σ_{ISR}	σ_{FSR}
SR-C1N2SS-LM	± 7.7	± 1.5	± 7.8	± 23.2	+0.0 -0.0	+0.0 -0.0	+0.0 -0.0	+0.0 -0.0	+0.0 -0.0	+0.0 -0.0
SR-C1N2SS-HM	± 7.7	± 1.5	± 7.8	± 23.2	0.1 -0.1	+0.5 -0.9	+9.1 -6.3	+8.4 -5.8	+0.1 -0.0	+0.1 -0.1
W-CR	± 9.9	± 15.5	± 4.0	± 14.1	0.0 -0.0	+1.1 -1.3	+0.4 -0.4	+0.7 -0.8	+0.0 -0.0	+0.0 -0.0
W-VR	± 3.6	± 11.0	± 4.5	± 16.4	0.0 -0.0	+0.3 -0.4	+0.3 -0.3	+0.0 -0.0	+0.0 0.0	+0.0 0.0
MB-VR	± 3.3	± 15.3	± 9.3	± 17.0	0.0 -0.0	+0.0 -0.1	+0.4 -0.4	+0.5 -0.4	+0.0 0.0	+0.0 0.0
TVR-HM	± 16.2	± 5.8	± 10.6	± 22.7	0.0 -0.0	+0.1 -0.2	+0.8 -1.0	+0.9 -1.2	+0.0 0.0	+0.0 0.0
TCR-HM	± 16.2	± 5.8	± 10.6	± 22.7	0.0 -0.0	+0.1 -0.1	+0.9 -1.0	+0.8 -0.9	+0.0 0.0	+0.0 0.0
CRA-LM	± 7.7	± 1.5	± 7.8	± 23.2	+0.1 -0.1	+7.5 -6.5	+6.7 -4.5	+15.6 -10.2	+1.2 -1.2	+0.5 -0.5
VRF-LM	± 7.7	± 1.5	± 7.8	± 23.2	0.0 -0.0	+0.3 -0.4	+0.4 -0.5	+0.0 -0.2	+0.0 -0.0	+0.0 -0.0

Table A.1: Theoretical uncertainties for the top related standard model background processes

Multi-boson related theoretical uncertainties

	σ_{CKKW}	σ_{QSF}	σ_{CSSKIN}	σ_{PDF}	σ_{μ_F}	σ_{μ_R}	σ_{μ_R, μ_F}
SR-C1N2SS-LM	+4.66 -2.31	+4.46 -4.39	± 2.34	± 6.6	3.2 -1.6	16.6 -12.8	18.7 -15.0
SR-C1N2SS-HM	+4.66 -2.31	+4.46 -4.39	± 2.34	± 6.2	0.8 -0.8	17.2 -12.8	15.0 -13.9
W-CR	+1.30 -4.99	+5.56 -4.97	± 1.11	± 11.0	0.8 -0.7	10.8 -7.9	11.4 -8.6
W-VR	+8.03 -2.90	± 7.88	± 5.56	± 6.2	0.9 -0.7	13.4 -9.9	14.2 -10.7
MB-VR	± 3.25	+4.86 -6.00	± 4.74	± 7.3	3.5 -2.4	17.3 -13.3	20.3 -15.9
TVR-HM	+8.16 -6.83	± 7.32	± 3.34	± 9.6	3.7 -3.2	17.0 -13.0	20.0 -15.9
TCR-HM	+8.16 -6.83	± 7.32	± 3.34	± 8.4	2.2 -1.4	20.0 -14.7	21.0 -16.6
CRA-LM	+4.66 -2.31	+4.46 -4.39	± 2.34	± 17.8	1.5 -0.5	15.1 -11.0	16.1 -11.9
VRF-LM	+4.66 -2.31	+4.46 -4.39	± 2.34	± 10.7	3.1 -1.6	18.6 -13.6	20.5 -15.7

Table A.2: MultiBoson theoretical uncertainties

W+jets theoretical uncertainties

	σ_{PDF}	σ_{μ_F}	σ_{μ_R}	σ_{μ_F, μ_R}	σ_{CKKW}	σ_{QSF}
SR-C1N2SS-LM	± 4.3	4.1 -4.2	4.8 -7.9	8.3 -12.8	12.21 -5.95	9.16 9.16
SR-C1N2SS-HM	± 9.6	2.3 -1.9	-0.9 -1.0	0.7 -3.1	± 24.23	± 27.12
W-CR	± 2.5	3.0 -5.3	22.6 -13.6	14.2 -11.9	± 1.76	± 1.09
W-VR	± 2.3	3.5 -5.7	22.8 -13.6	13.9 -11.5	± 3.27	± 1.12
MB-VR	± 2.6	0.3 -87.1	12.7 -11.8	± 84.0	± 22.05	± 38.04
TVR-HM	± 14.2	± 15.6	± 7.5	6.8 -21.2	4.87 -18.31	± 7.05
TCR-HM	± 13.1	± 11.0	2.6 -2.8	3.3 -11.9	18.62 -7.66	± 14.85
CRA-LM	± 3.0	2.9 -4.3	6.8 -7.8	9.7 -11.3	± 28.20	± 42.06
VRF-LM	± 2.4	1.8 -8.6	1.5 -1.5	0.1 -5.9	± 25.20	± 24.07

Table A.3: W+jets theoretical uncertainties

Z+jets theoretical uncertainties

	σ_{PDF}	σ_{μ_F}	σ_{μ_R}	σ_{μ_R, μ_F}	σ_{CKKW}	σ_{QSF}
SR-C1N2SS-LM	± 19.4	3.5 -2.7	13.5 -15.5	16.5 -18.3	± 21.02	± 20.07
SR-C1N2SS-HM	± 17.7	4.3 -4.7	1.2 -0.9	2.8 -4.4	± 18.43	± 18.23
WCR	± 10.4	± 22.8	± 25.4	± 24.7	± 9.74	± 5.65
WVR	± 12.9	0.3 -1.5	17.1 -11.3	15.9 -11.1	± 10.59	± 5.21
MBVR	± 1.5	± 4.5	11.6 -4.7	4.7 -2.1	± 27.65	± 22.32
TVR-HM	± 2.0	0.8 -0.6	5.7 -7.7	5.0 -6.9	-6.45 5.33	± 14.94
TCR-HM	± 1.7	2.7 -2.0	9.8 -11.4	7.3 -8.6	± 38.61	-0.59 20.68
CRA-LM	± 9.1	0.8 -1.2	1.5 -0.1	0.7 0.3	-26.94 17.57	-5.04 10.02
VRF-LM	± 3.0	1.6 -1.3	± 6.3	4.7 -4.6	-13.66 8.86	± 10.02

Table A.4: Z+jets theoretical uncertainties

Higgs theoretical uncertainties

	σ_{PDF}	σ_{μ_F}	σ_{μ_R}	σ_{μ_R, μ_F}	σ_{ISR}	σ_{FSR}
SR-C1N2SS-LM	0.0 0.0	71.3 -60.6	119.2 -80.0	223.6 -124.4	11.1 -10.6	31.4 -15.0
SR-C1N2SS-HM	0.0 0.0	1.4 -1.5	0.7 -0.2	1.9 -1.8	4.2 -6.7	± 17.1
W-CR	0.0 0.0	0.1 -0.1	0.1 -0.1	0.3 -0.2	0.0 0.0	± 0.3
W-VR	0.0 0.0	0.1 -0.1	0.5 -0.3	0.7 -0.3	0.3 -0.4	24.4 -2.5
MB-VR	0.0 0.0	0.5 -0.5	1.2 -0.8	1.8 -1.1	± 0.1	± 1.8
TVR-HM	0.0 0.0	0.0 0.0	0.0 0.0	0.0 0.0	0.0 0.0	0.0 0.0
TCR-HM	0.0 0.0	2.6 -2.4	7.0 -4.4	10.4 -6.4	0.5 -0.8	4.7 -15.9
CRA-LM	0.0 0.0	0.0 0.0	0.0 0.0	0.0 0.0	0.0 0.0	0.0 0.0
VRF-LM	0.0 0.0	0.0 0.0	0.0 0.0	0.0 0.0	0.0 0.0	0.0 0.0

Table A.5: Higgs theoretical uncertainties

GLOSSARY

ALICE	A Large Ion Collider Experiment	
ATLAS	A Toroidal LHC ApparatuS	ix
BDT	Boosted Decision Tree	x
BSM	Beyond Standard Model	30
CERN	European Organization for Nuclear Research	17
CL	Confidence Level	
CMS	Compact Muon Solenoid	ix
CMB	Cosmic Microwave Background	9
CR	Control Region	66
CSC	Cathode Strip Chamber	25
CTP	Central Trigger Processor	27
DM	Dark Matter	8
ECAL	Electromagnetic Calorimeter	ix
FCAL	Forward Calorimeter	24
FSR	Final State Radiation	93
GSF	Gaussian Sum Filter	32
GRL	Good Runs List	64
HCAL	Hadronic Calorimeter	23
HLT	High Level Trigger	x
IBL	Insertable B-Layer	ix
ID	Inner Detector	ix
ISR	Initial State Radiation	93
JVT	Jet vertex Tagger	34
L1	Level-1	44

Glossary	114
LAr Liquid Argon	25
LHC Large Hadron Collider	ix
LHCb Large Hadron Collider beauty	
LHCf Large Hadron Collider forward	
LO Leading Order	62
LSP Lightest Supersymmetric Particle	ix
MC Monte Carlo	xi
MDT Monitored Drift Tube	25
MoEDAL Monopole & Exotics Detector At the LHC	
MS Muon Spectrometer	25
MSSM Minimal Supersymmetric Standard Model	11
NLO Next-to-Leading Order	62
NNLO Next-to-Next-to-Leading Order	62
NLL Next-to-Leading-Logarithmic	62
NNLL Next-to-Next-to-Leading-Logarithmic	62
PDF Parton Distribution Function	93
PSB Proton Synchrotron Booster	17
QCD Quantum Chromodynamics	8
QED Quantum Electrodynamics	7
RNN Recursive Neural Network	x
RoI Region of Interest	39
RPC <i>R</i> -Parity Conserving	25
RPC Resistive-Plate Chamber	25
SCT SemiConductor Tracker	22
SM Standard Model	xi
SPS Super Proton Synchrotron	17
SR Signal Region	66
SUSY Supersymmetry	1
TGC Thin-Gap Chamber	25
TOTEM TOTal cross section, Elastic scattering and diffraction dissociation Measurement at the LHC	
TRT Transition Radiation Tracker	22
VR Validation Region	66
WIMP Weakly Interacting Massive Particle	1

BIBLIOGRAPHY

- [1] J. J. Thomson, *Cathode Rays*, *Philosophical Magazine* **44** (1897) 293–316. 1
- [2] M. L. Perl, G. S. Abrams, A. M. Boyarski, M. Breidenbach, D. D. Briggs, F. Bulos, W. Chinowsky, J. T. Dakin, G. J. Feldman, C. E. Friedberg, D. Fryberger, G. Goldhaber, G. Hanson, F. B. Heile, B. Jean-Marie, J. A. Kadyk, R. R. Larsen, A. M. Litke, D. Lüke, B. A. Lulu, V. Lüth, D. Lyon, C. C. Morehouse, J. M. Paterson, F. M. Pierre, T. P. Pun, P. A. Rapidis, B. Richter, B. Sadoulet, R. F. Schwitters, W. Tanenbaum, G. H. Trilling, F. Vannucci, J. S. Whitaker, F. C. Winkelmann, and J. E. Wiss, *Evidence for Anomalous Lepton Production in $e^+ - e^-$ Annihilation*, *Phys. Rev. Lett.* **35** (1975) 1489–1492.
<https://link.aps.org/doi/10.1103/PhysRevLett.35.1489>. 1
- [3] ATLAS Collaboration, *Observation of a new particle in the search for the Standard Model Higgs boson with the ATLAS detector at the LHC*, *Physics Letters, Section B: Nuclear, Elementary Particle and High-Energy Physics* **716** no. 1, (2012) 1–29, [arXiv:1207.7214v2](https://arxiv.org/abs/1207.7214v2). <http://dx.doi.org/10.1016/j.physletb.2012.08.020>. 1, 3, 7
- [4] CMS Collaboration, *Observation of a new boson at a mass of 125 GeV with the CMS experiment at the LHC*, *Physics Letters, Section B: Nuclear, Elementary Particle and High-Energy Physics* **716** no. 1, (2012) 30–61, [arXiv:1207.7235](https://arxiv.org/abs/1207.7235).
<https://arxiv.org/abs/1207.7235v2>. 1, 3, 7
- [5] ATLAS Collaboration, *A detailed map of Higgs boson interactions by the ATLAS experiment ten years after the discovery*, *Nature* **2022** 607:7917 **607** no. 7917, (2022) 52–59. <https://www.nature.com/articles/s41586-022-04893-w>. viii, 1, 7
- [6] S. P. Martin, *A Supersymmetry Primer*, *Adv.Ser.Direct.High Energy Phys.* **18** (1997) 1–98, [arXiv:9709356 \[hep-ph\]](https://arxiv.org/abs/hep-ph/9709356).
http://www.worldscientific.com/doi/abs/10.1142/9789812839657_0001. viii, 1, 10, 11, 12, 13, 14, 59
- [7] N. Jarosik, C. L. Bennett, J. Dunkley, B. Gold, M. R. Greason, et al., *SEVEN-YEAR WILKINSON MICROWAVE ANISOTROPY PROBE (WMAP*) OBSERVATIONS: SKY MAPS*,

- SYSTEMATIC ERRORS, AND BASIC RESULTS*, *ApJS* **192** no. 2, (2011) 17,
[arXiv:1001.4744](https://arxiv.org/abs/1001.4744).
<https://iopscience.iop.org/article/10.1088/0067-0049/192/2/14>. 1, 9
- [8] M. Thomson, *Modern Particle Physics*. Cambridge University Press, 2013. viii, 1, 4, 5, 6, 9
- [9] A. D. Sakharov, *Violation of CP Invariance, C asymmetry, and baryon asymmetry of the universe*, *Pisma Zh. Eksp. Teor. Fiz.* **5** (1967) 32–35. 1, 9
- [10] F. Zwicky, *On the Masses of Nebulae and of Clusters of Nebulae*, *ApJ* **86** (1937) 217.
<https://ui.adsabs.harvard.edu/abs/1937ApJ...86..217Z/abstract>. 1, 8
- [11] V. C. Rubin and J. Ford, W. Kent, *Rotation of the Andromeda Nebula from a Spectroscopic Survey of Emission Regions*, *ApJ* **159** (1970) 379.
<https://ui.adsabs.harvard.edu/abs/1970ApJ...159..379R/abstract>. 1, 9
- [12] K. G. Begeman, A. H. Broeils, and R. H. Sanders, *Extended rotation curves of spiral galaxies: dark haloes and modified dynamics*, *Monthly Notices of the Royal Astronomical Society* **249** no. 3, (1991) 523–537.
<https://academic.oup.com/mnras/article/249/3/523/1005565>. viii, 1, 9
- [13] Planck Collaboration, *Planck 2013 results. XVI. Cosmological parameters*, *Astronomy and Astrophysics* **571** (2014), [arXiv:1303.5076](https://arxiv.org/abs/1303.5076).
<https://arxiv.org/abs/1303.5076v3>. 1, 9
- [14] D. Clowe, M. Bradač, A. H. Gonzalez, M. Markevitch, S. W. Randall, et al., *A Direct Empirical Proof of the Existence of Dark Matter*, *The Astrophysical Journal* **648** no. 2, (2006) L109–L113, [arXiv:0608407](https://arxiv.org/abs/0608407) [astro-ph].
<https://iopscience.iop.org/article/10.1086/508162>. 1, 9
- [15] M. Bradač, S. W. Allen, T. Treu, H. Ebeling, R. Massey, R. G. Morris, A. von der Linden, D. Applegate, and ;, *Revealing the properties of dark matter in the merging cluster MACSJ0025.4-1222*, *The Astrophysical Journal* **687** no. 2, (2008) 959–967,
[arXiv:0806.2320v2](https://arxiv.org/abs/0806.2320v2). <http://dx.doi.org/10.1086/591246>. 1, 9
- [16] T. S. Kuhn, *The Structure of Scientific Revolutions*. Chicago: University of Chicago Press, 1962. 2
- [17] G. F. Giudice, *The Dawn of the Post-Naturalness Era*, [arXiv:1710.07663v1](https://arxiv.org/abs/1710.07663v1). 2
- [18] M. E. Peskin and D. V. Schroeder, *An Introduction to Quantum Field Theory*. Westview Press, 1995. 4, 8
- [19] E. Noether, *Invariant variation problems*,
<http://dx.doi.org/10.1080/00411457108231446> **1** no. 3, (2006) 186–207, [arXiv:0503066](https://arxiv.org/abs/0503066) [physics].
<https://www.tandfonline.com/doi/abs/10.1080/00411457108231446>. 4

- [20] M. Gell-Mann, *The interpretation of the new particles as displaced charge multiplets*, II *Nuovo Cimento Series* **10** 4 no. 2, (1956) 848–866.
<https://link.springer.com/article/10.1007/BF02748000>. 4
- [21] T. Nakano and K. Nishijima, *Charge Independence for V-particles*, *Progress of Theoretical Physics* **10** no. 5, (1953) 581–582.
<https://academic.oup.com/ptp/article/10/5/581/1899895>. 4
- [22] K. Nishijima, *Charge Independence Theory of V Particles*, *Progress of Theoretical Physics* **13** no. 3, (1955) 285–304.
<https://academic.oup.com/ptp/article/13/3/285/1924498>. 4
- [23] The ALEPH Collaboration, The DELPHI Collaboration, The L3 Collaboration, The OPAL Collaboration, The SLD Collaboration, The LEP Electroweak Working Group, The SLD Electroweak and Heavy Flavour Groups, *Precision electroweak measurements on the Z resonance*, *Physics Reports* **427** no. 5-6, (2006) 257–454, arXiv:0509008 [hep-ex]. 5
- [24] W. Meissner and R. Ochsenfeld, *Ein neuer Effekt bei Eintritt der Supraleitfähigkeit*, *Naturwissenschaften* 1933 21:44 **21** no. 44, (1933) 787–788.
<https://link.springer.com/article/10.1007/BF01504252>. 5
- [25] J. Ranninger, *The conceptual heritage of superconductivity - from Meissner-Ochsenfeld to the Higgs Boson*, arXiv:1207.6911. <https://arxiv.org/abs/1207.6911v1>. 5
- [26] L. N. Cooper, *Bound Electron Pairs in a Degenerate Fermi Gas*, *Physical Review* **104** no. 4, (1956) 1189.
<https://journals.aps.org/pr/abstract/10.1103/PhysRev.104.1189>. 5
- [27] F. Englert and R. Brout, *Broken symmetry and the mass of gauge vector mesons*, *Physical Review Letters* **13** no. 9, (1964) 321–323.
<https://journals.aps.org/prl/abstract/10.1103/PhysRevLett.13.321>. 5
- [28] T. W. Kibble, *Symmetry Breaking in Non-Abelian Gauge Theories*, *Physical Review* **155** no. 5, (1967) 1554.
<https://journals.aps.org/pr/abstract/10.1103/PhysRev.155.1554>. 5
- [29] P. W. Higgs, *Spontaneous Symmetry Breakdown without Massless Bosons*, *Physical Review* **145** no. 4, (1966) 1156.
<https://journals.aps.org/pr/abstract/10.1103/PhysRev.145.1156>. 5
- [30] CMS Collaboration, *A portrait of the Higgs boson by the CMS experiment ten years after the discovery*, *Nature* 2022 607:7917 **607** no. 7917, (2022) 60–68, arXiv:2207.00043.
<https://www.nature.com/articles/s41586-022-04892-x>. 7
- [31] M. C. Gonzalez-Garcia and Y. Nir, *Neutrino masses and mixing: evidence and implications*, *Reviews of Modern Physics* **75** no. 2, (2003) 345, arXiv:0202058

- [hep-ph].
<https://journals.aps.org/rmp/abstract/10.1103/RevModPhys.75.345.7>
- [32] R. L. Workman et al., *Review of Particle Physics*, *PTEP* **2022** (2022) 083C01. 8, 10, 35, 61
- [33] L. Canetti, M. Drewes, and M. Shaposhnikov, *Matter and antimatter in the universe*, *New Journal of Physics* **14** no. 9, (2012) 095012, [arXiv:1204.4186](https://arxiv.org/abs/1204.4186).
<https://iopscience.iop.org/article/10.1088/1367-2630/14/9/095012>
<https://iopscience.iop.org/article/10.1088/1367-2630/14/9/095012/meta.9>
- [34] R. Catena and L. Covi, *SUSY dark matter(s) Review*, *Supersymmetry After Higgs Discov.* (2014) 121–136, [arXiv:1310.4776](https://arxiv.org/abs/1310.4776).
<http://dx.doi.org/10.1140/epjc/s10052-013-2703-4>. ix, 14
- [35] D. Alves, N. Arkani-Hamed, S. Arora, Y. Bai, M. Baumgart, et al., *Simplified models for LHC new physics searches*, *Journal of Physics G: Nuclear and Particle Physics* **39** no. 10, (2012) 105005, [arXiv:1105.2838](https://arxiv.org/abs/1105.2838).
<https://iopscience.iop.org/article/10.1088/0954-3899/39/10/105005>. 14
- [36] ATLAS Collaboration, *SUSY Summary Plots March 2022*, 2022.
<https://cds.cern.ch/record/2805985>. ix, 15, 16
- [37] The CMS Collaboration, *CMS Supersymmetry Physics Results, Run 2 Summary Plots*, 2021. <https://twiki.cern.ch/twiki/bin/view/CMSPublic/PhysicsResultsSUS>. ix, 15, 16
- [38] O. S. Brüning, J. Poole, P. Collier, P. Lebrun, R. Ostojic, et al., *LHC Design Report*, *CERN, Geneva* **1** (2004) 548. <https://cds.cern.ch/record/782076>. 17
- [39] L. Evans and P. Bryant, *LHC Machine*, *Journal of Instrumentation* **3** no. 08, (2008) S08001.
<https://iopscience.iop.org/article/10.1088/1748-0221/3/08/S08001>. 17, 18
- [40] J. Haffner, *The CERN accelerator complex. Complexe des accélérateurs du CERN*,
<http://cds.cern.ch/record/1621894>. ix, 18
- [41] The ALICE Collaboration, *The ALICE experiment at the CERN LHC*, *Journal of Instrumentation* **3** no. 08, (2008) S08002.
<https://iopscience.iop.org/article/10.1088/1748-0221/3/08/S08002>. 18
- [42] The LHCb Collaboration, *The LHCb Detector at the LHC*, *Journal of Instrumentation* **3** no. 08, (2008) S08005.
<https://iopscience.iop.org/article/10.1088/1748-0221/3/08/S08005>. 18
- [43] The CMS Collaboration, *The CMS experiment at the CERN LHC*, *Journal of Instrumentation* **3** no. 08, (2008) S08004.
<https://iopscience.iop.org/article/10.1088/1748-0221/3/08/S08004>. 18

- [44] ATLAS Collaboration, *The ATLAS Experiment at the CERN Large Hadron Collider*, *Journal of Instrumentation* **3** no. 08, (2008) S08003. <https://iopscience.iop.org/article/10.1088/1748-0221/3/08/S08003>. ix, 18, 21, 22, 23, 24, 25
- [45] The LHCf Collaboration, *The LHCf detector at the CERN Large Hadron Collider*, *Journal of Instrumentation* **3** no. 08, (2008) S08006. <https://iopscience.iop.org/article/10.1088/1748-0221/3/08/S08006>. 18
- [46] The TOTEM Collaboration, *The TOTEM Experiment at the CERN Large Hadron Collider*, *Journal of Instrumentation* **3** no. 08, (2008) S08007. <https://iopscience.iop.org/article/10.1088/1748-0221/3/08/S08007>[https://iopscience.iop.org/article/10.1088/1748-0221/3/08/S08007meta](https://iopscience.iop.org/article/10.1088/1748-0221/3/08/S08007/meta). 18
- [47] MoEDAL Collaboration, *Technical Design Report of the MoEDAL Experiment*, <https://cds.cern.ch/record/1181486>. 18
- [48] ATLAS Collaboration, *Luminosity Public Results Run 2*, tech. rep. <https://twiki.cern.ch/twiki/bin/view/AtlasPublic/LuminosityPublicResultsRun2>. ix, 19, 20
- [49] J. Pequeno, *Computer generated image of the whole ATLAS detector*, tech. rep., Mar, 2008. <https://cds.cern.ch/record/1095924>. ix, 21
- [50] ATLAS Collaboration, *Inner Detector Forward SCT Barrel SCT TRT Pixel Detectors Technical Design Report*, tech. rep. <https://cds.cern.ch/record/331063/files/ATLAS-TDR-4-Volume-I.pdf>. 22
- [51] ATLAS Collaboration, *Experiment Briefing: Keeping the ATLAS Inner Detector in perfect alignment*, tech. rep., Jul, 2020. <https://cds.cern.ch/record/2723878>. ix, 22
- [52] ATLAS Collaboration, *ATLAS Insertable B-Layer Technical Design Report Addendum*, Tech. Rep. May, Sep, 2012. <https://cds.cern.ch/record/1291633>. 23
- [53] K. Potamianos, *The upgraded Pixel detector and the commissioning of the Inner Detector tracking of the ATLAS experiment for Run-2 at the Large Hadron Collider*, [arXiv:1608.07850](https://arxiv.org/abs/1608.07850). <https://arxiv.org/abs/1608.07850v1>. 23
- [54] ATLAS Collaboration, *ATLAS pixel detector electronics and sensors*, *Journal of Instrumentation* **3** no. 07, (2008) P07007. <https://iopscience.iop.org/article/10.1088/1748-0221/3/07/P07007>. 23
- [55] T. Heim, *Status and performance of the ATLAS Pixel Detector after 3 years of operation*, *Nuclear Instruments and Methods in Physics Research Section A: Accelerators, Spectrometers, Detectors and Associated Equipment* **765** (2014) 227–231. 23
- [56] A. Ahmad, Z. Albrechtskirchinger, P. P. Allport, J. Alonso, L. Andricsek, et al., *The silicon microstrip sensors of the ATLAS semiconductor tracker*, *Nuclear Instruments and*

- Methods in Physics Research Section A: Accelerators, Spectrometers, Detectors and Associated Equipment **578** no. 1, (2007) 98–118.
<https://www.sciencedirect.com/science/article/pii/S0168900207007644>. 23
- [57] ATLAS Collaboration, *The ATLAS Transition Radiation Tracker (TRT) proportional drift tube: design and performance*, *Journal of Instrumentation* **3** no. 02, (2008) P02013.
<https://iopscience.iop.org/article/10.1088/1748-0221/3/02/P02013>. 23
- [58] ATLAS Collaboration, *ATLAS liquid-argon calorimeter : Technical Design Report*, CERN-LHCC-96-041 no. December, (1996) 606.
<https://cds.cern.ch/record/331061>. 23, 24
- [59] ATLAS Collaboration, *ATLAS tile calorimeter: Technical Design Report*, CERN/LHCC96-42(1996) (1996). <https://cds.cern.ch/record/331062>. 23, 25
- [60] ATLAS Collaboration, *ATLAS muon spectrometer : Technical Design Report*,
<https://cds.cern.ch/record/331068>. 25
- [61] ATLAS Collaboration, *Performance of the ATLAS muon triggers in Run 2*,
[arXiv:2004.13447v2](https://arxiv.org/abs/2004.13447v2). ix, 26, 30
- [62] ATLAS Collaboration, *Operation of the ATLAS trigger system in Run 2*, *Journal of Instrumentation* **15** no. 10, (2020), [arXiv:2007.12539v2](https://arxiv.org/abs/2007.12539v2). ix, 27
- [63] ATLAS Collaboration, *Performance of the missing transverse momentum triggers for the ATLAS detector during Run-2 data taking*, *Journal of High Energy Physics* **2020** no. 8, (2020), [arXiv:2005.09554v2](https://arxiv.org/abs/2005.09554v2). [http://dx.doi.org/10.1007/JHEP08\(2020\)080](http://dx.doi.org/10.1007/JHEP08(2020)080). 31
- [64] ATLAS Collaboration, *The ATLAS Tau Trigger in Run 2*, Jul, 2017.
<http://cds.cern.ch/record/2274201>. 31
- [65] ATLAS Collaboration, *Topological cell clustering in the ATLAS calorimeters and its performance in LHC Run 1*, *European Physical Journal C* **77** no. 7, (2016),
[arXiv:1603.02934](https://arxiv.org/abs/1603.02934). <https://arxiv.org/abs/1603.02934v3>. 31
- [66] ATLAS Collaboration, *Reconstruction, Energy Calibration, and Identification of Hadronically Decaying Tau Leptons in the ATLAS Experiment for Run-2 of the LHC*, tech. rep. <https://cds.cern.ch/record/2064383/>. 32
- [67] ATLAS Collaboration, *Electron reconstruction and identification in the ATLAS experiment using the 2015 and 2016 LHC proton-proton collision data at $\sqrt{s} = 13$ TeV*, *European Physical Journal C* **79** no. 8, (2019), [arXiv:1902.04655v2](https://arxiv.org/abs/1902.04655v2).
<http://dx.doi.org/10.1140/epjc/s10052-019-7140-6>. ix, 33, 42, 47
- [68] T. Atkinson, *Reconstruction of Electrons with the Gaussian-Sum Filter in the ATLAS Inner Detector*, tech. rep. 33

- [69] ATLAS Collaboration, *Electron and photon energy calibration with the ATLAS detector using 2015-2016 LHC proton-proton collision data*, *Journal of Instrumentation* **14** no. 3, (2018), arXiv:1812.03848v2.
<http://dx.doi.org/10.1088/1748-0221/14/03/P03017>. 33
- [70] ATLAS Collaboration, *Muon reconstruction and identification efficiency in ATLAS using the full Run 2 pp collision data set at $\sqrt{s} = 13$ TeV*, *The European Physical Journal C* **81** no. 7, (2021), arXiv:2012.00578.
<http://dx.doi.org/10.1140/epjc/s10052-021-09233-2>. 34, 92
- [71] ATLAS Collaboration, *Jet reconstruction and performance using particle flow with the ATLAS Detector*, *European Physical Journal C* **77** no. 7, (2017), arXiv:1703.10485v2.
<http://dx.doi.org/10.1140/epjc/s10052-017-5031-2>. 34
- [72] M. Cacciari, G. P. Salam, and G. Soyez, *The anti- k_t jet clustering algorithm*, *Journal of High Energy Physics* **2008** no. 4, (2008), arXiv:0802.1189v2.
<http://dx.doi.org/10.1088/1126-6708/2008/04/063>. 34
- [73] ATLAS Collaboration, *Tagging and suppression of pileup jets with the ATLAS detector*, tech. rep., May, 2014. <https://cds.cern.ch/record/1700870>. 34
- [74] I. Neutelings, *Hadronic tau decay*, https://tikz.net/tau_decay/. x, 35
- [75] ATLAS Collaboration, *Identification and energy calibration of hadronically decaying tau leptons with the ATLAS experiment in pp collisions at $\sqrt{s} = 8$ TeV*, *The European Physical Journal C* **2015 75:7 75** no. 7, (2015) 1–33, arXiv:1412.7086.
<https://link.springer.com/article/10.1140/epjc/s10052-015-3500-z>. 35
- [76] ATLAS Collaboration, *Identification of hadronic tau lepton decays using neural networks in the ATLAS experiment*, tech. rep., ATL-PHYS-PUB-2019-033, 2019. x, 35, 36, 92
- [77] ATLAS Collaboration, *Performance of missing transverse momentum reconstruction with the ATLAS detector using proton-proton collisions at $\sqrt{s} = 13$ TeV*, *European Physical Journal C* **78** no. 11, (2018), arXiv:1802.08168v2.
<http://dx.doi.org/10.1140/epjc/s10052-018-6288-9>. 36, 92
- [78] S. Höche, *Introduction to parton-shower event generators*, arXiv:1411.4085v2. 36
- [79] E. Bothmann, G. S. Chahal, S. Höche, J. Krause, F. Krauss, et al., *Event Generation with Sherpa 2.2*, *SciPost Physics* **7** no. 3, (2019), arXiv:1905.09127v2.
<http://dx.doi.org/10.21468/SciPostPhys.7.3.034>. 37
- [80] S. Alioli, P. Nason, C. Oleari, and E. Re, *A general framework for implementing NLO calculations in shower Monte Carlo programs: the POWHEG BOX*, *Journal of High Energy Physics* **2010** no. 6, (2010), arXiv:1002.2581v1.
[http://dx.doi.org/10.1007/JHEP06\(2010\)043](http://dx.doi.org/10.1007/JHEP06(2010)043). 37

- [81] J. Alwall, R. Frederix, S. Frixione, V. Hirschi, F. Maltoni, et al., *The automated computation of tree-level and next-to-leading order differential cross sections, and their matching to parton shower simulations*, *Journal of High Energy Physics* **2014** no. 7, (2014), [arXiv:1405.0301v2](https://arxiv.org/abs/1405.0301v2). [http://dx.doi.org/10.1007/JHEP07\(2014\)079](http://dx.doi.org/10.1007/JHEP07(2014)079). 37
- [82] T. Sjöstrand, S. Mrenna, and P. Skands, *A Brief Introduction to PYTHIA 8.1*, *Computer Physics Communications* **178** no. 11, (2007) 852–867, [arXiv:0710.3820v1](https://arxiv.org/abs/0710.3820v1). <http://dx.doi.org/10.1016/j.cpc.2008.01.036>. 37
- [83] J. Bellm, S. Gieseke, D. Grellscheid, P. Kirchgaesser, F. Loshaj, et al., *Herwig 7.1 Release Note*, [arXiv:1705.06919](https://arxiv.org/abs/1705.06919). <https://arxiv.org/abs/1705.06919v1>. 37
- [84] M. Bähr, S. Gieseke, M. A. Gigg, D. Grellscheid, K. Hamilton, et al., *Herwig++ physics and manual*, *European Physical Journal C* **58** no. 4, (2008) 639–707, [arXiv:0803.0883](https://arxiv.org/abs/0803.0883). <https://link.springer.com/article/10.1140/epjc/s10052-008-0798-9>. 37
- [85] D. J. Lange, *The EvtGen particle decay simulation package*, *Nuclear Instruments and Methods in Physics Research Section A: Accelerators, Spectrometers, Detectors and Associated Equipment* **462** no. 1-2, (2001) 152–155. 37
- [86] S. Agostinelli, J. Allison, K. Amako, J. Apostolakis, H. Araujo, et al., *GEANT4 - A simulation toolkit*, *Nuclear Instruments and Methods in Physics Research, Section A: Accelerators, Spectrometers, Detectors and Associated Equipment* **506** no. 3, (2003) 250–303. 38
- [87] ATLAS Collaboration, *The simulation principle and performance of the ATLAS fast calorimeter simulation FastCaloSim*, Oct, 2010. <https://cds.cern.ch/record/1300517>. x, 38, 51
- [88] ATLAS Collaboration, *Performance of electron and photon triggers in ATLAS during LHC Run 2*, *European Physical Journal C* **80** no. 1, (2020), [arXiv:1909.00761](https://arxiv.org/abs/1909.00761). <https://arxiv.org/abs/1909.00761v2>. x, 39, 40, 41, 43, 44, 47, 50
- [89] D. M. Koeck, “The ATLAS Electron and Photon Trigger Performance in Run 2.” <https://indico.cern.ch/event/754973/contributions/3536331/>. 39
- [90] D. M. Koeck, *The ATLAS electron and photon trigger performance in Run 2*, <https://doi.org/10.1142/S0217751X20440078> **35** no. 34-35, (2020). 39
- [91] ATLAS Collaboration, *Performance of the ATLAS Trigger System in 2015*, [arXiv:1611.09661](https://arxiv.org/abs/1611.09661). <http://dx.doi.org/10.1140/epjc/s10052-017-4852-3>. x, 40
- [92] ATLAS Collaboration, *Electron and photon energy calibration with the ATLAS detector using 2015-2016 LHC proton-proton collision data*, *Journal of Instrumentation* **14** no. 3, (2018), [arXiv:1812.03848v2](https://arxiv.org/abs/1812.03848v2). <http://dx.doi.org/10.1088/1748-0221/14/03/P03017>. 41, 92

- [93] ATLAS Collaboration, *Electron reconstruction and identification in the ATLAS experiment using the 2015 and 2016 LHC proton-proton collision data at $\sqrt{s} = 13\text{ TeV}$* , The European Physical Journal C **79** no. 8, . 45
- [94] ATLAS Collaboration, *AtlFast3: the next generation of fast simulation in ATLAS*, arXiv:2109.02551. <http://arxiv.org/abs/2109.02551>. 56
- [95] ATLAS Collaboration, “Search for the direct production of charginos and neutralinos in final states with tau leptons in $\sqrt{s} = 13\text{ tev}$ pp collisions with the atlas detector.” <https://cds.cern.ch/record/2815678>. xi, xiii, 57, 58, 100
- [96] D. M. Koeck, *Searches for supersymmetry in final states with at least two hadronically decaying tau leptons using the ATLAS detector*, 2022. <https://agenda.infn.it/event/28874/contributions/175844/>. 57
- [97] *LHC SUSY Cross Section Working Group*, 2022. <https://twiki.cern.ch/twiki/pub/LHCPhysics/SUSYCrossSections/>. xi, 58
- [98] W. Beenakker, C. Borschensky, M. Krämer, A. Kulesza, and E. Laenen, *NNLL-fast: predictions for coloured supersymmetric particle production at the LHC with threshold and Coulomb resummation*, Journal of High Energy Physics 2016 2016:12 **2016** no. 12, (2016) 1–25. [https://link.springer.com/article/10.1007/JHEP12\(2016\)133](https://link.springer.com/article/10.1007/JHEP12(2016)133). xi, 58
- [99] ATLAS Collaboration, *Search for the direct production of charginos and neutralinos in final states with tau leptons in $\sqrt{s} = 13\text{ TeV}$ pp collisions with the ATLAS detector*, European Physical Journal C **78** no. 2, (2018) 154. <https://link.springer.com/article/10.1140/epjc/s10052-018-5583-9>. xi, 59, 60, 86, 105
- [100] D. Albornoz Vásquez, G. Eve Bélanger, and C. Boehm, *Revisiting light neutralino scenarios in the MSSM*, tech. rep. arXiv:arXiv:1108.1338v1. <https://arxiv.org/pdf/1108.1338.pdf>. 59
- [101] ATLAS Collaboration, *Search for the direct production of charginos, neutralinos and staus in final states with at least two hadronically decaying taus and missing transverse momentum in pp collisions at $\sqrt{s} = 8\text{ TeV}$ with the ATLAS detector*, Journal of High Energy Physics **2014** no. 10, (2014) 1–52, arXiv:1407.0350. [https://link.springer.com/article/10.1007/JHEP10\(2014\)096](https://link.springer.com/article/10.1007/JHEP10(2014)096). 59
- [102] ATLAS Collaboration, *Search for the electroweak production of supersymmetric particles in $\sqrt{s} = 8\text{ TeV}$ pp collisions with the ATLAS detector*, Physical Review D **93** no. 5, (2016) 052002, arXiv:1509.07152. <https://journals.aps.org/prd/abstract/10.1103/PhysRevD.93.052002>. 59

- [103] CMS Collaboration, *Search for electroweak production of charginos and neutralinos in proton-proton collisions at $\sqrt{s} = 13\text{TeV}$* , *Journal of High Energy Physics* **2022** no. 4, (2021), [arXiv:2106.14246v2](https://arxiv.org/abs/2106.14246v2). [http://dx.doi.org/10.1007/JHEP04\(2022\)147](http://dx.doi.org/10.1007/JHEP04(2022)147). 62
- [104] M. Beneke, P. Falgari, S. Klein, and C. Schwinn, *Hadronic top-quark pair production with NNLL threshold resummation*, *Nuclear Physics B* **855** no. 3, (2012) 695–741. <https://www.sciencedirect.com/science/article/pii/S0550321311005803>. 62
- [105] M. Cacciari, M. Czakon, M. Mangano, A. Mitov, and P. Nason, *Top-pair production at hadron colliders with next-to-next-to-leading logarithmic soft-gluon resummation*, *Physics Letters B* **710** no. 4, (2012) 612–622. <https://www.sciencedirect.com/science/article/pii/S0370269312002766>. 62
- [106] P. Bärnreuther, M. Czakon, and A. Mitov, *Percent-Level-Precision Physics at the Tevatron: Next-to-Next-to-Leading Order QCD Corrections to $q\bar{q} \rightarrow t\bar{t}+X$* , *Phys. Rev. Lett.* **109** (2012) 132001. <https://link.aps.org/doi/10.1103/PhysRevLett.109.132001>. 62
- [107] M. Czakon and A. Mitov, *NNLO corrections to top-pair production at hadron colliders: the all-fermionic scattering channels*, *Journal of High Energy Physics* **2012** no. 12, (2012). 62
- [108] M. Czakon and A. Mitov, *NNLO corrections to top pair production at hadron colliders: the quark-gluon reaction*, *Journal of High Energy Physics* **2013** no. 1, (2013). 62
- [109] M. Czakon, P. Fiedler, and A. Mitov, *Total Top-Quark Pair-Production Cross Section at Hadron Colliders Through $\mathcal{O}(\alpha_s^4)$* , *Physical Review Letters* **110** no. 25, (2013). 62
- [110] M. Czakon and A. Mitov, *Top++: A program for the calculation of the top-pair cross-section at hadron colliders*, *Computer Physics Communications* **185** no. 11, (2014) 2930–2938. 62
- [111] P. Kant, O. Kind, T. Kintscher, T. Lohse, T. Martini, S. Mölbitz, P. Rieck, and P. Uwer, *HatHor for single top-quark production: Updated predictions and uncertainty estimates for single top-quark production in hadronic collisions*, *Computer Physics Communications* **191** (2015) 74–89. 62
- [112] M. Aliev, H. Lacker, U. Langenfeld, S. Moch, P. Uwer, and M. Wiedermann, *HATHOR – HAdronic Top and Heavy quarks crOss section calculatoR*, *Computer Physics Communications* **182** no. 4, (2011) 1034–1046. 62
- [113] A. Lazopoulos, T. McElmurry, K. Melnikov, and F. Petriello, *Next-to-leading order QCD corrections to $t\bar{t}Z$ production at the LHC*, *Physics Letters B* **666** no. 1, (2008) 62–65. 62
- [114] J. M. Campbell and R. K. Ellis, *$t\bar{t}W$ production and decay at NLO*, *Journal of High Energy Physics* **2012** no. 7, (2012). 62

- [115] S. Catani, L. Cieri, G. Ferrera, D. de Florian, and M. Grazzini, *Vector Boson Production at Hadron Colliders: A Fully Exclusive QCD Calculation at Next-to-Next-to-Leading Order*, *Physical Review Letters* **103** no. 8, (2009). 62
- [116] CERN, *CERN Yellow Reports: Monographs, Vol 2 (2017): Handbook of LHC Higgs cross sections: 4. Deciphering the nature of the Higgs sector*, 2017.
<https://e-publishing.cern.ch/index.php/CYRM/issue/view/32>. 62, 94
- [117] B. Fuks, M. Klasen, D. R. Lamprea, and M. Rothering, *Gaugino production in proton-proton collisions at a center-of-mass energy of 8 TeV*, *Journal of High Energy Physics* **2012** no. 10, (2012), [arXiv:1207.2159v2](https://arxiv.org/abs/1207.2159v2).
[http://dx.doi.org/10.1007/JHEP10\(2012\)081](http://dx.doi.org/10.1007/JHEP10(2012)081). 63
- [118] B. Fuks, M. Klasen, D. R. Lamprea, and M. Rothering, *Precision predictions for electroweak superpartner production at hadron colliders with Resummino*, *European Physical Journal C* **73** no. 7, (2013) 1–12, [arXiv:1304.0790v2](https://arxiv.org/abs/1304.0790v2).
<http://dx.doi.org/10.1140/epjc/s10052-013-2480-0>. 63
- [119] C. Borschensky, M. Krämer, A. Kulesza, M. Mangano, S. Padhi, et al., *Squark and gluino production cross sections in pp collisions at $\sqrt{s} = 13, 14, 33$ and 100 TeV*, *European Physical Journal C* **74** no. 12, (2014) 1–12, [arXiv:1407.5066v2](https://arxiv.org/abs/1407.5066v2).
<http://dx.doi.org/10.1140/epjc/s10052-014-3174-y>. 63
- [120] ATLAS Collaboration, *ATLAS data quality operations and performance for 2015-2018 data-taking*, *Journal of Instrumentation* **15** no. 4, (2019), [arXiv:1911.04632v2](https://arxiv.org/abs/1911.04632v2).
<http://arxiv.org/abs/1911.04632>. 64
- [121] ATLAS Collaboration, *Vertex Reconstruction Performance of the ATLAS Detector at $\sqrt{s} = 13$ TeV*, <https://cds.cern.ch/record/2037717>. 64
- [122] ATLAS Collaboration, *Selection of jets produced in 13 TeV proton-proton collisions with the ATLAS detector*, tech. rep., 2015. <https://cds.cern.ch/record/2037702/>. 65
- [123] ATLAS Collaboration, *Optimisation and performance studies of the ATLAS b-tagging algorithms for the 2017-18 LHC run*, tech. rep., CERN, Geneva, Jul, 2017.
<https://cds.cern.ch/record/2273281>. 65
- [124] C. G. Lester and D. J. Summers, *Measuring masses of semi-invisibly decaying particles pair produced at hadron colliders*, *Physics Letters, Section B: Nuclear, Elementary Particle and High-Energy Physics* **463** no. 1, (1999) 99–103, [arXiv:9906349v1](https://arxiv.org/abs/hep-ph/9906349v1) [hep-ph]. [http://dx.doi.org/10.1016/S0370-2693\(99\)00945-4](http://dx.doi.org/10.1016/S0370-2693(99)00945-4). 67
- [125] A. Barr, C. Lester, and P. Stephens, *m_{T2} : the truth behind the glamour*, *Journal of Physics G: Nuclear and Particle Physics* **29** no. 10, (2003) 2343–2363, [arXiv:0304226v1](https://arxiv.org/abs/0304226v1) [hep-ph]. <http://dx.doi.org/10.1088/0954-3899/29/10/304>. 67

- [126] R. D. Cousins, J. T. Linnemann, and J. Tucker, *Evaluation of three methods for calculating statistical significance when incorporating a systematic uncertainty into a test of the background-only hypothesis for a Poisson process*, *Nuclear Instruments and Methods in Physics Research Section A: Accelerators, Spectrometers, Detectors and Associated Equipment* **595** no. 2, (2008) 480–501, [arXiv:0702156](https://arxiv.org/abs/0702156) [physics]. 68
- [127] L. Moneta, K. Belasco, K. S. Cranmer, S. Kreiss, A. Lazzaro, et al., *The RooStats Project*, *Proceedings of Science* **93** (2010) 2010, [arXiv:1009.1003](https://arxiv.org/abs/1009.1003).
<https://arxiv.org/abs/1009.1003v2>. 68
- [128] R. Brun and F. Rademakers, *ROOT — An object oriented data analysis framework*, *Nuclear Instruments and Methods in Physics Research Section A: Accelerators, Spectrometers, Detectors and Associated Equipment* **389** no. 1-2, (1997) 81–86. 68
- [129] ATLAS Collaboration, *Jet energy scale measurements and their systematic uncertainties in proton-proton collisions at $\sqrt{s} = 13$ TeV with the ATLAS detector*, *Physical Review D* **96** no. 7, (2017), [arXiv:1703.09665v2](https://arxiv.org/abs/1703.09665).
<http://dx.doi.org/10.1103/PhysRevD.96.072002>. 92
- [130] ATLAS Collaboration, *Luminosity determination in pp collisions at $\sqrt{s} = 13$ TeV using the ATLAS detector at the LHC*, tech. rep., Geneva, Jun, 2019.
<https://cds.cern.ch/record/2677054>. 92
- [131] J. Butterworth, S. Carrazza, A. Cooper-Sarkar, A. D. Roeck, J. Feltesse, et al., *PDF4LHC recommendations for LHC Run II*, *Journal of Physics G: Nuclear and Particle Physics* **43** no. 2, (2016) 023001, [arXiv:1510.03865](https://arxiv.org/abs/1510.03865).
<https://iopscience.iop.org/article/10.1088/0954-3899/43/2/023001><https://iopscience.iop.org/article/10.1088/0954-3899/43/2/023001/meta>. 93
- [132] G. Cowan, *Statistical data analysis*. Oxford University Press, USA, 1998. 94, 97
- [133] M. Baak, G. J. Besjes, D. Cote, A. Koutsman, J. Lorenz, and D. Short, *HistFitter software framework for statistical data analysis*, *European Physical Journal C* **75** no. 4, (2014) 1–20, [arXiv:1410.1280](https://arxiv.org/abs/1410.1280). <http://dx.doi.org/10.1140/epjc/s10052-015-3327-7>. 95, 96, 98
- [134] G. Cowan, K. Cranmer, E. Gross, and O. Vitells, *Asymptotic formulae for likelihood-based tests of new physics*, *European Physical Journal C* **71** no. 2, (2010), [arXiv:1007.1727v3](https://arxiv.org/abs/1007.1727).
<http://dx.doi.org/10.1140/epjc/s10052-011-1554-0>. 96
- [135] A. L. Read, *Modified Frequentist analysis of search results (The CLs method)*,
<https://cds.cern.ch/record/451614/files/p81.pdf>. 96, 97
- [136] ROOT Collaboration, *HistFactory: A tool for creating statistical models for use with RooFit and RooStats*, tech. rep., New York, Jan, 2012.
<https://cds.cern.ch/record/1456844>. 98

-
- [137] ATLAS Collaboration, “Search for the direct production of charginos and neutralinos in final states with tau leptons in $\sqrt{s} = 13$ TeV pp collisions with the ATLAS detector.” <http://cds.cern.ch/record/2815678>. xiii, 107

This thesis was typeset using the \LaTeX typesetting system created by Leslie Lamport.
The body text size is set to 11 pt with *Utopia Regular* with *Fourier* font, part of \TeX Live.
The bibliography was typeset using the [ATLAS](#)-paper style.